

Lawrence Berkeley National Laboratory

Recent Work

Title

THE STUDY OF INTERGRANULAR EMBRITTLEMENT IN Fe-12Mn ALLOYS

Permalink

<https://escholarship.org/uc/item/7h9104v7>

Author

Lee, H.J.

Publication Date

1982-06-01



Lawrence Berkeley Laboratory

UNIVERSITY OF CALIFORNIA

Materials & Molecular Research Division

RECEIVED
LAWRENCE
BERKELEY LABORATORY

NOV 16 1982

LIBRARY AND
DOCUMENTS SECTION

THE STUDY OF INTERGRANULAR EMBRITTLEMENT
IN Fe-12Mn ALLOYS

Hyung Jai Lee
(Ph.D. thesis)

June 1982

TWO-WEEK LOAN COPY

*This is a Library Circulating Copy
which may be borrowed for two weeks.
For a personal retention copy, call
Tech. Info. Division, Ext. 6782.*



LBL-14747
c. 2

DISCLAIMER

This document was prepared as an account of work sponsored by the United States Government. While this document is believed to contain correct information, neither the United States Government nor any agency thereof, nor the Regents of the University of California, nor any of their employees, makes any warranty, express or implied, or assumes any legal responsibility for the accuracy, completeness, or usefulness of any information, apparatus, product, or process disclosed, or represents that its use would not infringe privately owned rights. Reference herein to any specific commercial product, process, or service by its trade name, trademark, manufacturer, or otherwise, does not necessarily constitute or imply its endorsement, recommendation, or favoring by the United States Government or any agency thereof, or the Regents of the University of California. The views and opinions of authors expressed herein do not necessarily state or reflect those of the United States Government or any agency thereof or the Regents of the University of California.

The Study of Intergranular Embrittlement in Fe-12Mn Alloys

Hyung Jai Lee

Materials Science and Molecular Research Division

Lawrence Berkeley Laboratory

and

Materials Science and Mineral Engineering Department

University of California, Berkeley

(Ph.D. Thesis)

June 1982

This work was supported by the Director, Office of Energy Research,
Office of Basic Energy Science, Material Science Division
of the U. S. Department of Energy under contract No. DE-AC03-76SF00098.

Table of Contents

Introduction	2
II. Experimental Procedure	5
A. Material Preparation and Heat Treatment	5
B. Mechanical Test	6
C. Measurements of Transformation Temperature and Phase	6
D. Microscopy	7
E. Auger Electron Spectroscopy	8
III. Experimental Results	11
A. Intergranular Embrittlement of Fe-12Mn Steel in the As-austenitized Condition	11
B. Effect of Alloying Elements	19
C. Effect of Tempering in Fe-12Mn Alloys	22
IV. Discussion	31
A. Intergranular Embrittlement in Fe-12Mn Steel in the As-Austenitized	

Condition	31
B. Effect of Boron Addition	34
C. Effect of Tempering in Fe-12Mn Alloys	38
V. Conclusions	43
References	45
Figure Captions	52
Figures	57

The Study of Intergranular Embrittlement in Fe-12Mn Alloys

Hyung Jai Lee

ABSTRACT

A high resolution scanning Auger microscopic study has been performed to investigate the chemical source of the intergranular fracture surfaces of Fe-12Mn steels in the as-austenitized condition. The fracture mode below the ductile-brittle transition temperature was found to be intergranular whenever the alloy was quenched from the austenite field, irrespective of the austenitizing time and temperature. High resolution chemical analyses of the intergranular fracture surface failed to reveal any consistent segregation of P, S, As, O, or N. The occasional appearance of S or O on the fracture surface was found to be due to a low density precipitation of MnS and MnO_2 along the prior austenite boundaries. An AES study with Ar^+ ion-sputtering showed no evidence of manganese enrichment along the prior austenite boundaries, but a slight segregation of carbon which does not appear to be implicated in the tendency toward intergranular fracture.

The addition of 0.002 weight percent boron with a 1000°C/1hr/WQ treatment yielded a high Charpy impact energy at liquid nitrogen temperature, preventing the intergranular fracture. The high resolution AES studies of the boron added alloy showed that the presence of approximately 3 atomic percent boron on the prior austenite grain boundaries is most effective in increasing the grain boundary cohesive strength in an Fe-12Mn alloy. Trace additions of Mg, Zr, or V, which are believed to be beneficial to the grain boundaries, had negligible effects on the intergranular

embrittlement.

A 450°C temper of the boron-modified alloys was found to cause tempered martensite embrittlement, leading to intergranular fracture. The embrittling treatment of the Fe-12Mn alloys with and without boron additions raised the ductile-brittle transition by 150°C. This tempered martensite embrittlement was found to be due to the Mn enrichment of the fracture surface to approximately 32 atomic percent Mn in the boron-modified alloy and 38 atomic percent Mn in the unmodified alloy. The Mn-enriched region along the prior austenite grain boundaries upon further tempering is believed to cause nucleation of austenite and to change the chemistry of the intergranular fracture surfaces.

ACKNOWLEDGEMENTS

The author would like to express his deepest appreciation to Professor J. W. Morris, Jr. for his continuous guidance and support throughout the course of this investigation. The author is also grateful to Professors A. Searcy and I. Finnie for their critical review of this manuscript. Special thanks are extended to Drs. Sunkeun Hwang, Chol Kyl Syn, and Jungihl Kim for their helpful advice.

The technical assistance provided by members of the Materials and Molecular Research Division, Lawrence Berkeley Laboratory, especially Brian Pope (ingot melting), Herb Liebe and Wayland Wong (machining), John Holthuis (alloy preparation), Sandy Stewart (purchasing), and Gloria Pelatowski (line drawings) is gratefully acknowledged.

The author wishes to thank Mrs. Jeanne Shull for her careful preparation and help with this manuscript. Thanks are also extended to the author's colleagues, especially to Mr. K. Sakai and Mr. L. Summers for their help in reviewing this manuscript.

The author is greatly indebted to his family, especially to his parents and brother, for their patience and support.

This work was supported by the Director, Office of Energy Research, Office of Basic Energy Science, Material Science Division of the U.S. Department of Energy under contract No. DE-AC03-76SF00098.

INTRODUCTION

A number of investigations have been made to study the mechanical properties of ferritic steels at very low temperatures. Excellent cryogenic strength and toughness have been achieved in ferritic steel by the addition of nickel (1-4) and proper heat treatment (5-7). With the hope that manganese could be successfully substituted for the comparatively expensive nickel addition, research on the low temperature mechanical properties of Fe-Mn alloys has been undertaken in several laboratories (8).

Studies (9-17) of Ni-free cryogenic ferritic steels have been conducted over the composition range 5-12% Mn because of the microstructural and chemical similarities between Mn and Ni as Fe alloying elements. Appropriate thermal and thermo-mechanical treatments have led to excellent cryogenic strength and toughness in these Fe-Mn alloys. The characteristic phase transformation (14,18) in Fe-Mn alloys with more than 10% Mn is of particular interest since these alloys form a metastable phase, hcp ϵ -martensite, as one of the transformation products, whereas Fe-Mn alloys with less than 10% Mn do not form different phases from those of the Fe-Ni alloys of less than 28% Ni. With the presence of the hexagonal ϵ -martensite, Fe-Mn alloys with composition over 8-12% Mn are of interest because they show the highest strength in the as-austenitized condition. As the Mn content is increased from 8 to 12%, the yield strength increases while the ductile-brittle transition temperature (DBTT) decreases slightly. Despite the low DBTT of the Fe-12 Mn alloy in the as-austenitized condition, below the DBTT this alloy fractures in a catastrophically intergranular mode while the Fe-8Mn alloy displays a transgranular cleavage fracture mode.

In earlier work (12-15) fundamental research into the embrittlement sources in Fe-12Mn alloy was conducted. The suppression of the low temperature intergranular embrittlement was successfully accomplished by a cold work plus temper, a controlled rolling treatment, or by adding a beneficial alloying element, specifically a trace addition of boron (19). These results suggested that the origin of intergranular embrittlement in

the Fe-12Mn steel in the as-austenitized condition is not due to the segregation of metalloid impurities or the formation of a deleterious second phase along the prior austenite grain boundaries, but is rather due to its inherent microstructures. However, this earlier conclusion (12-15,18) induced a significant argument about the sources of intergranular embrittlement because of the relatively low resolution of Auger electron spectroscopy.

Many high strength steels with small amounts of metalloid impurities have been known to be very susceptible to temper embrittlement (20-32) over the temperature range of 550-650°C, or tempered martensite embrittlement (33-38) around 300°C. Subsequently, tempered martensite embrittlement was found to have a transgranular cleavage fracture mode (39-40). In most cases, the intergranular brittleness due to tempering was attributed to austenite grain boundary carbide formation and metalloid impurities such as P, S, As, Sn or Sb segregation, which decrease the cohesive strength between the two phases. On the other hand, the transformation of unstable retained austenite to the carbides along the lath boundaries is believed to cause brittleness appearing as a transgranular cleavage mode.

The current research was designed to clarify the nature and source of intergranular embrittlement in Fe-12Mn in the as-austenitized condition by employing high resolution scanning Auger microscopy (SAM) and to investigate tempered martensite embrittlement in these alloys. Brittleness always develops along the same fracture path, i.e., intergranular fracture along the prior austenite grain boundaries. Special emphasis was placed on the investigation of changes in chemical composition on the intergranular fracture facets.

Further research on boron additions and austenitizing treatment were carried out to achieve better mechanical properties at low temperature. Improvements in the cohesive strength of the prior austenite grain boundaries of the Fe-12Mn alloy resulted in the suppression of the brittle intergranular failure below the ductile-brittle transition tem-

perature. Several alloying elements in addition to boron, which were believed to be beneficial to the grain boundaries, were added in the hope of changing the fracture mode from intergranular to transgranular. Tempered martensite embrittlement of the Fe-12Mn alloys with trace addition of beneficial alloying elements was also studied.

II. EXPERIMENTAL PROCEDURE

A. Material Preparation and Heat Treatment.

Alloys of nominal compositions Fe-12Mn were induction melted in an argon gas atmosphere. To study the effect of boron addition on the grain boundaries, minor additions of boron (ranging from 10 ppm to 100 ppm) and Ti (approximately 0.2%) were made. Special care was taken in the alloy preparation to reduce the effects of impurities. Each ingot was cast from a separate batch into a copper chill mold. The average weight of an ingot was 9 kg. The chemical composition of alloys is shown in Table I.

TABLE I

Chemical Composition of the Alloy Ingots in Wt. Pct.

Chemical Compositions								
Mn	Ti	C	O	A	P	N	B	Fe
12.0	0.000	0.003	0.004	0.006	0.008	0.005	0.00	Bal.
11.7	0.14	0.002	0.001	0.006	0.006	0.001	0.002*	Bal.

* Other chemical composition of alloys with boron ranging from 10 ppm to 1000 ppm is not available.

Mechanical test specimens were cut from plates and pre-machined to oversized dimensions before heat treatment. The as-austenitized specimens were sealed in stainless steel bags filled with argon and treated from 850°C to 1200°C and water quenched. Holding time at 1100°C ranged from 1 hour to 100 hours. The specimens for studying tempered martensite embrittlement were treated at temperatures ranging from 250°C to

650°C in 50°C increments for up to 200 hours. The specimens were usually water quenched after each heat treatment. All of these heat treated oversized specimens were finally machined under flood cooling to the proper dimensions of standard mechanical property test specimens.

B. Mechanical Testing

1. Hardness test.

Specimens tested for the hardness of the alloy were usually cut from broken Charpy impact test specimens. The hardness was measured on a Wilson Rockwell hardness tester. The Rockwell C scale was used for most of the specimens. At least five indentations were made and the readings averaged for each specimen. The standard deviation of the test was always within ± 0.5 for Rc scale.

2. Charpy impact test. The Charpy impact test specimens were machined to ASTM standard size shown in Figure 1. Notches of 45° were machined perpendicular to the rolling direction of the plate. The impact tests were carried out as described in ASTM E23. Various temperatures were obtained by a proper mixture of liquid nitrogen, isopentane, and Corning 710 oil. At least two Charpy V-notched specimens were tested at each testing temperature.

C. Measurements of Transformation Temperature and Phases.

1. Transformation temperature.

A Theta Dilatronic IIR dilatometer was employed for measuring transformation temperatures. Specimens prepared from bulk material were machined to the specifications given in Figure 2. Each specimen was heated to 1100°C with a programmed linear heating rate of 440°C/min and quenched by a jet stream of He gas with a quenching rate of approximately 70°C/sec. Transformation temperatures were determined by points deviating from linearity on dilation and temperature vs. time curves.

2. Phase.

X-ray diffraction analysis was carried out on specimens usually cut from broken Charpy specimens along the longitudinal direction. Specimen surfaces were carefully ground up to emery paper 600 grade and chemically polished in a solution of 100 ml H_2O_2 + 3 ml HF for 15 minutes in order to remove any strain-induced transformation phases from previous mechanical tests. A CuK_α radiation in a Picker x-ray diffractometer was used. The volume percent of each phase was calculated by comparing average integrated intensities of $(200)_\alpha$, $(200)_\gamma$ and $(101)_\epsilon$ peaks. The calculation is described in Schanfein's work (18).

D. Microscopy.

1. Scanning electron microscopy (SEM).

The fractographs of the broken Charpy specimens were obtained with an AMR 1000 scanning electron microscope operated at 20 kV. An energy dispersive analysis of x-rays (EDAX) combined with the SEM was employed to quantitatively analyze the chemical compositions of precipitates on the fracture surfaces.

2. Optical microscopy.

Specimens for optical microscopy were cut from the broken Charpy bars along a longitudinal direction. After mounting in Koldmount, they were ground on successive emery papers up to 600 grade. A final polishing was carried out on a 1μ diamond lapping wheel. The specimens were etched with either a 2% Nital or a picral (1 gm picric acid dissolved in 100 ml ethyl alcohol and 5 ml HCl) solutions. The microstructures were examined with a Carl Zeiss metallograph.

3. Transmission electron microscopy (TEM).

Specimens for transmission electron microscopy studies were sliced to about 12 mils thickness from the broken Charpy specimen. They were then chemically thinned

to about 5 mils in a solution of 100 ml H_2O_2 and 4 ml HF, spark cut into 3 mm discs and sanded down to about 2 mils thickness. Final thinning was carried out by a twin jet electro-polishing apparatus operated at room temperature using a solution of 75 gr CrO_3 , 400 ml CH_3COOH , and 21 ml H_2O . The optimum thinning condition was found at 30 mA and 50 V. The thinned specimens were examined in a JEM 7A or a Philips EM 301 operated at 100 kV.

4. Scanning transmission electron microscopy (STEM).

The grain boundary segregation was studied with a Philips 400 scanning transmission electron microscope operated at 100 kV. Thin foils for the STEM analysis were prepared using the same method as described for TEM. Chemical analysis of grain boundaries were carried out with an EDAX unit attached to the STEM.

E. Auger Electron Spectroscopy (AES).

Specimens for Auger electron spectroscopic studies were cut from the bulk plates and machined to oversized dimensions before heat treatment. The specimens were sealed and heat treated in stainless steel bags filled with argon gas. Following heat treatment, the specimens were machined to the shape and dimensions illustrated in Figure 3. In order to prevent any severe contamination of their surfaces, each specimen was dried following successive distilled water and ethyl alcohol rinses. They were then stored in a dessicator until being tested.

The Auger electron spectroscopic studies were carried out with a PHI model 590 scanning Auger microscope (SAM) combined with a scanning electron microscope and an Ar^+ ion-sputtering gun. At least two specimens were put into the reaction chamber equipped with an *in-situ* fracturing and cooling stage shown in Figure 4. The temperature of the specimen inside the reaction chamber was controlled by liquid nitrogen flowing through the fracture stage, monitored by a thermocouple. Each specimen was cooled to liquid nitrogen temperature within 30 minutes. The specimens to be frac-

tured were subjected to a $5 \times 10^{-10} - 1 \times 10^{-9}$ Torr vacuum attained by employing a differential ion pump, a Ti sublimation pump, and a liquid nitrogen cold trap. The specimens were always impact-fractured by hammer to reveal its fresh fracture surface.

After fracture, the specimen was positioned in front of the SAM cylindrical mirror analyzer (CMA). The time required for the first Auger electron spectrum usually took no more than 5 minutes. The primary electron energy and peak-to-peak modulation used were 2 kV or 5 kV and 3 eV or 6 eV, respectively, depending on the energy scanning range. The primary electron beam size ranging $2 \mu \sim 0.3 \mu$ in diameter was regulated according to the places needed to be analyzed. In order to obtain a typical spectrum from a grain boundary, at least 10 points on an intergranular cleavage surface were analyzed with 0.3% energy resolution, monitored by the attached scanning electron microscope. The time constant per point and the sweep rate were 0.03 second/point and 0.5 eV/sec, respectively. For automatic data acquisition, a multiple-technique analytical computer system (MACS) provided with the PHI model 590 SAM was employed with the parameters: time/point (T/P) = 50 msec, peak-to-peak modulation (Mod) = 6 eV, and volt/step (V/S) = 1 eV. Most of AES chemical analyses were carried out by this programmed MACS.

Following the AES analysis on the fresh fracture surface, the surface was sputtered by an Ar^+ ion gun at normal incidence. In most cases, a primary ion beam voltage of 3 kV was used. In order to derive the sputtering rate for a Fe-12Mn alloys, the same sputtering conditions were maintained as those for Ta_2O_5 epitaxy thin film reference. It is expected from other works (52) that the sputtering rates for Fe-12 Mn alloys were approximately 100 Å/min at 3 kV and 50 Å/min at 1 kV, respectively, which does not differ from those for the Ta_2O_5 reference by less than a factor of 2. The sputtered regions were always re-analyzed to compare the difference between the surface before and after sputtering.

Whenever it was necessary to determine the degree of contamination on the fresh and sputtered surfaces, the chemical analysis of the residual gas inside the reaction chamber was performed with a residual gas detector 3M Model 710 secondary ion mass spectrometer (SIMS). The relative chemical composition of the residual gas and the pressure inside the AES analysis chamber were recorded during AES analysis.

III. EXPERIMENTAL RESULTS

A. Intergranular Embrittlement of Fe-12Mn Steel in the As-Austenitized Condition.

1. Austenitizing treatment.

Previous research (14,15) has shown that the Fe-12Mn steel in the as-austenitized condition fails in a strikingly brittle intergranular fracture mode below the DBTT. The austenitizing treatment was performed at 1100°C for 2 hours which was followed by water quenching. The ductile-brittle transition occurred sharply at room temperature in the Charpy impact test as shown in Figure 5. The decrease in the Charpy impact energy value on lowering temperature is correlated with the change in the fracture mode from a ductile dimple rupture mode (transgranular) to catastrophic intergranular fracture mode, as shown in Figure 6. Brittle intergranular fracture always occurred along the prior austenite grain boundaries, whose dimension was approximately 170 μm .

To investigate the effect of austenitizing temperature on the fracture mode, the austenitizing treatments were conducted either (1) at temperatures ranging from 850°C to 1200°C for 2 hrs, or (2) from 2 hrs to 100 hrs at 1100°C, all of which were followed by water quenching. Two hour heat treatments were sufficient to obtain both the fully recrystallized austenite phase and to form a consistent microstructure. Table II shows that the prior austenite grain size of the Fe-12Mn steel changed from 15 μm to 250 μm . The hardness and Charpy impact energy value at liquid nitrogen temperature (LNT) were nearly independent of austenitizing temperature as shown in Figure 7. The fracture mode below the DBTT was 100% intergranular cleavage irrespective of the prior austenite grain size. Figure 8 displays four different fractographs of very flat, smooth intergranular fracture facets along prior austenite grain boundaries after austenitizing treatments at 850°C, 1000°C, 1100°C, and 1200°C, respectively. The change in holding time at 1100°C from 2 hrs up to 100 hrs affects neither the fracture mode nor the prior austenite grain size. The grain boundary microstructures are similar for all heat treatments, but the grain boundary chemistry will be discussed in a later section.

TABLE II

Changes in the Prior Austenite Grain Size and Fracture

Mode with Respect to Austenitizing Temperature

Heat Treatment	Grain Size (μm)	Fracture Mode
850°C/2hrs/WQ	~15	Intergranular
900°C/2hrs/WQ	~30	Intergranular
1000°C/2hrs/WQ	~85	Intergranular
1100°C/2hrs/WQ	~170	Intergranular
1200°C/2hrs/WQ	~250	Intergranular

2. High resolution AES analysis of intergranular cleavage surface.

Chemical analyses of the intergranular cleavage surfaces of different grain sized specimens were obtained using a high resolution scanning Auger microscope with a $1\mu\text{m}$ electron beam size, a 3 eV peak-to-peak modulation, a 2 kV primary electron voltage, and 0.3% energy resolution. A typical Auger electron spectrum obtained from the in-situ fracture surfaces of an Fe-12Mn steel in the as-austenitized condition is shown in Figure 9, together with the corresponding SEM fractograph. The surface-sensitive AES technique (41-45) was applied to detect any segregation within a monolayer of the surface on the prior austenite grain boundaries, the fracture path of this alloy. High resolution AES analysis shows that in addition to the Fe and Mn Auger electron peaks, there is a small carbon peak at 272 eV. Taking the sensitivity from 10X to 40X, it is clear that there are no other significant peaks such as P at 120 eV and S at 150 eV. Those Auger electron peaks are also consistently present in the specimens austenitized at different temperatures. Auger electron spectra obtained from the specimens which

were austenitized at 1100°C for either 40 hrs or 100 hrs show very similar chemistries except for the appearance of a small nitrogen Auger electron peak at 379 eV, as shown in Figure 10. On occasion, a high intensity S or O peak was observed in the Auger electron spectra from an intergranular cleavage surface. First, a determination of the source of the S or O peak was carried out by a SEM fractographic study. As shown in Figure 11, high magnification SEM analysis revealed the presence of small precipitates along the cleavage surfaces. Precipitate size ranged from 0.5 to 5 μm in diameter. On the average, five such precipitates were found to be associated with each cleavage surface. These precipitates were not easily distinguishable during lower magnification SEM examination. Chemical analysis of these precipitates using EDAX, shown in Figure 11, revealed that these precipitates are of two types. The first is MnS, the other is an oxide or carbide precipitate of Mn which cannot be positively identified due to the limitations of the EDAX system. Second, a high partial resolution AES analysis was conducted over the fracture surface. In most cases a medium electron beam size (1-2 μm) was used for the AES study. With a smaller electron beam size (0.3 μm), chemical analyses of the precipitates and holes on the intergranular cleavage facets were carefully performed. Upon examining the fractograph in Figure 12, one interpretation could be that there possibly exist four different chemistries. The chemistry detected is dependent on the location of the point of analysis. From the Auger electron spectrum of Figure 12-a, this precipitate was identified as MnS which is in agreement with the EDAX results. Figure 12-b reveals that this precipitate is a Mn oxide (possibly MnO_2) whose surface was decorated by the segregation of S. The hole in the SEM fractograph of Figure 12-c was analyzed by Auger electron spectroscopy. Analysis of the spectrum shows that small amounts of S, C, and N segregated along the interface between the precipitate and the prior austenite grain boundary. These segregations may reduce the interface energy so that the precipitate was easily separated from the matrix. An Auger electron spectrum identical to that produced by holes in the fracture surface was

obtained from the flat fracture surface shown in Figure 12-d.

3. C, N, or Mn on the prior austenite grain boundaries.

As shown in the previous section, a small carbon or nitrogen peak in the Auger electron spectra (Figures 9 and 10) was always detected on fresh intergranular cleavage facets. It is believed that the grain boundary properties are influenced by the presence of carbon or nitrogen, which are assumed to have segregated to the prior austenite grain boundaries during austenitizing. To this extent a careful investigation into the source and effect of these elements was carefully performed.

After AES analysis of the in-situ fractured surface, an Ar^+ ion-sputtering technique, which is described elsewhere (46-51) was employed. The use of this ion-sputtering technique, combined with AES analysis, is very effective in studying the surface chemistry in two ways. First, it is possible that two different surface chemistries may be obtained before and after sputtering. Thus, AES analyses on the sputtered surface, as well as the unsputtered surface, may give evidence of some differences in the chemistry between the grain boundary and the matrix. Second, by comparing the peak-to-peak amplitude of definite elements by sputtering layer by layer, a depth profile of certain elements from the grain boundary to the inside matrix can be easily obtained within sub-layer sensitivity. This is possible because the AES analysis has a high depth resolution, on the order of one monolayer. Examination of this depth profile can tell how the concentration changes with respect to depth.

Figure 13 shows two different Auger electron spectra of the specimen austenitized at 1100°C for 2 hrs. Figure 13a was obtained from an intergranular fracture surface produced at LNT and thus indicates the prior austenite grain boundary chemistry. However, sputtering with Ar^+ ions for two minutes brought about a slightly different Auger electron spectrum of Figure 13b. The significant difference between the two spectra can be recognized as the existence of a carbon peak at 272 eV. An unsputtered surface has a small amount of carbon and a sputtered one does not. The small Auger

electron peak at 215 eV can be identified as an argon peak from Ar^+ ions implantation. The occurrence of carbon segregation in the specimen austenitized at 1100°C was partly proved by Figure 13. Employing higher sensitivity, it is easily recognized that carbon can be sputtered away from the grain boundaries, as shown in Figure 14.

An attempt to identify the status of carbon from the AES spectra was made by comparing carbon Auger electron peak shapes and peak energy shifts (42,52). As shown in Figure 15, the partial AES spectrum, produced by using higher sensitivity, furnishes more precise carbon peak shape and energy information. The comparison of carbon Auger peak shapes and energies between atomic carbon and a carbide is so distinct that the carbon peak in Figure 15 is believed to be one of carbides. However, despite this possibility, the existence of a continuous carbide film along the prior austenite grain boundaries in the specimens austenitized at 1100°C or even 1200°C is rejected. This theory could be confirmed by carbon depth profile analysis.

An AES analysis combined with an Ar^+ ion-sputtering technique (52) provides a concentration depth profile near the surface with less than a monolayer depth resolution. Determination between segregation and thin film (continuous second phase) phenomena was successfully accomplished by this depth profile analysis. The sputtering profile shown in Figure 16a depicts how carbon concentration changed with depth. The carbon depth profile indicates that carbon atoms are equilibrium-segregated to the prior austenite grain boundaries rather than as a thin carbide film. It was observed that the depth of carbon segregation is about 30 *angstrom* along the grain boundaries.

Small amounts of nitrogen were detected on the intergranular fracture surface in the specimens austenitized at 1100°C for 100 hrs. A small nitrogen Auger electron peak slowly appeared in the spectra when the specimens were austenitized at 1100°C for more than 40 hrs. The peak height of nitrogen is similar to that of carbon and it disappeared simultaneously with the carbon peak after 3 minutes of Ar^+ ion-sputtering. It is concluded from Figures 16b and 17 that nitrogen had also segregated to the prior

austenite grain boundaries.

Possible manganese segregation was investigated by the Ar^+ ion sputtering technique. Manganese has four different major Auger electron transition peaks which are the KLL Auger transition peak at 40 eV, and the LMM peaks at 542 eV, 589 eV, and 636 eV, respectively. Since the strongest Mn Auger electron peak at 589 eV is very close to the strong Fe Auger peak at 598 eV, the strongest Mn peak at 542 eV was used to obtain the Mn depth profile. As shown in Figure 16a, the Mn concentration along the grain boundaries was not changed at all and thus, no Mn enrichment region exists along the prior austenite grain boundaries to affect the grain boundary properties. However, the grain boundary composition is presumably another important factor concerned with the intergranular embrittlement which will be discussed later.

Intergranular surface chemical composition was calculated from the Auger peak-to-peak amplitudes on the AES spectra of the specimen fractured in an ultra high vacuum (6×10^{-10} Torr). The atomic percent C_x of element x is approximated by

$$C_x = \frac{\frac{I_x}{S_x d_x}}{\sum_n \frac{I_n}{S_n d_n}}$$

where I_x is the peak-to-peak Auger amplitude, S_x is the relative sensitivity between element x and the standard, and d_x is the scale factor which is $L_x E_{m,x} I_{p,x}$. The scale factor d_x in this equation is constant if the lock-in amplifier sensitivity, L_x , modulation, $E_{m,x}$, and the primary beam current, $I_{p,x}$, settings used to obtain the test spectrum are the same for all peaks and cancel out. The relative sensitivity, S_x , is obtained from the "Handbook of Auger Electron Spectroscopy" (53), and is described in detail. Table III shows the chemical compositions of grain boundaries and matrix obtained by sputtering in two different austenitized specimens. The reported composition is the average of at least 5 analyses. The chemical composition difference between the grain boundaries and the matrix is approximately 0.4 atomic percent carbon and 0.5 atomic percent nitrogen.

TABLE III

Chemical Composition of Grain Boundaries and the Matrix Obtained by AES Analyses

Specimen		Chemical Composition			
		Mn	C	N	Fe
1100°C/2hrs/WQ	Grain Boundary	12.5	0.4	-	Bal.
	Matrix*	12.6	-	-	Bal.
1100°C/100hrs/WQ	Grain Boundary	12.4	0.4	0.5	Bal.
	Matrix*	12.4	-	-	Bal.

* The chemical composition of the matrix was obtained from the Ar^+ ions sputtered surface.

Despite an austenitizing treatment, the amount of carbon or nitrogen on the grain boundaries is consistent when the in-situ fractured surfaces was analyzed in UHV within a certain length of analyzing time. A significant build-up of carbon and oxygen peaks which occurred 30 minutes after fracturing, presumably is due to the decomposition of carbon monoxide (CO) (54) on the fresh surface. Surface adsorption of C and O, assumed to happen in UHV, was analyzed by the residual gas detector as shown in Figure 18. The adsorption of C or O in UHV is beyond the present research; however, most of the Auger data before 30 minutes are available for calculating the surface composition.

4. Microstructure.

Previous works (9-14,55-57) showed that an Fe-12 Mn alloy has three different crystal structures which are fcc austenite, bcc α martensite, and hcp ϵ martensite. The

transformation temperatures measured by dilatometry are shown in Table IV. The various transformation temperatures of Fe-12Mn steel are slightly different from those of Fe-12Mn-0.2Ti because of the Ti addition. The appearance of the three different phases in Fe-12Mn alloy represent very unique submicrostructures. Figure 19 shows typical optical micrographs of specimens austenitized for 2 hrs at 900° and 1100°C, respectively. These micrographs show straight well-aligned martensite structures with different sized martensite packets. An attempt to reveal grain boundary etching (58,59) due to impurity segregation as performed on other steels was not successful.

TABLE IV.

Transformation Temperature (°C) of Fe-12Mn Alloy

Nominal Composition	Temperature (°C)					
	A_{se}	A_{fe}	$A_{sa'}$	$A_{fa'}$	$M_{sa'}$	$M_{fa'}$
Fe-12Mn-0.2Ti*	240	350	570	670	260	120
Fe-12Mn	230	340	560	670	270	130
Fe-12Mn-0.2Ti-0.002B	340	390	600	680	230	150

* From Hwang's data.

In Figure 20, a transmission electron micrograph shows the microstructure of a region along the prior austenite grain boundary. The phases present in the microstructure are α - and ϵ -martensite. An Fe-12Mn steel in the as-austenitized condition has blocky martensite structures which were often bound by thin ϵ -martensite. No apparent second phases were found along the grain boundary. The distribution of the

ϵ -martensite was also studied. A dark field transmission electron micrograph shown in Figure 21 displays no indication of a continuous film of ϵ - martensite along the boundary.

B. Effect of Alloying Elements

5. Addition of alloying elements.

The present high resolution SAM studies, together with the previous results, strongly suggested that the intergranular fracture in Fe-12Mn was not caused by the formation of a deleterious phase on, or impurity segregation to the prior austenite grain boundaries. Hwang and Morris (19) also suggested that if the preference for intergranular fracture in Fe-12Mn is an inherent bias due to the relative difficulty of transgranular cleavage, then an appropriate approach to toughen the alloy, e.g., to change its fracture mode from intergranular to transgranular, would be to add a chemical species which segregates to the prior austenite boundaries and increase their relative cohesion. An addition of boron was successful in suppressing the intergranular embrittlement and improving the cryogenic mechanical properties. However, the effect of boron segregation on the impact toughness during austenitization was not fully investigated and the effect of the additions of other alloying elements on the intergranular brittleness is unconfirmed.

Figure 22 shows the Charpy impact energy vs. boron contents (ppm) in an Fe-12Mn alloy, austenitized at 1000°C for 1 hour. Regardless of austenitizing treatment, the maximum impact value was obtained in the specimen with 20 ppm boron. This 20 ppm boron is the optimized content in evaluating the Charpy value even though an addition of boron ranging from 10 ppm to 1000 ppm changes its fracture mode. This result agrees with Hwang and Morris' work (19). Their autoradiography studies to reveal the segregation of boron to grain boundaries in the specimens austenitized at 1000°C were very successful, but not successful enough to quantitatively establish the

amount of boron segregation.

As shown in Figure 23, austenitization at 1000°C for 1 hour followed by water quenching gives maximum Charpy impact energy value at LNT. If two major factors are considered to affect Charpy values, they are prior austenite grain size and the degree of boron segregation to the grain boundaries. Prior austenite grain size dramatically increases at temperatures higher than 1000°C, as shown in Figure 24. Careful examination of fractographs in Figure 25, shows that the specimen austenitized at 850°C for 1 hour displays 100% intergranular fracture and the fraction of intergranular fracture slowly decreases as heat treatment temperature goes up, yielding totally transgranular fracture in the specimen heat treated at 1000°C. The build-up of boron segregation to the grain boundaries was monitored by SAM study. An AES spectrum of Figure 26 shows the existence of boron on the grain boundaries. The amount of boron segregation was calculated to be approximately 0.7 atomic percent by using the previously described method. The specimens austenitized at higher temperatures have more boron segregation to the grain boundaries as shown in Figure 27. Unfortunately, the amount of boron segregated to the austenite boundaries at 1000°C was not accurately obtained from this experiment. Since most of the segregation of metalloid impurities are reported to occur during an austenitizing treatment (60,61), intergranular fracture was intentionally induced by short time tempering (10 minutes) at 650°C followed by austenitizing at 1000°C for 1 hour and the amount of boron on the grain boundaries was calculated to be approximately 2.9 atomic percent. This result will be discussed later. It should, however, be noted that austenitizing at 1000°C for 1 hour is the optimum condition for grain size effect and boron segregation. An attempt to find out other alloying elements which are also beneficial to increasing grain boundary cohesion was performed. Small amounts of Mg, Nb, or Zr are reported to segregate easily to the grain boundaries of Ni-base alloys or high strength alloys (62,63). As for these alloying elements effect on the austenitization treatment, an addition of 0.1-0.5% Mg,

1% V, or 0.1% Zr did not segregate to the austenite boundaries and thus, are not assumed to affect the intergranular embrittlement. AES spectra obtained from the intergranular fracture surface of the specimen are almost the same as that from the specimen without addition of Mg, V, or Zr.

6. Effect of segregation of boron on the grain boundaries.

As the austenitizing temperature for the Fe-12Mn with 20 ppm of boron was raised from 850° to 1000°C, the fraction of intergranular fracture mode was dramatically reduced as shown in Figure 25. Coincidentally, the change in the fracture mode was well-matched with the increase in the amount of boron segregated to the grain boundaries. The transformation temperature of the specimen with the addition of boron, measured by dilatometry, is shown in Table IV. Transformations for $\epsilon \rightarrow \gamma$ and $\alpha' \rightarrow \gamma$ in the specimen with boron occurred at slightly higher temperatures than in the specimens without boron and the $\gamma \rightarrow \alpha'$ transformation on cooling was obtained at a lower temperature. However, phases in the as-austenitized condition are fairly well preserved. Figure 28 provides TEM microstructures of the specimen with boron, which shows typical blocky type martensite. This microstructure was not affected by austenitizing temperature and time. As reported by Hwang and Morris (19), an addition of boron in Fe-12Mn acts as a 'grain boundary glue' and consequently prevents catastrophic intergranular failure along the prior austenite boundaries. The 'gluing effect' of boron largely depends on the grain boundary boron concentration. The fractograph of Figure 29a shows that the specimen austenitized at 850°C has a completely intergranular cleavage surface which was analyzed to have less than 1 atomic percent boron. It is, however, noted that the fracture surface is not flat and smooth, but was plastically deformed. This phenomenon is more clearly seen in the specimen austenitized at a higher temperature. Figure 29b displays less intergranular fracture and more ductility around the boundaries because more boron segregation to the grain boundaries. Optimum boron content on the grain

boundaries (which was calculated to be about 3 atomic percent boron) develops fully transgranular fracture in the specimen austenitized at more than 1000°C, as shown in Figure 30a. It is also noteworthy that transgranular fracture in this specimen is rather unique, not like dimple ruptured fracture. High magnification SEM fractograph of Figure 30b clearly shows that failure occurred transgranularly with negligible plastic deformation.

C. Effect of Tempering in Fe-12Mn Alloys.

In the previous sections, the investigation of intergranular embrittlement of an Fe-12Mn steel in the as-austenitized condition was investigated by high resolution SAM and the effect of a boron addition of the intergranular embrittlement were described. However, the boron-added Fe-12Mn alloy which was tempered at 450°C after austenitizing treatment undergoes intergranular failure similar to that observed in an Fe-12Mn alloy without boron additions in the as-austenitized condition. In this section, the results of tempered martensite embrittlement in the Fe-12Mn alloy with and without the addition of boron are described.

1. Tempered martensite embrittlement.

The variation of Charpy impact toughness (CVN) at LNT with tempering temperature for the boron modified Fe-12Mn alloy is shown in Figure 31. Tempering at a higher temperature of 450°C results in a large decrease in Charpy impact energy. The display of a 'toughness trough' around this temperature is the so-called tempered martensite embrittlement (TME). The variation of fracture mode with tempering temperature is shown in Figure 32. Specimens tempered at 250°C failed by a typical transgranular fracture mode (Figures 32a and b) which is identical to the fracture mode in the as-austenitized specimen. As the tempering temperature was raised to 450°C, the fracture mode changed from almost transgranular to 100% intergranular cleavage (Figures 31c-f). Further tempering temperature increases result in a reversion to

transgranular fracture (Figures 32g-j). Examination of fractographs within this tempering temperature range leads to two significant results; one is that the specimen tempered in the embrittlement range always failed by intergranular cleavage along the prior austenite grain boundaries and the other is that the change in the fraction of the intergranular fracture mode is always coincidental with the change in Charpy impact energy values.

The ductile-brittle transition curves shown in Figure 33 represent the DBTT of the specimens in the as-austenitized and tempered (450°C) conditions, respectively. The embrittling treatment results in an increase of the transition temperature by 150°C. This increase in the transition temperature in the specimen tempered at 450°C after 1000°C austenitizing is accompanied by an appearance of a 100% intergranular fracture mode below the DBTT instead of a 100% transgranular fracture mode in the specimen in the as-austenitized condition. Since an Fe-12Mn steel without the boron addition always failed by intergranular cleavage below the transition temperature, the TME phenomenon of this alloy demonstrates an extension of the upper limit for observing intergranular fracture mode to a higher temperature by 150°C when the alloy was tempered at 400°C after austenitizing at 1000°C. This phenomenon is also illustrated in the ductile-brittle transition curves shown in Figure 34.

Since Hwang (14) pointed out some significant change of the grain boundary chemistry in the embrittled treated specimen, this present investigation toward tempered martensite embrittlement also concentrated on the AES study of the intergranular cleavage surface when the specimen became brittle. Due to its high sensitivity to surface chemistry and a need for one or two layers dimension detectability in studying the grain boundary structure, an AES technique could be applied only when the grain boundaries are exposed, as in the case of intergranular fracture surfaces. Before investigating the chemical source of the intergranular embrittlement in the boron modified specimen tempered at 450°C, extensive AES studies of the specimen without boron

addition were performed due to their similarities. The reasons for starting with an Fe-12Mn alloy without boron are that this alloy always displays intergranular failure and tendency toward intergranular embrittlement by tempering, and is similar to the boron-added alloy. Some investigators (64) reported an application of AES technique in studying grain boundary chemistry by intentionally inducing intergranular fracture by means of hydrogen charging into the specimen, even though the specimen failed by transgranular cleavage or ductile rupture before charging treatment. The present research avoided this method for its complexity of explaining the embrittlement phenomenon.

Two typical AES spectra obtained from the as-quenched (or quenched and tempered at 250°C/1 hr/WQ) and the embrittled Fe-12Mn steel are shown in Figure 35. The most significant differences found between these two spectra were in the Mn Auger peaks. The relative intensity of the Mn peaks in the embrittled specimen is higher than that found in the other heat treated specimens by a factor of 3. Except for the Mn Auger peaks, no other significant Auger peaks such as P, S, As or Sb appear. Figure 36 represents the chemistry of the intergranular fracture surface of the boron-modified Fe-12Mn alloy which was austenitized and tempered at 450°C for 1 hour. It is impossible to measure the change of the grain boundary chemistry during tempering with these specimens. However, this typical AES spectrum obtained from the embrittled boron-modified Fe-12Mn alloy can be summarized by the existence of the boron Auger peak at 179 eV, two Ti peaks, relatively strong Mn peaks and three major Fe peaks. It is plausible that the embrittled specimens without and with boron addition display higher Mn concentration on the intergranular fracture surfaces.

2. Intergranular fracture surface chemistry.

Tempering in the two-phase region has been extensively documented in many alloys (65-68), resulting in desirable cryogenic mechanical properties due to its effective grain refining through the two-phase decomposition. Tempering of Fe-12Mn alloys was

initiated for this purpose. The definition for "grain boundary during tempering" in Fe-12Mn steels will be a prior austenite grain boundary in the martensite matrix because this boundary is a crystallographically high angle boundary and preserved during the two-phase decomposition. It should also be noted that a prior austenite grain boundary is believed to be the right unit for most chemical segregation, effective interruption of dislocation motion, and preferred sites for austenite nucleation.

The variation in grain boundary chemistry during tempering would be rather important if intergranular cleavage or Charpy impact energy is strongly dependent on chemistry of the grain boundary. An AES study of the intergranular cleavage surface obtained in an Fe-12Mn alloy was conducted for examining the varying chemistry on the prior austenite grain boundary, especially the Mn concentration. The variation of the Mn content during tempering was determined with the peak height ratio (PHR) of the Mn Auger peak at 542 eV and the Fe peak at 703 eV. This ratio of Mn_{542} and Fe_{703} demonstrates a very definite variation in intergranular fracture surface chemistry during tempering. It is, however, difficult to determine chemical composition directly from this PHR. Figure 37 shows the variation in Mn concentration on the intergranular cleavage surfaces during tempering. As revealed by the curve, the PHR of Mn and Fe Auger peaks remains constant until the tempering temperature was raised above 300°C and then the PHR achieves a maximum value, approximately 38%, at 400°C. At higher temperatures, the PHR decreases to a slightly higher level than the primary PHR, which is about 13%. The variation of the PHR of Mn and Fe, on isothermal treatment, is shown in Figure 38. The PHR curve shows an abrupt increase with holding time until 1 hour, after which grain boundary Mn enrichment is maximized. After 1 hour, the PHR gradually decreases to 28% on 280 hours treatment.

The chemistry of intergranular fracture surface of the boron-modified Fe-12Mn alloy during heat treatment was regarded as rather difficult to analyze due to its tendency for transgranular fracture. However, the embrittling treatment on this alloy

reveals an intergranular fracture surface. To monitor the change of fracture surface chemistry of the boron-added steel, an isothermal treatment at 450°C was conducted. Figure 39 shows the variation of Charpy impact energy of the specimen fractured at LNT with holding time up to 200 hours. The increase of holding time accompanied a gradual increase in Charpy impact value. Hardness remains relatively constant throughout the treatment. The upper curve of Figure 39 illustrates a decrease of intergranular fracture mode with holding time. This is also clearly seen in fractographs of Figure 40. The variation in intergranular fracture surface chemistry of the boron-modified Fe-12Mn alloy during isothermal treatment was successfully investigated by an AES study of the intergranular fracture surface exposed after fracturing. AES spectra obtained from the specimen which was isothermally heat treated for 1 hour, 10 hours, and 40 hours are shown in Figures 36, 41, and 42, respectively. Careful examination of these spectra is expected to show possible changes in Mn and B contents on the intergranular fracture surface. As illustrated in Figure 43, there are two significant curves which show the changes in the Mn and B contents. The upper curve in Figure 43 represents the change of PHR of Mn and Fe, which shows that Mn concentration on the intergranular fracture surface abruptly increase during treatment until 1 hour and slowly decreases to about 18% of PHR. This curve of the boron-modified alloy follows the same trend as that of an Fe-12Mn without the boron addition. The lower one shows the nearly consistent PHR of B and Fe during isothermal treatment. Ti was excluded due to its consistency throughout the heat treatments.

The Mn enriched region as well as C or B segregation, along the prior austenite grain boundaries was confirmed by the Ar^+ ion-sputtering technique, which was described in an earlier section. The sputtering profile obtained by this technique not only gives evidence of enrichment within one monolayer, but also makes it possible to calculate the thickness of the enriched region in *angstrom*. The sputtering profiles in Figure 44 show the changes in Mn and C contents with sputtering depth in the speci-

mens which were tempered at 250°C for 1 hour and 400°C for 1 hour, respectively, after austenitizing. The Mn concentration in the embrittled specimen dramatically decreases to that of the bulk composition after 0.2 minutes sputtering and C concentration follows the same trend as described in the previous section. The boron-modified Fe-12Mn alloy austenitized and tempered at 450°C for 1 hour shows the same characteristics of the sputtering profile of Mn contents as that of an identically treated Fe-12Mn steel without boron, as illustrated in Figure 45. The only difference between the two specimens is recognized as the existence of boron instead of carbon in the boron-added alloy.

In order to investigate the segregation of Mn in Fe-12Mn alloys with and without boron additions by comparing the same embrittling phenomena, AES studies combined with Ar^+ ion-sputtering of the embrittled specimens on the isothermal heat treatment were performed. The Mn sputtering profiles obtained by Fe-12Mn without boron were shown in Figures 46-49. An Fe-12Mn alloy on the isothermal treatment at 400°C after austenitizing shows the variation of the Mn-enriched region on the intergranular fracture surfaces. The Mn-enriched region gradually increases as holding time progresses, while the Mn concentration abruptly increases until 1 hour and gradually decreases. The boron-modified alloy also shows the same characteristics of sputtering profiles as the alloy without boron, which is illustrated in Figures 45, 50, and 51. These sputtering profiles indicate that Mn segregated to the grain boundaries during tempering either at 400°C or 450°C for 1 hour and the chemistry of intergranular fracture surface was changed due to its microstructural change along the prior austenite boundaries. Figures 52 and 53 show the variation of the Mn-enriched region with the holding time on the intergranular fracture surfaces in the specimens with and without boron additions, respectively. Calculations of the enriched region were performed, based on the method described earlier, the trend is the same for both alloys except for the existence of boron segregation. These phenomena will be discussed later in relation to microstructural

changes on the grain boundaries.

Figure 54 displays the TEM micrograph of the prior austenite grain boundary in the embrittled (400°C/1hr) Fe-12Mn steel and the EDAX analysis on the grain boundary. The scanning transmission electron analytical microscopic (STEM) technique always shows an advantage in quantitative analysis with the microstructure. Since the Mn-enriched region from this embrittling phenomenon is far less than the STEM resolution capability (40 Å minimum spot size), the EDAX study of the austenite boundary shows only that the grain boundary has quantitatively more Mn than the matrix by a factor of two. This STEM analysis, however, agrees well with the formation of the Mn-enriched region studied by an AES analysis.

3. Microstructure.

Microstructural changes on the prior austenite grain boundaries during tempering were examined because the chemistry of intergranular fracture surface was found to vary significantly with tempering after austenitizing. The optical microstructures of the tempered Fe-12Mn without boron addition are shown in Figure 54. Tempering up to 450°C for 1 hour did not affect the optical microstructures even though Mn segregated to and formed an enriched region along the boundaries during this heat treatment, as shown in Figure 55a and 55b. Figure 55c clearly shows the prior austenite grain boundaries which, upon close examination, show the presence of a newly nucleated phase. The optical micrograph of Figure 55d shows that this new phase formed from austenite nucleation growing rapidly along the prior austenite boundaries to a recognizable size. These microstructures obtained after tempering and quenching are fresh martensite (denoted by the lighter phase) and tempered martensite (dark phase).

As described earlier, an Fe-12Mn alloy without boron failed intergranularly below the DBTT and thus, the fracture surface reveals the intergranular cleavage facet along the prior austenite boundaries. The fractographs shown in Figure 56 represent the microstructural change on the austenite boundaries. The fractographs of Figure 56a

and 56b which were obtained from the specimens tempered at 250°C and 400°C, respectively, show no change in grain boundary microstructure during tempering. The intergranular fracture surfaces remained rather flat and smooth until tempering temperature was raised above 400°C. Figure 56c shows that the specimen tempered at 550°C has relatively irregular boundaries which are different from the specimen tempered at lower temperatures. A higher temperature of 650°C brought more irregular intergranular fracture surfaces, as illustrated in Figure 56d. By comparing these fractographs with optical microstructures, it was noticed that the specimen always failed along the prior austenite boundaries and that the irregularity on the fractured surface is almost equal to the size of newly nucleated austenite phases which were shown in the optical micrographs. This irregularity on the grain boundaries is closely associated with austenite nucleation and growth during tempering. The microstructure change on the isothermal treatment was illustrated in the fractographs of Figure 57 and optical micrographs of Figure 58. Optical microstructures as well as fractographs clearly show the change from a flat and smooth surface to an irregular surface as hold time at 400°C increases.

The irregularities on the intergranular fracture surfaces (Fig. 56) can be explained by two possibilities, which are illustrated by the TEM micrographs. Firstly, the prior austenite grain boundaries were changed from the typical straight, flat boundaries to irregular boundaries by the intrusion of second phases between α -martensite phases. A TEM micrograph of the intrusion of second phases between α -martensite phases of the embrittled (400°C/1 hr) specimen shown in Figure 60a displays the unaffected and preserved boundaries while a long tempered (400°C/200 hrs) specimen displays different boundaries as shown in Figure 60 b. The TEM micrograph in Figure 60b reveals that the phases between the blocky α -martensite structures grew and intruded the previous straight boundaries. This intrusion of either retained austenite or ϵ -martensite into the boundaries turned out to be the irregularity of the intergranular

cleavage facets which were revealed after fracturing. Secondly, the preferential austenite nucleation along the boundaries formed after Mn enrichment, made the boundary irregular. A TEM micrograph of the long-tempered specimen shown in Figure 61a displays the microstructures along the austenite boundaries. From the schematic diagram of 61b, it can be clearly seen that the prior austenite boundaries have small new austenite grains (transformed to fresh martensite) and after fracturing, the fracture surface shows the observed irregularity. These TEM micrographs are well matched with the fractographs of Figures 56 and 57.

The boron-modified Fe-12Mn alloy presumably shows a similar trend, but due to its transgranular fracture during tempering except for the embrittling treatment around 450°C, there can be no comparison of fractographs to show the changes in grain boundary microstructures. Isothermal treatment at 450°C, however, shows a rather definite grain boundary microstructural change with time revealing the intergranular fracture surface. As holding time increases, the fraction of intergranular fracture (Fig. 39) gets smaller and grain boundaries gradually change from the flat, smooth surface to a rather irregular one as shown in Figure 59, hence, the grain boundary irregularity of the boron-modified Fe-12Mn alloy which was shown in the fractographs presumably has two sources; one is from the austenite nucleation and growth and the other from the boron

IV. DISCUSSION

A. Intergranular Embrittlement of Fe-12Mn in the As-Austenitized Condition.

1. The source of intergranular brittleness: chemistry.

Intergranular fracture due to crack propagation along prior austenite grain boundaries in Fe-12Mn alloy in the as-austenitized condition was well documented by Hwang and Morris (14-16,19). It was assumed that the typical sources of intergranular fracture are the segregation of metalloids to the austenite boundaries (20-32) and the formation of a deleterious second phase on the boundaries (39,40,60). The previous conclusion that the intergranular brittleness in Fe-12Mn arises from neither of these causes, but is from its inherent microstructure (14), lead to a further investigation concerning possible chemical sources on the grain boundaries. Since an attempt to reveal the second phase along the boundaries never succeeded, the effect of a deleterious second phase on intergranular embrittlement was excluded and thus, most of these studies were focused on individual chemical species found by employing high resolution SAM.

Many investigations (29,69-71), attempted to relate the existence and extent of impurity segregation to decreasing cohesive strength of the interphase boundaries as a consequence of especially P or S segregation. The impurity segregation which could affect the boundary failure should present a suitable amount of impurities on the boundaries. Detection of the existence and the amount of chemical species on the intergranular fracture surface varies with the sensitivity of the Auger spectrometer, involving spatial and spectroscopic resolution. A primary interest lies in the detection of P segregation on the boundaries, since chemical composition of the bulk material (Table I) shows a very small amount of P. High resolution SAM studies using high sensitivity nevertheless never show a reasonable amount of P (more than 0.1 atomic percent) on the intergranular fracture surface. Segregation of S is thought to be one of the sources of the tempered martensite embrittlement of high purity steel (37,38). Occasionally a

relative large S Auger peak was detected, but this S peak came not from the segregation of S but from sulfide precipitates on the boundaries (Figures 11 and 12).

The effect of oxygen on intergranular fracture has been extensively investigated in many alloys, especially with high temperature mechanical tests (72-76). Grain boundary diffusion of oxygen in addition to oxidation is assumed to accelerate this oxygen-induced intergranular embrittlement. However, detection of oxygen is considered to be the most difficult AES analysis, even in the ultra high vacuum, due to the fast build-up of oxygen contamination on the fracture surface. However, like the S Auger peak, the source of the O Auger peak results not from segregation, but from oxide precipitates (MnO_2) on the grain boundaries. The minor second phase which is not continuous along the grain boundaries may affect the grain boundary properties, but the observed precipitates on the fracture surface facet are very rare in number and the denuded grain boundary facets show little plasticity. However, due to the sulfur segregation on the precipitate surface, it is recognizable that those precipitates were easily differentiated from the matrix (Figures 12 and 13).

The roles of C and N in alloy design are important issue. It is reported that C or N not only enhances the strength (77,78) of most steel alloys, but also affects their fracture modes (34,79-82). The N Auger peak appeared on the fracture surface in the specimen austenitized at 1100°C for more than 40 hours. Since the intergranular fracture appeared the absence of N peak shown in Figure 9, nitrogen is assumed not to be the source of the intergranular embrittlement. As reported by McMahon (82), increasing the carbon content showed the beneficial effect of suppressing the intergranular intergranular fracture. Carbide formation, however, promoted to intergranular fracture (33,34), but attempts to show active carbon contents on the prior austenite grain boundaries to influence the cohesive strength of the boundaries were unsuccessful. The present AES study represents the carbon contents on the intergranular fracture surface in Table III. The chemical analysis was very carefully conducted, usually within 5

minutes after being fractured before the C can build up under an ultra-high vacuum. If the impurity segregation on the prior austenite boundaries is considered when the alloy undergoes intergranular fracture, according to other cases (10-32,70), about 0.4 atomic percent carbon which segregated during austenitizing is believed to be insufficient to affect the fracture mode. Also, the boron-modified alloy, which was subjected to an embrittling treatment, shows intergranular fracture in the absence of carbon. The roles of carbon and nitrogen, however, remain unsolved and require further investigation.

2. The source of intergranular brittleness: microstructure.

The cause of the intergranular brittleness of Fe-12Mn in the as-austenitized condition does not appear to be due to segregation of deleterious species. Nor is brittleness caused by a microstructural disturbance such as the formation of a precipitate or a second phase on the prior austenite grain boundaries. From the results obtained by high resolution AES and TEM studies, it seems more plausible to detect the source of the intergranular weakness in the inherent resistance of the internal microstructure to the transgranular cleavage mode.

The previous work by Hwang and Morris (16,19) detailed the characteristic microstructure of Fe-12Mn steel in the as-austenitized condition. Typically in the Fe-12Mn alloy, a competing transformation of the present austenite to the hexagonal ϵ -martensite phases intrudes during the $\gamma \rightarrow \alpha$ transformation. The intrusion of the ϵ -martensite phases results in a substantial change in the substructure of the alloy with a unique, blocky type, dislocated α -martensite divided by regions which contain ϵ -martensite, as shown in Figure 20. This rather irregular substructure formed on cooling Fe-12Mn after austenitizing furnishes the alloy with a high resistance to transgranular cleavage fracture. Consequently, when the alloy undergoes brittle fracture, the fracture path is preferentially intergranular rather than transgranular. On the other hand, the Fe-8Mn alloy forms a lath martensite structure on cooling which resembles that of a typical Fe-Ni steel of intermediate nickel content (83). As in the Fe-Ni steels, the

substructure of Fe-8Mn consists of well-aligned lath martensite and provides preferable cleavage fracture through packets of adjacent laths (14). The comparison between two substructures of Fe-12Mn and Fe-8Mn alloy offers a straight forward explanation of the difference between the intergranular failure of Fe-12Mn and the transgranular cleavage fracture of Fe-8Mn tested below its DBTT.

The mechanism of fracture in an Fe-12Mn is also illustrated by the schematic diagram, as shown in Figure 62. Ductile-to-brittle transition behavior is well described by the yield strength (σ_y), the fracture stress for transgranular cleavage (σ_{fc}) and the fracture stress for intergranular cracking (σ_{fgb}). The fracture stresses are assumed relatively insensitive to temperature. The ductile-to-brittle transition is then associated with a change in the fracture mode from ductile rupture to brittle fracture when the yield strength rises above the lower of the two critical fracture stresses. While the inherent strength of the grain boundaries (σ_{fgb}) for both alloys was assumed comparable, the transgranular cleavage fracture stress (σ_{fc}) in Fe-12Mn is assumed higher than that in Fe-8Mn due to their submicrostructures. As a consequence, the Fe-12Mn alloy with its inherent microstructure always failed intergranularly because $\sigma_{fgb} < \sigma_{fc}$. However, the effect of grain boundary chemistry on σ_{fgb} is uncertain and will be discussed later.

B. Effect of Boron Segregation

1. Segregation of boron.

The basic approach to segregation behavior was first described by Langmuir (84) by using saturated type of solid/gas adsorption. His assumptions of fixed saturation level and no adsorbate interactions were inadequate. A more satisfactory derivation was proposed for grain boundary segregation by McLean (85), who provides a relatively desirable equation which minimizes of the free energy (by using vacant lattice sites and grain boundary adsorption energy). His model was criticized, modified and extended to

represent the ternary regular solution model of Guttman (86). While McLean's model, in general, shows that segregation rises as the solute content rises and the temperature falls, the equation developed by Guttman involves the interaction coefficients which are more important in evaluating the amount of segregation.

The equilibrium segregation of impurities such as P, S, and Sb was widely studied in order to explain the consequences of tempered embrittlement and tempered martensite embrittlement of steel alloys because of the availability of surface sensitive instruments. These embrittling phenomena involved two different heat treatments which might control impurity segregation to the prior austenite grain boundaries; austenitizing and tempering treatment. Most segregations to the austenite grain boundaries (which might be sufficient to affect the grain boundary cohesive strength) are believed to proceed during austenitizing. However, due to easy access to monitoring the change of grain boundary chemistry from embrittling treatment (tempering after austenitizing), studies of equilibrium segregation of impurities during tempering were widely performed. The segregation of boron in the boron-modified Fe-12Mn alloy is mainly restricted to austenitization due to its simple treatment. The austenite grains in an Fe-12Mn also have crystallographically high angle boundaries and thus provide most preferable vacant sites for impurity segregation during austenitizing treatment (87-89).

The boron-added Fe-12Mn alloy austenitized at 850° for 1 hour showed the 100% intergranular fracture and made it possible to determine the boron contents on the boundaries at this temperature. The boron contents from austenitizing treatment at higher than 900°C obtained by an AES study of the austenitized (1000°/1 hr/WQ) and tempered (650°/10 min/WQ) specimen because this treated specimen showed the 100% intergranular fracture mode and the change of boron contents by short tempering (10 min) is believed not to be significant from low diffusivity of boron at 650°C and most of the B segregation occurred during austenitizing. The relative boron contents were also confirmed by the autoradiography works (19,90). As shown in Table V, the boron

content on the prior austenite boundaries increases as the austenitizing temperature is raised. This result is contrary to other work on equilibrium segregation (91). However, the increase of austenitizing temperature causes the grain size to increase from 15μ at 850°C to approximately 85μ at 1000°C . This increase in grain size could affect the boron content on the boundaries because the grain boundary area would decrease along with the fixed boron contents in the matrix. It is also assumed that the kinetics of boron diffusion at different temperatures played a practical role in affecting segregation. As a consequence, the optimized boron content (3 atomic percent), segregated to the prior austenite grain boundaries from the austenitizing treatment ($1000^{\circ}/1$ hr), could carry its most beneficial effect on the grain boundary cohesive strength.

TABLE V

Heat Treatment		Mn	B	Fe
850°C, 1 hr	Grain boundary	12.7	1.1	Bal.
	Matrix	12.6	-	Bal.
900°C, 1 hr	Grain boundary	12.8	1.8	Bal.
	Matrix	12.8	-	Bal.
1000°C, 1 hr*	Grain boundary	(29.0)	2.9	Bal.
	Matrix	12.7	-	Bal.
1000°C, 1hr and 450°C, 1 hr	Grain boundary	28.4	2.9	Bal.
	Matrix	12.7	-	Bal.
450°C, 40 hrs	Grain boundary	17.1	2.4	Bal.
	Matrix	12.6	-	Bal.

* The specimen was embrittled at $650^{\circ}\text{C}/10$ min after austenitizing treatment ($1000^{\circ}\text{C}/1\text{hr}/\text{WQ}$).

2. The beneficial effect of boron segregation.

A microaddition of boron in medium carbon steel was found to improve its ductility as well as impact toughness at low temperature. Pyatakava and his coworkers (92-95) concluded that boron segregation may lead to a uniform microstructure to relieve local stresses from an uneven distribution of carbon and/or carbide precipitates. Other works (96-98) showed that boron appears to be exceptionally beneficial in that it segregates to austenite grain boundaries and improves creep-rupture life and ductility. These effects were attributed to the formation of more stable boron-precipitates or retardation of oxygen diffusion along the grain boundaries. However, none of these works proposed the improvement of the cohesion of the grain boundaries by boron segregation. Previous work by Hwang and Morris (19) implies that the segregation of boron may be attributed to the increase of the net change in surface energy per unit area of fresh fracture surface by reducing the grain boundary tension due to grain boundary surfactant, and this increase causes the suppression of DBTT. In this study, a more quantitative approach to investigate the effect of boron on surface tension was not carried out due to its intrinsic complexity.

TEM microstructures (Fig. 27) show the typical blocky α -martensite in the austenitized (1000°/1 hr/WQ) specimen. This boron-modified specimen displays no TEM microstructural difference from an Fe-12Mn without boron addition. Furthermore, the increase in austenitizing temperature from 850°C to 1000°C did not affect its TEM microstructure. However, if we compare the fractographs of two different specimens with and without boron additions (Figure 8 and Figure 29, respectively), there appear to be significantly different in the intergranular fracture surfaces in that the boron-added alloy displays more plastic deformation along the boundary than does the alloy without boron. This plastic deformation develops more significantly when the boron alloy was austenitized at a higher temperature (Figure 29). Since the boron content on the boundary is believed to be the only factor (Table V), the increase in boron

content along the boundary enhances the resistance to a fracture path along the prior austenite grain boundaries and a totally transgranular fracture mode (Figure 30) is presumably due to the increase of grain boundary cohesive strength by optimized segregation of boron to the boundary. This 'gluing effect' of boron appears speculative and needs further investigation.

C. Effect of Tempering.

1. Tempered martensite embrittlement.

Embrittlement in ferritic Fe-Mn alloys were reported by several workers (11,99). In this study the tempered martensite embrittlement in Fe-12Mn alloys with and without boron addition could be described as raising the DBTT by 150°C. This DBTT increase would be the main consequence of the formation of a Mn-enriched region along the prior austenite grain boundaries as shown in the present observations. The possibility of Mn enrichment on the austenite boundaries during tempering could be predicted to be due to the following reason: the tempering effects in Fe-Mn alloys are assumed to provide more vacant sites along the high angle grain boundaries in the highly dislocated martensite structure during tempering. The dislocation interaction along the high angle boundaries during tempering is rather speculative, but, in most cases, the dislocation density in matrix during tempering greatly decreases (100) and presumably the decrease in dislocation density results in more vacant sites for manganese segregation to the austenite boundaries during tempering. Since Mn segregation to the austenite boundaries requires both sufficient vacant sites along the boundaries and a low free energy of segregation, the following two factors could explain this segregation phenomenon which is assumed to cause the DBTT increase: 1.) more vacant sites on the boundaries provided during tempering or 2.) the low vapor pressure of Mn. This segregation phenomenon could be easily confirmed by the following indirect evidence: As holding time at 400°C increases in Fe-12Mn steel, the amount of Mn segre-

gation abruptly increases and the Mn-enriched region was obtainable by a submicro scale diffusional process, as shown in Figure 37. However, the growth of the Mn-enriched region does not continue after 1 hour of tempering, reaching a 20\AA thickness. This is because the diffusion of the substitutional Mn atoms must be limited to short distances at the relatively low temperature of 400°C .

Tempered martensite embrittlement was widely investigated in many martensitic steels. The embrittlement causes a deterioration of toughness and the embrittling sites have been delineated to be either transgranular or intergranular. Thomas (39) and Ritchie, et al. (40) proposed the model which shows that thermally unstable retained austenites along the lath boundaries transform to carbide during low temperature tempering resulting in a transgranular fracture mode, while McMahon (60) and Banerji, et al. (37,38) showed that impurity segregation and carbide formation are the cause of the intergranular brittleness. The present experimental evidence follows neither of these embrittling models. From the experimental observations, it appears that there is no impurity segregation or carbide formation either along the prior austenite boundaries or the lath boundaries.

From the present observations, it was deduced that the segregation of Mn in these alloys is directly responsible for the TME. It is rather difficult to investigate the effect of Mn segregation on the embrittlement by any mechanical tests because the enriched regions are of submicron dimensions as described in Figures 52 and 53. However, two possible explanations can be drawn from the investigation. First, a hypothetically brittle interface forms between two thin layers of Mn-enriched and Mn-depleted regions. Depth profiles shown in Figures 44 and 46 display two different regions along the austenite grain boundaries. As the Mn-depleted region slowly disappeared as the holding time increased (Figures 49-50), the fraction of intergranular fracture decreased and finally settled to less than 5% (Figure 38). Second, the segregation of Mn causes inhomogeneity of solute atoms along the boundaries and may induce solution- harden-

ing along the boundaries as similarly described in other works (99,100). These solution-hardened regions provide an easy fracture path along the austenite boundaries.

As described earlier, the preference of fracture mode below the DBTT was made by the comparison between the fracture stress for transgranular cleavage (σ_{fc}) and the fracture stress for intergranular crackings (σ_{fgb}) as shown in Figure 62. The yield strength (σ_y) and the transgranular cleavage fracture stress (σ_{fc}) are assumed insensitive to the grain boundary chemistry. On the other hand, the intergranular cleavage fracture stress (σ_{fgb}) is not sensitive to temperature, but is increasing or decreasing depending on the grain boundary chemistry. Consequently, the Fe-12Mn without boron always display intergranular fracture because the σ_{fc} due to the formation of the enriched region, otherwise the σ_{fgb} is kept lower than the σ_{fc} due to the effect boron segregation.

2. Grain boundary chemistry and microstructure.

The chemical composition of the grain boundary has been regarded as one of the most important subjects when the alloy becomes embrittled, especially in an intergranular fracture mode. Much research work (29,64,101,102) have been done on the determination of grain boundary chemistry to interpret the intergranular embrittlement by using surface-sensitive instruments or scanning transmission electron microscopic studies. In most cases, solute enrichment at grain boundaries was restricted to the more common impurities in iron such as P, S, N, Sn and Sb. These solute atoms were found to be at grain boundary concentrations more than 10^2 times the bulk concentrations, which are at least several hundred ppm.

However, segregations of boron and manganese to the austenite boundaries in the Fe-Mn alloy during tempering are rather peculiar. Boron, in particular, strongly segregates to the austenite boundaries with the highest concentrations during austenitizing. The tempering treatment after austenitizing did not affect the amount of boron segregation (Figure 43). The boron concentrations on the boundaries remain nearly constant

even after long isothermal heat treatment at 450°C. The boron enrichment ratio between the boundary and the matrix was obtained with difficulty because the boron content in the matrix could not easily be detected (actual bulk content is 20 ppm). The enrichment ratio, however, is presumably higher than any reported ratios (104,105).

Manganese, as reported earlier, had not formed the enriched region along the austenite boundaries after austenitizing. The tempering treatment around 400°C promotes the manganese segregation to the boundaries. The Mn enrichment on the intergranular fracture surfaces suddenly reached its peak concentration at the embrittling temperature and slowly decreased as the tempering temperature or the tempering time increased (Figure 37). As shown in Figure 37, the Mn enrichment ratio in an Fe-12Mn boron-free alloy is approximately on the order of 3, while the boron-modified Fe-12Mn alloy has a slightly lower enrichment ratio. This is due to the amount of previous boron segregation. As demonstrated earlier (Figures 60 and 61), the chemistry of intergranular fracture surfaces studied by AES could not apply to the chemistry of the prior austenite grain boundaries because the change of grain boundary structures affects the fracture path along the boundaries and, thus, most of the AES analyses showed the chemistry of intergranular fracture surface, not exactly of the prior austenite grain boundaries. There is always competition between chemical species for grain boundary sites in many steels due to their different segregation free energies. In the present study, boron did not hinder manganese segregation to the austenite boundaries during tempering. The tendency of Mn enrichment during tempering in Fe-12Mn alloys with and without boron additions is identical.

The response of intergranular fracture surface chemistry to tempering treatment in the boron-added alloy is well described by the changes in the peak height ratios (PHR) for Mn/Fe and B/Fe (Figure 43). Thermodynamically, the PHR at grain boundaries will either increase or equilibrate with that of the matrix. However, the PHR, Mn/Fe decreases as the tempering time increases. This phenomenon may be explained

by the fractographs (Figure 56) and grain boundary microstructures (Figure 55). Mn segregation to the boundaries reaches approximately 32 atomic percent Mn after 1 hour tempering at 450°C. Longer tempering time provides for either the intrusion of ϵ phase into the boundaries or the nucleation of new austenite on the highly Mn-concentrated region (Figures 60 and 61). Other results on Ni-steel (106) had shown that newly nucleated austenite appears not only on the prior austenite boundaries but also along the lath boundaries during two-phase tempering because both boundaries furnished equal opportunity for nucleation from the highly dislocated martensite. The predominant austenite nucleation on the prior austenite boundaries can be easily confirmed by the optical micrographs of the tempered (650°C/1 hr) Fe-12Mn steel (Figure 55). The PHR change with respect to tempering temperature is virtually identical to the PHR change with respect to isothermal treatment time. Furthermore, the intergranular fracture surfaces from the fractographs of Figure 57 are also similar. As the PHR, Mn/Fe decreases, the irregularity along the prior austenite boundaries becomes more apparent, which suggests that nucleated austenite grain growth is occurring. This austenite grain growth along the prior austenite boundaries affects not only the change of PHR, Mn/Fe on the fracture surface, but also the fracture mode in the boron-modified steel. The intergranular fracture mode in the boron-modified Fe-12Mn steel after tempering at 450°C for 1 hour is caused by the Mn-enriched region (3 times higher than the matrix) along the boundaries. The Mn-enrichment ratio decreases during isothermal treatment through a change in the grain boundary structure from austenite grain growth. The Mn-enriched region has a very slow composition gradient from the intergranular fracture surface (Figure 49). The fracture mode then reverts to transgranular as in the as-quenched specimen. This conclusion is based on the similarity of the Mn enrichment ratios on the intergranular fracture surface of the Fe-12Mn alloy with and without boron additions.

V. CONCLUSIONS

The main results from the present research may be summarized as follows:

A. Intergranular Embrittlement of an Fe-12Mn in the As-Austenitized Condition.

1. The alloys fractured below the DBTT have an intergranular fracture mode, irrespective of grain size over the range of 15–250 μm .
2. High resolution AES analyses on the intergranular fracture surface revealed no consistent impurity segregation such as P, S, Sb, As or O, but did show a slight segregation of carbon. Some nitrogen, together with carbon, were found in the further austenitized (1100°C/100 hrs/WQ) specimen.
3. An occasional presence of S or O Auger peak on the intergranular fracture surface was associated with MnS or MnO₂ precipitates along the prior austenite boundaries.
4. Ar⁺ ion sputtering on the fracture surface showed equilibrium segregation of carbon with approximately 30Å depth to the boundaries, but not any Mn enrichment at the grain boundaries.
5. The intergranular brittleness of an Fe-12Mn alloy in the as-austenitized condition is not due to chemical changes on the prior austenite boundaries but is rather due to the microstructural effect on the preferential fracture path along the grain boundaries.

B. Effect of Alloying Elements on Intergranular Embrittlement.

1. A 20 ppm boron addition with 1000°C/1 hr/WQ heat treatment yielded the highest Charpy V-notch impact energy at LNT and changed the fracture mode from intergranular to transgranular.
2. The AES studies on the grain boundaries in the boron-modified alloy showed that the increase in concentration of boron segregation from 0.7 atomic percent to

about 3 atomic percent to the prior austenite boundaries results in the highest 'gluing effect' of boron.

3. Trace additions of Mg, Zr, or V in an Fe-12Mn steel hardly segregated to the grain boundaries during the austenitizing treatment and, thus, had negligible effects on the intergranular embrittlement.

C. Effect of Tempering in Fe-12Mn Alloys.

1. A 400° or 450°C tempering for 1 hour of the Fe-12Mn alloys without and with boron addition raised the ductile-brittle transition by 150°C. The tempered martensite embrittlement in Fe-12Mn alloys was found to be mainly due to a Mn-enriched region along the prior austenite boundaries.
2. The high resolution AES studies combined with Ar^+ ion-sputtering showed that the Mn-enriched region of the embrittled specimens was approximately 32 atomic percent Mn with boron addition and 38 atomic percent Mn without, with a 20Å thickness.
3. The change in Mn-enrichment on the intergranular fracture surfaces of the boron-modified Fe-12Mn alloy is directly associated with the change in the fracture mode as well as the CVN values.
4. After Mn enrichment further tempering causes preferential austenite nucleation along the prior austenite boundaries, affects the grain boundary microstructures, and changes the chemistry of intergranular fracture surfaces.

REFERENCES

- 1 G. R. Brophy and A. J. Miller: *Trans. ASM*, 1949, vol. 41, 1185.
- 2 B. E. Hopkins and H. R. Tipler: *J. Iron Steel Inst.*, 1958, vol. 188, 118.
- 3 W. Jolley: *J. Iron Steel Inst.*, 1968, vol. 206, 170.
- 4 W. C. Leslie, R. J. Sober, S. G. Babcock and S. J. Green: *Trans. ASM*, 1969, vol. 62, 690.
- 5 T. Ooka, H. Mimura, S. Yano, K. Sugino and T. Toizumi: *J. Japan Inst. Metals*, 1966, vol. 30, 442.
- 6 H. Sakurai, S. Yano, T. Inoue, H. Mimura and K. Aoki: *J. Japan Inst. Metals*, 1969, vol. 33, 856.
- 7 D. Mann: "LNG Material and Fluids", Cryogenic Div., Inst. for Basic Standard, NBS, 1st ed., 1977.
- 8 J. W. Morris, Jr., S. K. Hwang, K. A. Yuschenko, V. T. Belotzerkovetz and O. G. Kvasnerskii: *Advances in Cryogenic Engineering*, 1978, vol 24, 91.
- 9 M. J. Roberts: *Met. Trans.*, 1970, vol. 1, 3287.
- 10 A. Holden, J. D. Bolton and E. R. Petty: *J. Iron Steel Inst.*, 1971, vol. 209, 721.
- 11 J. D. Bolton, E. R. Petty and G. B. Allen: *Met. Trans.*, 1971, vol. 2, 2915.
- 12 S. K. Hwang, S. Jin and J. W. Morris, Jr.: *Proc. 4th Int. Conf., Strength of Metals and Alloys, Laboratoire de Physique des Solides, Nancy, France, 1976*, vol. 2, 842.
- 13 S. K. Hwang and J. W. Morris, Jr.: *Proc., USSR-US Seminar on Applied Problems of Low Temperature Materials, E. O. Paton Inst. of Electro-Welding, Kiev, USSR, 1976*.

- 14 S. K. Hwang: Ph.D. Thesis, University of California, Berkeley, 1977.
- 15 S. K. Hwang and J. W. Morris, Jr.: *Met. Trans.*, 1979, vol. 10A, 545.
- 16 S. K. Hwang and J. W. Morris, Jr.: *Advances in Cryogenic Engineering*, 1978, vol. 24, 137.
- 17 M. Niikura and J. W. Morris, Jr.: *Met. Trans.*, 1980, vol. 11A, 1531.
- 18 M. J. Schanfein, M. J. Yokota, V. F. Zackay, E. R. Parker and J. W. Morris, Jr.: *ASTM STP 579*, 1975, 361.
- 19 S. K. Hwang and J. W. Morris, Jr.: *Met. Trans.*, 1980, vol. 11A, 1197.
- 20 M. Guttman, P. R. Krahe, F. Abel, G. Amsel, M. Bruneaux and C. Cohen: *Met. Trans.*, 1974, vol. 5, 167.
- 21 R. Viswanathan: *Met. Trans.*, 1971, vol. 2, 809.
- 22 R. O. Ritchie: *Met. Trans.*, 1977, vol. 8A, 1131.
- 23 J. Q. Clayton and J. F. Knott: *Fracture 1977*, vol. 2, ICF4, Waterloo, Canada, June, 287.
- 24 C. J. McMahon, Jr., A. K. Cianelli and H. C. Feng: *Met. Trans.*, 1977, vol. 8A, 1055.
- 25 H. Ohtani, H. C. Feng and C. J. McMahon, Jr.: *Met. Trans.*, 1976, vol. 7A, 1123.
- 26 A. K. Cianelli, H. C. Feng and C. J. McMahon, Jr.: *Met. Trans.*, 1977, vol. 8A, 1059.
- 27 M. Guttman and P. R. Krahe: *Scrip. Met.*, 1971, vol. 5, 479.
- 28 C. L. Smith and J. R. Low, Jr.: *Met. Trans.*, 1974, vol. 5, 279.
- 29 Y. E. Glikman: *Fiz. metal. metalloved.*, 1968, vol. 26, 233.
- 30 P. Dumoulin, M. Guttman, M. Foucault, M. Palmier, M. Wayman, and M. Biscondi: *Metal Sci.*, 1980, January, 1.

- 31 J. Yu and C. J. McMahon, Jr.: *Met. Trans.*, 1980, vol. 11A, 277.
- 32 J. Yu and C. J. McMahon, Jr.: *Met. Trans.*, 1980, vol. 11A, 291.
- 33 C. L. Briant and S. K. Banerji: *Met. Trans.*, 1979, vol. 10A, 1729.
- 34 S. K. Banerji, C. J. McMahon, Jr. and H. C. Feng: *Met. Trans.*, 1978, vol. 9A, 237.
- 35 G. Delisle and A. Galibois: *J. Iron Steel Inst.*, 1969, December, 1628.
- 36 E. B. Kula and A. A. Anctil: *J. Metals*, 1968, vol. 4, 817.
- 37 C. L. Briant and S. K. Banerji: *Met. Trans.*, 1979, vol. 10A, p. 1151.
- 38 C. L. Briant and S. K. Banerji: *Met. Trans.*, 1981, vol. 12A, 309.
- 39 G. Thomas: *Met. Trans.*, 1978, vol. 9A, 439.
- 40 R. M. Horn and R. O. Ritchie: *Met. Trans.*, 1978, vol. 9A, 1039.
- 41 L. A. Harris: *J. Appl. Phys.*, 1968, vol. 39, 1419.
- 42 C. C. Chang: "Characterization of Solid Surfaces", Kane and Larrabee, eds., Plenum Press, 1974, 509.
- 43 P. W. Palmberg: "Electron Spectroscopy", D. A. Shirley, ed., 1972, 385.
- 44 R. L. Park: *Physics Today*, 1975, April, 52.
- 45 H. L. Marcus: *J. Metals*, 1977, vol. 29, 20.
- 46 B. Navinsek: *Prog. in Surf. Sci.*, 1977, vol. 7, 49.
- 47 H. L. Bay, J. Bohdansky and E. Hechtl: *Rad. Effects*, 1979, vol. 41, 77.
- 48 T. J. Chuang and K. Wandelt: *IBM J. Res. and Dev.*, 1978, vol. 22, 277.
- 49 P. S. Ho and J. E. Lewis: *Surf. Sci.*, 1976, vol. 57, 393.
- 50 P. S. Ho and J. E. Lewis: *Surf. Sci.*, 1979, vol. 85, 19.
- 51 P. S. Ho: *Surf. Sci.*, 1978, vol. 72, 253.

- 52 D. F. Stein, W. C. Johnson and C. L. White: "Grain Boundaries in Engineering Metal", G. A. Chadwick and D. A. Smith, eds., New York, Academic Press, 1976, 388.
- 53 L. E. Davis, N. C. McDonald, P. W. Palmberg, G. E. Riach and R. E. Weber: Handbook of AES, 2nd ed., 1976, Phy. Elec. Ind., Inc., Minnesota.
- 54 T. W. Haas, J. T. Grant and G. J. Dooley: "Adsorption-Desorption Phenomena", Ricca, ed., Academic Press, 1972, 359.
- 55 H. Schumann: Arch. Eisenhattenvesen, 1967, vol. 38, 743.
- 56 H. Schumann: Z. Metallk., 1967, vol. 58, 207.
- 57 H. Schumann: Arch. Eisenhattenwesens, 1967, vol. 38, 647.
- 58 J. B. Cohen, A. Hurlich and M. Jacobson: Trans. Amer. Soc. Metals, 1947, vol. 39, 109.
- 59 P. R. Krahe and M. Guttman: Metallography, 1974, vol. 7, 5.
- 60 C. J. McMahon, Jr.: "Grain Boundaries in Engineering Metals", J. L. Walter, et al., eds., Claitors Pub., 1974, 525.
- 61 C. J. McMahon, Jr., J. R. Rellick and B. J. Schultz: "Fracture", P. L. Pratt, ed., Chapman and Hall, 1969, 278.
- 62 R. L. Cairns and C. J. Novak: Met. Trans., 1971, vol. 2, 1837.
- 63 R. F. Decker and J. W. Freeman: Trans. TMS-AIME, 1960, vol. 218, 277.
- 64 G. S. Was, H. H. Tixhner and R. M. Latanision: Met. Trans., 1981, vol. 12A, 1397.
- 65 S. Jin, S. K. Hwang and J. W. Morris, Jr.: Met. Trans., 1975, vol. 6A, 1721.
- 66 C. K. Syn, S. Jin and J. W. Morris, Jr.: Met. Trans., 1976, vol. 7A, 1827.
- 67 M. Enomoto and E. Furubayashi: Mat. Sci. Eng., 1976, vol. 24, 123.

- 68 J. Koo and G. Thomas: *Met. Trans.*, 1977, vol. 8A, 525.
- 69 J. E. Doherty, B. H. Kear, A. F. Giamei and C. W. Steinke: "Grain Boundaries in Engineering Metals", J. L. Walter, et al., eds., Claitors Pub., 1974, 619.
- 70 T. Matsuyama and H. Suto: *Trans. JIM*, 1979, vol. 20, 44.
- 71 M. C. Inman and H. R. Tipler: *Acta Met.*, 1953, 185.
- 72 A. E. Dias and R. E. Reed-Hill: *Scrip. Met.*, 1979, vol. 13, 491.
- 73 C. Lea: *Met. Sci.*, 1979, May, 301.
- 74 R. H. Bricknell and D. A. Woodford: *Met. Trans.*, 1981, vol. 12A, 1673.
- 75 D. A. Woodford: *Met. Trans.*, 1981, vol. 12A, 299.
- 76 D. A. Woodford and R. H. Bricknell: *Met. Trans.*, 1981, vol. 12A, 1467.
- 77 T. G. Digges: *Trans. ASM*, 1938, vol. 26, 408.
- 78 E. D. Bain and H. W. Paxton: "Alloying Elements in Steel", ASM Pub., Metals Park, 1966.
- 79 T. Inoue: "Grain Boundaries in Engineering Metals", J. L. Walter et al., eds., Claitors Pub., 553.
- 80 T. E. Swarr and G. Krauss: *ibid.*, 127.
- 81 R. G. Rowe: *Met. Trans.*, 1979, vol. 10A, 997.
- 82 C. J. McMahon, Jr.: *Acta Met.*, 1966, vol. 14, 839.
- 83 J. W. Morris, Jr., C. K. Syn, J. I. Kim and B. Fultz: "International Conference on Martensitic Transformations (ICOMAT)", Cambridge, Mass., June 1979,
- 84 I. Langmuir: *J. Amer. Chem. Soc.*, 1918, vol. 40, 1361.
- 85 D. McLean: "Grain Boundaries in Metals", Oxford Univ. Press, 1957, 118.
- 86 M. Guttman: *Surf. sci.*, 1975, vol. 53, 213.

- 87 H. Taga and A. Youshikawa: *Trans. Iron Steel Inst., Japan (Suppl.)*, 1971, vol. 11, 1256.
- 88 T. M. Williams, D. R. Harris and J. Furnival: *J. Iron Steel Inst.*, 1972, vol. 210, 351.
- 89 G. F. Melloy, P. R. Slimmon and P. P. Podgursky: *Met. Trans.*, 1973, vol. 4, 2279.
- 90 J. D. Garnish and J. D. Hughes: *J. Mat. Sci.*, 1972, 7.
- 91 Y. Ohmori and K. Yamanake: "Boron in Steel", S. K. Banerji and J. e. Morral, eds., AIME, Milwaukee, Wisc., 1979, 44.
- 92 L. L. Pyatakova: *Steel in the USSR*, 1974, 994.
- 93 L. L. Pyatakova, M. V. Mozharov, M. A. Sirotkina and T. A. Dyuzheva: *Metal i Termich. Obrab. Metallov*, 1971, No. 2, 62.
- 94 V. I. Arkharov, L. L. Pyatakova and Ye. S. Markhasin: *Fiz. met. metallov.*, 1974, vol. 37, 661.
- 95 L. L. Pyatakova, I. I. Mints, T. G. Berezina and M. A. Sirotkina: *Metal i Termich. Obrab. Metallov*, 1976, No. 1, 39.
- 96 B. J. Thomas and G. Henry: "Boron in Steel", S. K. Banerji and J. E. Morral, eds., AIME, Milwaukee, Wisc., 1979, 80.
- 97 T. M. Williams: *Metal Sci. J.*, 1972, vol. 6, p. 68.
- 98 T. M. Williams, A. M. Stoneham and D. R. Harries: *Met. Sci.*, 1976, 14.
- 99 Ya. E. Goldsteyn, G. A. Charushnikova and A. M. Belikov: *Russ. Met. and Mining*, 1963, No. 4, 72.
- 100 J. Friedel: "Dislocations", Pergamon Press, Oxford, 1964, 224.
- 101 J. H. Westbrook and K. T. Aust: *Acta Met.*, 1963, vol. 11, 1151.

- 102 K. T. Aust, R. E. Hanneman, P. Niessen and J. H. Westbrook: *Acta Met.*, 1968, vol. 16, 291.
- 103 M. Guttman, P. R. Krahe, F. Abel, G. Amsel, M. Bruneaux and C. Cohen: *Met. Trans.*, 1974, vol. 5, 167.
- 104 I. N. Shabanova, A. B. Kutin, L. V. Smirnov and V. A. Trapeznikov: *Fiz. metal. metallov.*, 1976, vol. 42, 318.
- 105 R. V. Ramasubramaniun and D. F. Stein: *Met. Trans.*, 1974, vol. 4, 1735.
- 106 R. H. Jones, S. M. Bruemmer, M. T. Thomas and D. r. Baer: *Met. Trans.*, 1981, vol 12A, 1621.
- 107 J. I. Kim: Ph.D. Thesis, University of California, Berkeley, 1979.

FIGURE CAPTIONS

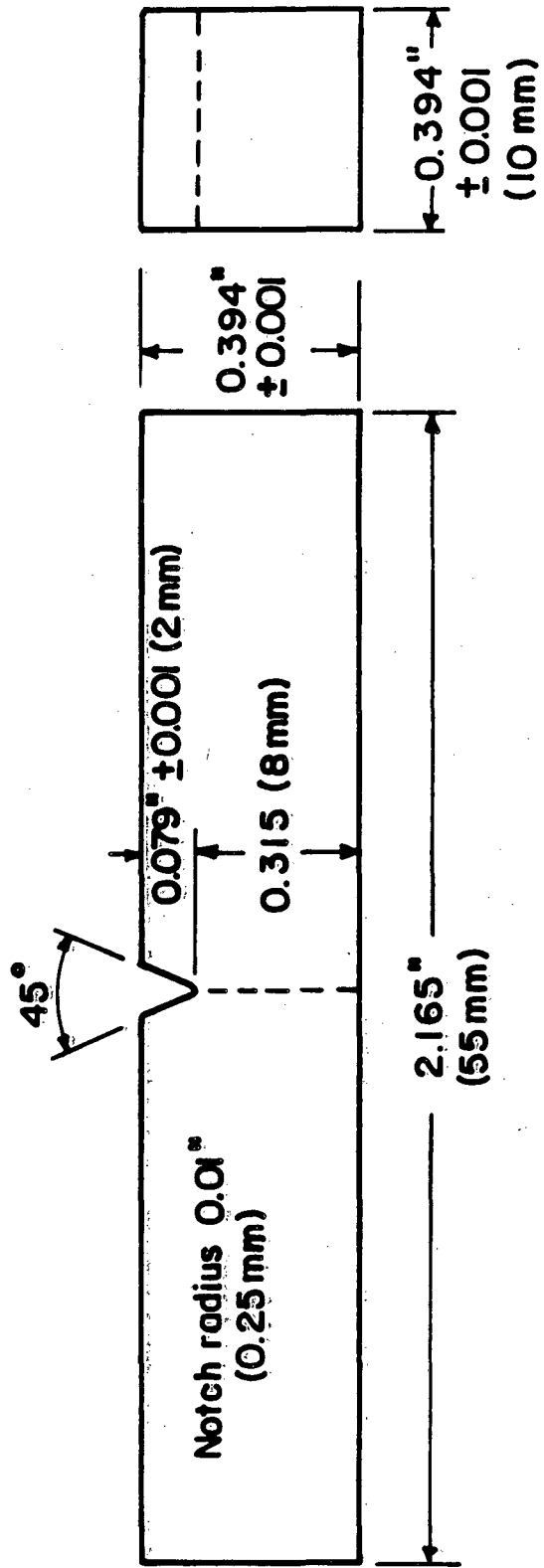
- 1 Standard Charpy impact test specimen.
- 2 Dilatometry specimen for measuring phase transformation temperature.
- 3 Single notched AES specimen for fracturing.
- 4 Schematic diagram of the ultra high vacuum reaction chamber with *in-situ* fracturing and cooling stage for AES study.
- 5 Ductile-brittle transition in austenitized (1100°C/2hr/WQ) Fe-12Mn.
- 6 SEM fractographs taken from Charpy specimens tested (a) above the DBTT and (b) below the DBTT.
- 7 Changes of structures and properties on austenitizing for 2 hours (a) grain size (b) hardness at room temperature (c) Charpy impact energy at LNT.
- 8 SEM fractographs of Fe-12Mn steel tested below the DBTT after austenitizing at 850°C/2hrs, 1000°C/2hrs, 1100°C/2hrs, and 1200°C/2hrs, respectively.
- 9 AES spectrum obtained from intergranular fracture surface of the specimen austenitized at 1100°C/2hrs/WQ) and SEM fractograph.
- 10 AES spectra obtained from intergranular fracture surfaces of the specimen austenitized at 1100°C for 2 hours and 100 hours, respectively.
- 11 SEM-EDAX analyses of particles on the intergranular fracture surface.
- 12 SEM-AES analyses of (a) sulfide particle, (b) manganese particle, (c) crater made by a particle which was separated from the grain boundary, and (d) intergranular fracture surface.
- 13 AES spectra obtained from (a) the sputtered surface and (b) the sputtered surface of an austenitized (1100°C/2hrs/WQ) specimen.

- 14 Partial AES spectra of (a) the unsputtered surface and (b) the sputtered surface showing the disappearance of carbon peak.
- 15 Partial AES spectrum obtained from the intergranular fracture surface with higher sensitivity.
- 16 Depth profiles obtained from the intergranular fracture surfaces of the specimens austenitized at 1100°C (a) for 2 hours and (b) for 100 hours, respectively.
- 17 AES spectra obtained from (a) the unsputtered surface and (b) the sputtered surface of an austenitized (1100°C/100hrs/WQ) specimen.
- 18 Residual gas analysis of inside reaction chamber at ultra-high vacuum.
- 19 Optical micrographs of Fe-12Mn specimens austenitized at (a) 850°C and (b) at 1100°C.
- 20 TEM micrograph of Fe-12Mn specimen austenitized at 1100°C for 2 hours.
- 21 TEM micrograph of Fe-12Mn specimen. (a) bright field image and (b) dark field image.
- 22 Changes of Charpy impact energy at LNT as a function of boron contents.
- 23 Changes of Charpy impact energy of an Fe-12Mn with 20 ppm B at LNT on austenitizing treatment.
- 24 Fractographs showing the different austenite grain sizes on austenitizing treatment.
- 25 SEM fractographs showing the fracture modes on 1 hour austenitizing treatment at (a) 850°C, (b) 900°C, (c) 950°C, and (d) 1000°C.
- 26 AES spectrum obtained from the austenitized (850°C/1hr/WQ) specimen with boron additions.
- 27 AES spectrum obtained from the austenitized (900°C/1hr/WQ) specimen with boron additions.
- 28 TEM micrograph of the boron-modified Fe-12Mn alloy austenitized at 1100°C for 1 hour followed by water quenching.

- 29 SEM fractographs showing the fracture surface of austenitizing treatment at (a) 850°C and (b) 900°C.
- 30 SEM fractographs showing the transgranular fracture mode obtained from the austenitized (100°C/1hr/WQ) specimen.
- 31 Changes in Charpy impact energy at 77°K as a function of tempering temperature.
- 32 SEM fractographs showing the fracture modes on tempering treatment at (a) and (b) 250°C, (c) and (d) 350°C, (e) a and (f) 450°C, (g) and (h) 550°C, and (i) and (j) 650°C.
- 33 Shift of ductile-brittle transition temperature by tempered martensite embrittlement in a boron-modified Fe-12Mn.
- 34 Shift of ductile-brittle transition by tempered martensite embrittlement in an Fe-12Mn without boron additions.
- 35 AES spectra obtained from the tempered specimen at (a) 250°C and (b) 400°C.
- 36 AES spectrum obtained from the boron-added Fe-12Mn tempered at 450°C for 1 hour.
- 37 Changes in peak height ratio of Mn_{542} and Fe_{703} Auger peaks as a function of tempering temperature.
- 38 Changes in peak height ratio of Mn_{542} and Fe_{703} Auger peaks as a holding time at 400°C.
- 39 Changes of structures and properties on tempering (a) fraction (%) of intergranular fracture mode, (b) hardness at room temperature, (c) Charpy impact energy at LNT.
- 40 SEM fractographs showing the fracture modes on isothermal treatment at 450°C for (a) 1 hour, (b) 2 hours, (c) 80 hours, and (d) 200 hours.

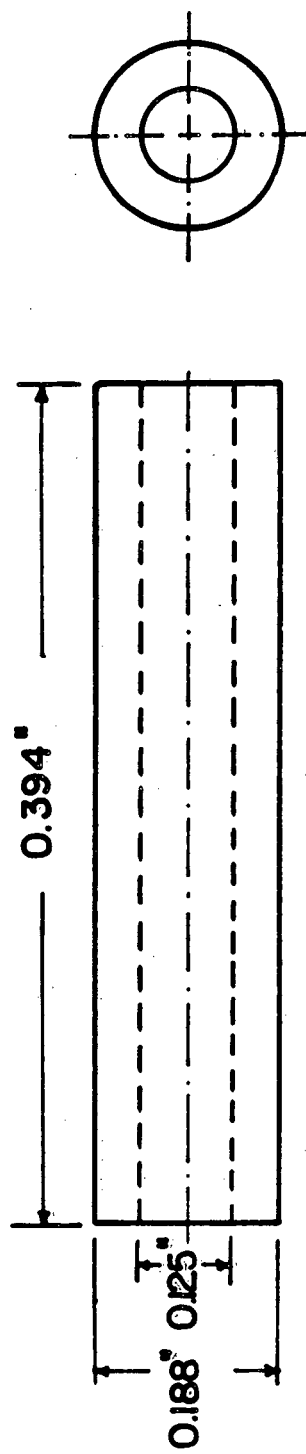
- 41 AES spectrum obtained from the tempered (450°C/1hr/WQ) specimen.
- 42 AES spectrum obtained from the tempered (450°C/40hrs/WQ) specimen.
- 43 Changes in peak height ratio of Mn/Fe and B/Fe Auger peaks as a function of holding time at 450°C.
- 44 Depth profiles obtained from an Fe-12Mn on tempering treatment at 250°C and 400°C.
- 45 Depth profile obtained from the tempered (450°C/1hr/WQ) Fe-12Mn with the boron additions.
- 46 Depth profile obtained from the tempered (400°C/10min/WQ) Fe-12Mn.
- 47 Depth profile obtained from the tempered (400°C/1hr/WQ) Fe-12Mn.
- 48 Depth profile obtained from the tempered (400°C/48hrs/WQ) Fe-12Mn.
- 49 Depth profile obtained from the tempered (400°C/290hrs/WQ) Fe-12Mn.
- 50 Depth profile obtained from the tempered (450°C/10hrs/WQ) Fe-12Mn with the boron additions.
- 51 Depth profile obtained from the tempered (450°C/20hrs/WQ) Fe-12Mn with the boron additions.
- 52 Changes in Mn-enriched depth as a function of holding time at 400°C in an Fe-12Mn alloy.
- 53 Changes in Mn-enriched depth as a function of holding time at 450°C in the boron-modified Fe-12Mn alloy.
- 54 TEM-EDAX analyses of grain boundary and matrix in Fe-12Mn alloy tempered at 400°C for 1 hour.
- 55 Optical micrographs of Fe-12Mn specimens on tempering treatment at (a) 250°C, (b) 400°C, (c) 550°C, and (d) 650°C.

- 56 SEM fractographs of Fe-12Mn specimens showing the fracture surfaces on tempering treatment at (a) 250°C, (b) 400°C, (c) 550°C, and 650°C.
- 57 SEM fractographs of Fe-12Mn specimens showing the fracture surfaces on isothermal treatment at 400°C for (a) 1 hour, (b) 3 hours, (c) 6 hours, (d) 12 hours, (e) 24 hours, and (f) 48 hours.
- 58 Optical micrographs of Fe-12Mn specimens on isothermal treatment at 400°C for (a) 1 hour, (b) 3 hours, (c) 6 hours, (d) 12 hours, (e) 24 hours, and (f) 48 hours.
- 59 SEM fractographs of the boron-modified Fe-12Mn specimens showing the fracture surfaces on isothermal treatment at 450°C for (a) 1 hour, (b) 20 hours, (c) 80 hours, and (d) 200 hours.
- 60 TEM micrographs of Fe-12Mn specimens tempered at 400°C for (a) 1 hour and (b) 200 hours.
- 61 TEM micrograph of Fe-12Mn specimen tempered at 400°C for 200 hours and schematic diagram showing the newly nucleated austenite grains along the prior austenite grain boundaries.
- 62 Schematic diagram showing the fracture mode below the DBTT in an Fe-12Mn alloy.



XBL 8110-6792

Figure 1



XBL8110-679I

Figure 2

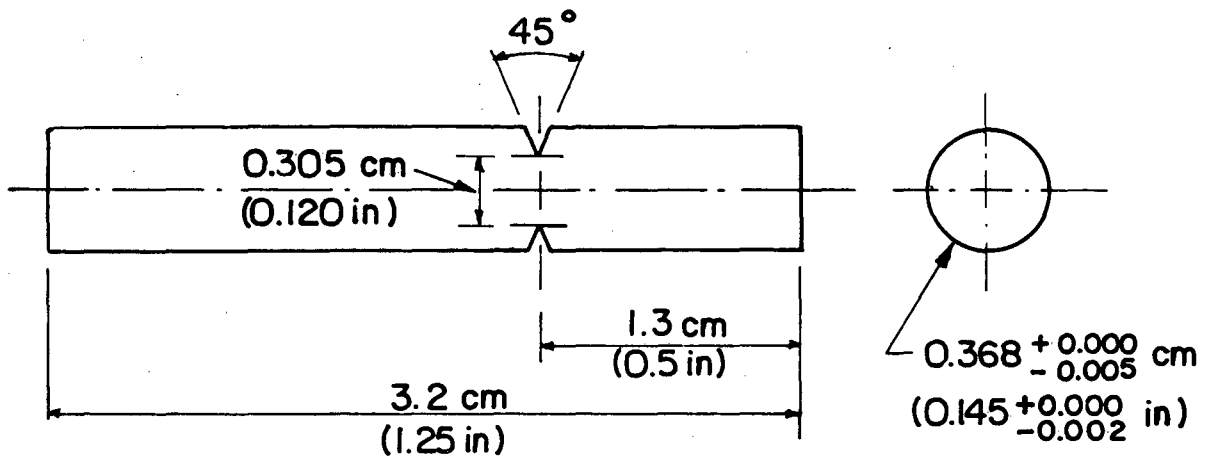


Figure 3

XBL 812-5242

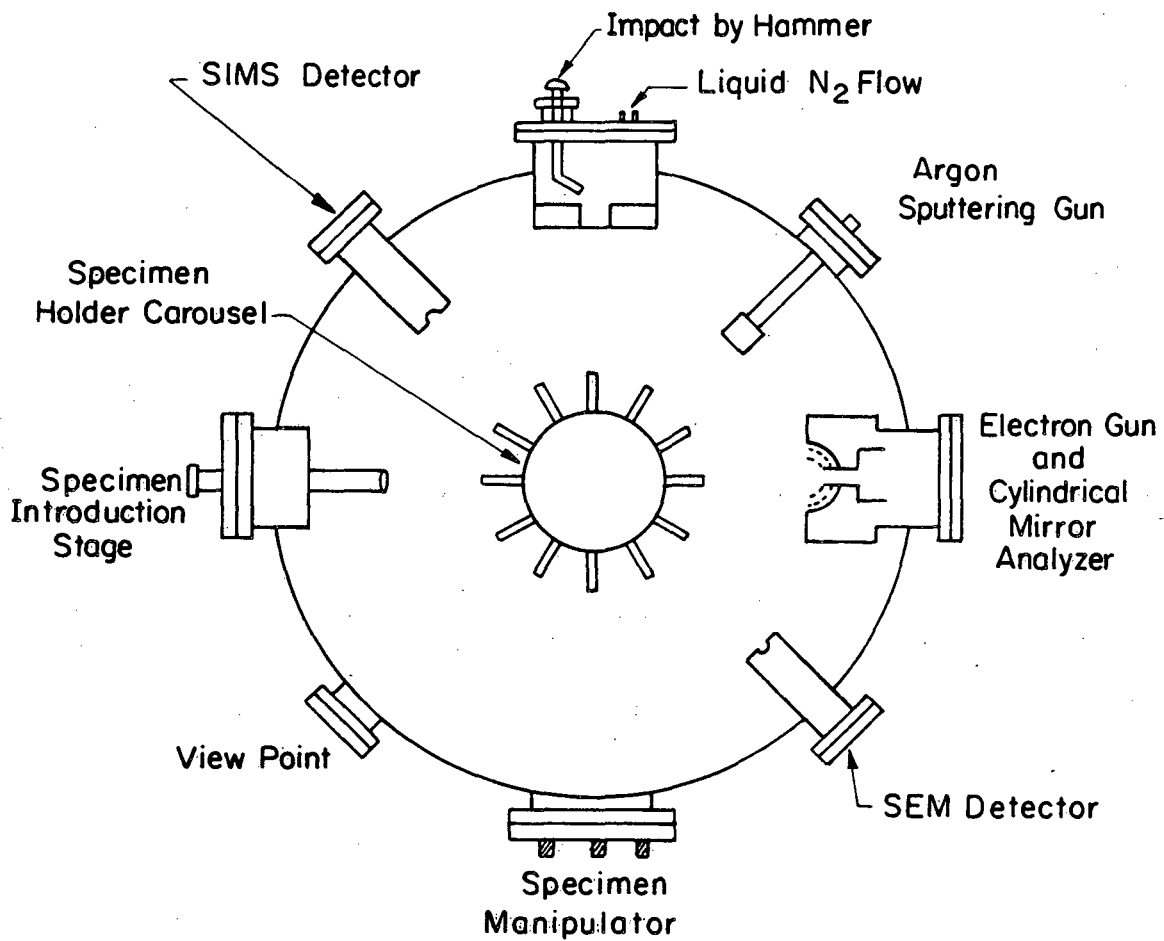


Figure 4

XBL 812-5241

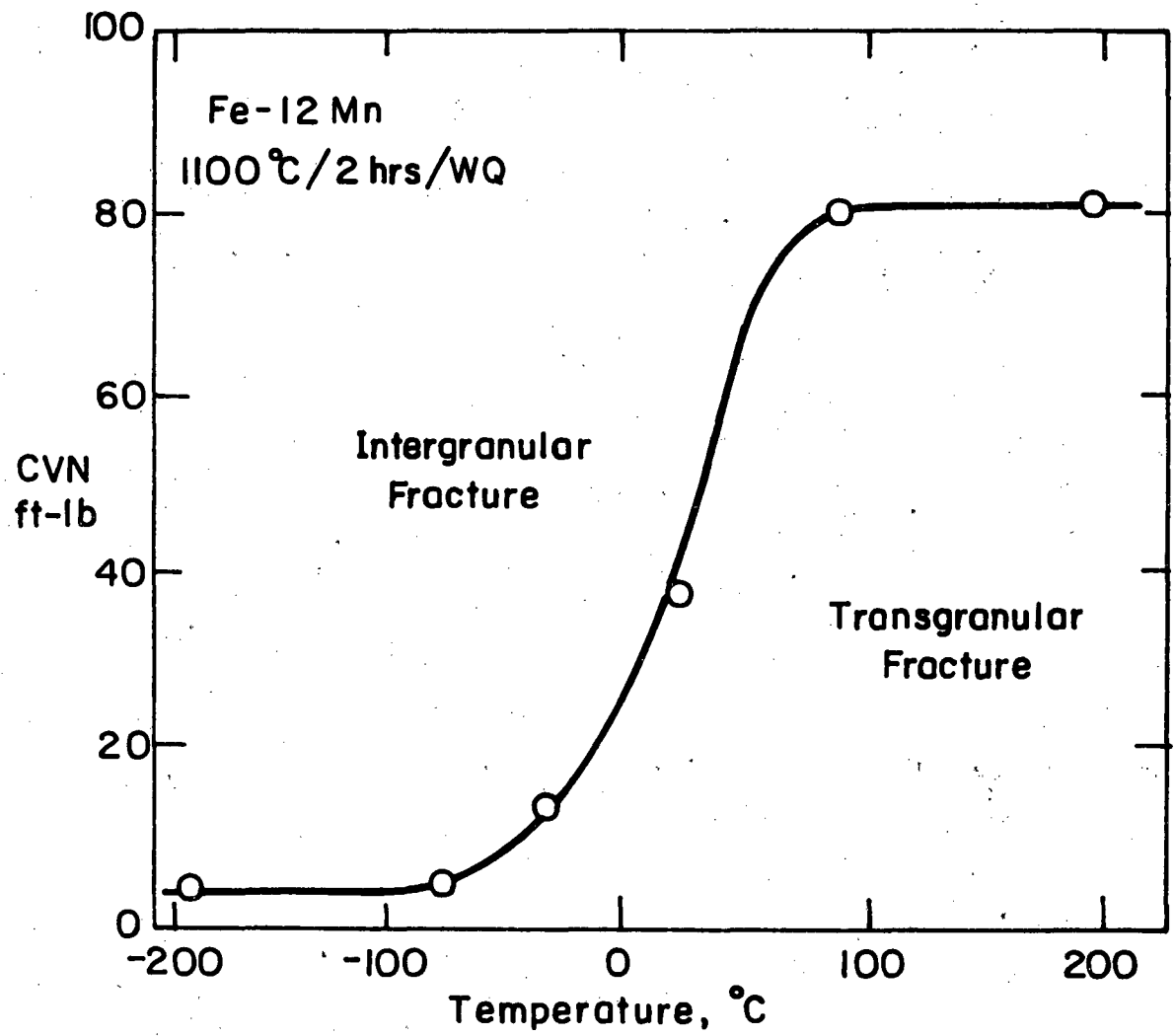


Figure 5

XBL 8110-6793

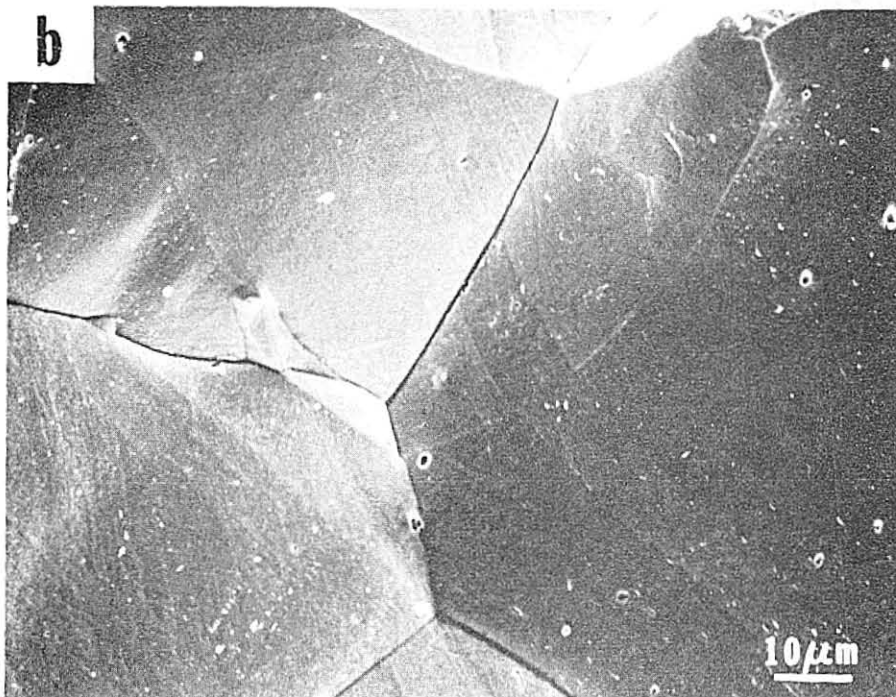
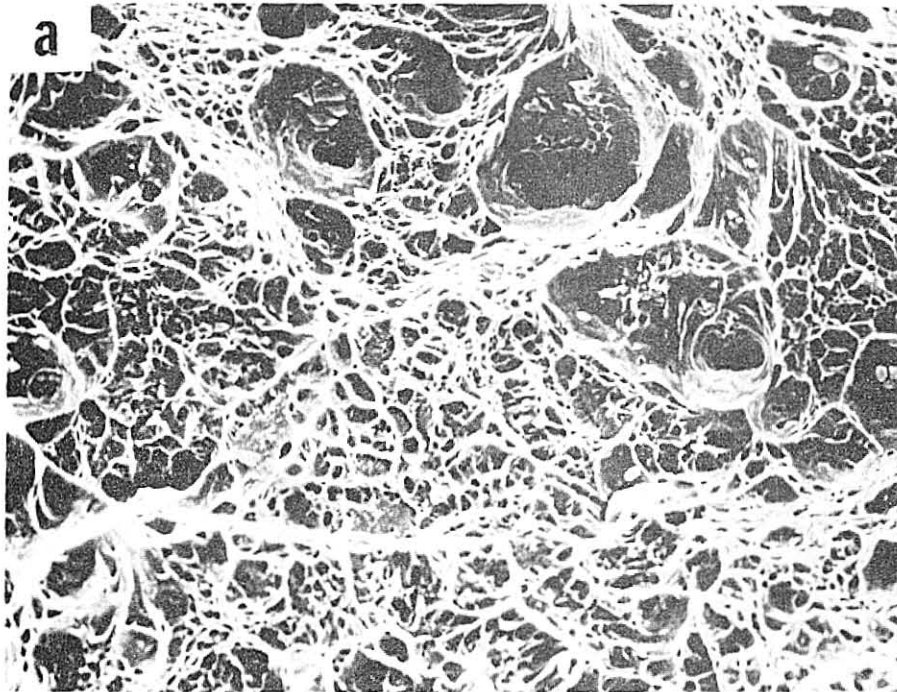


Figure 6

XBB 810-10132

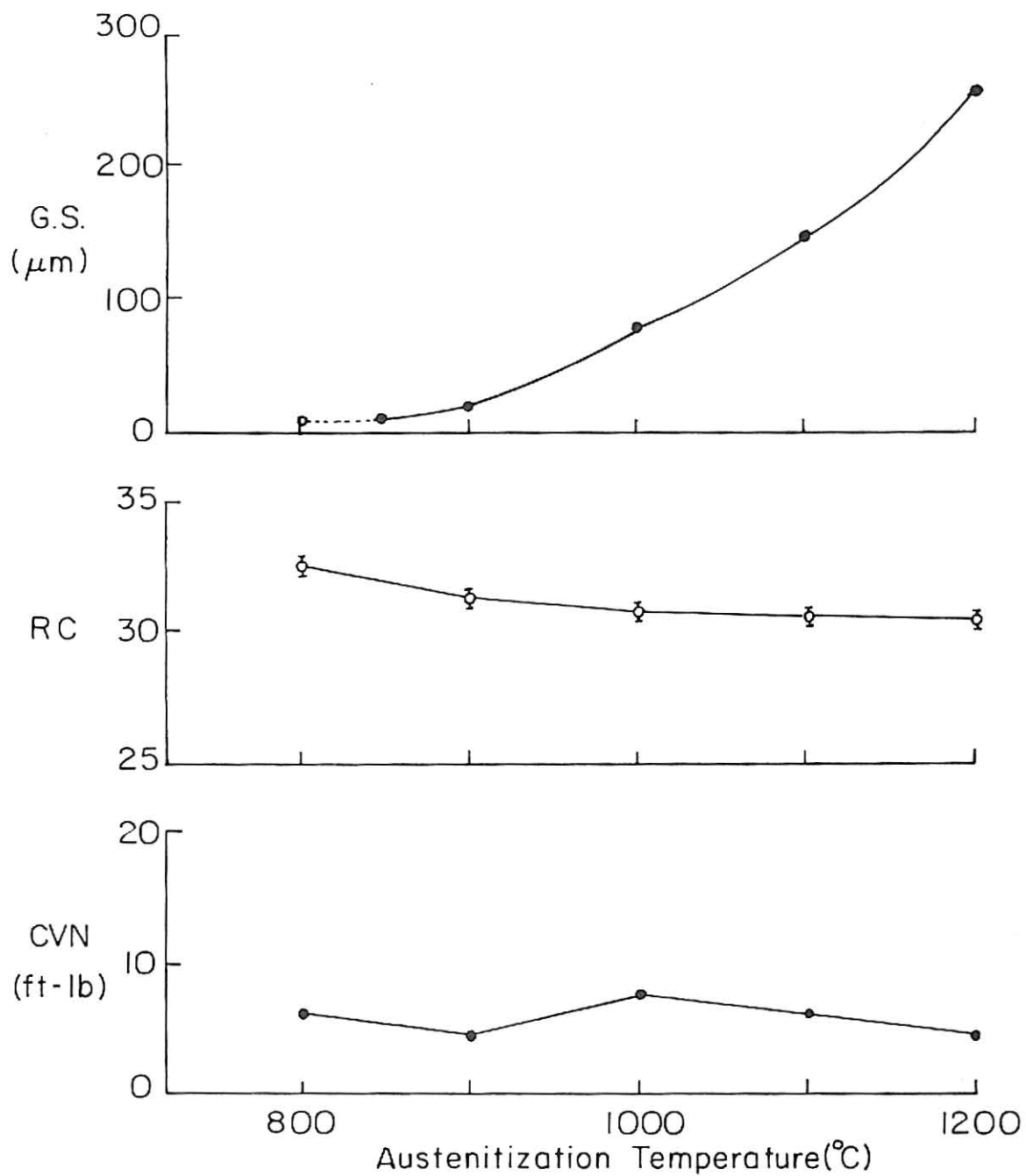


Figure 7

XBL 8010-624I

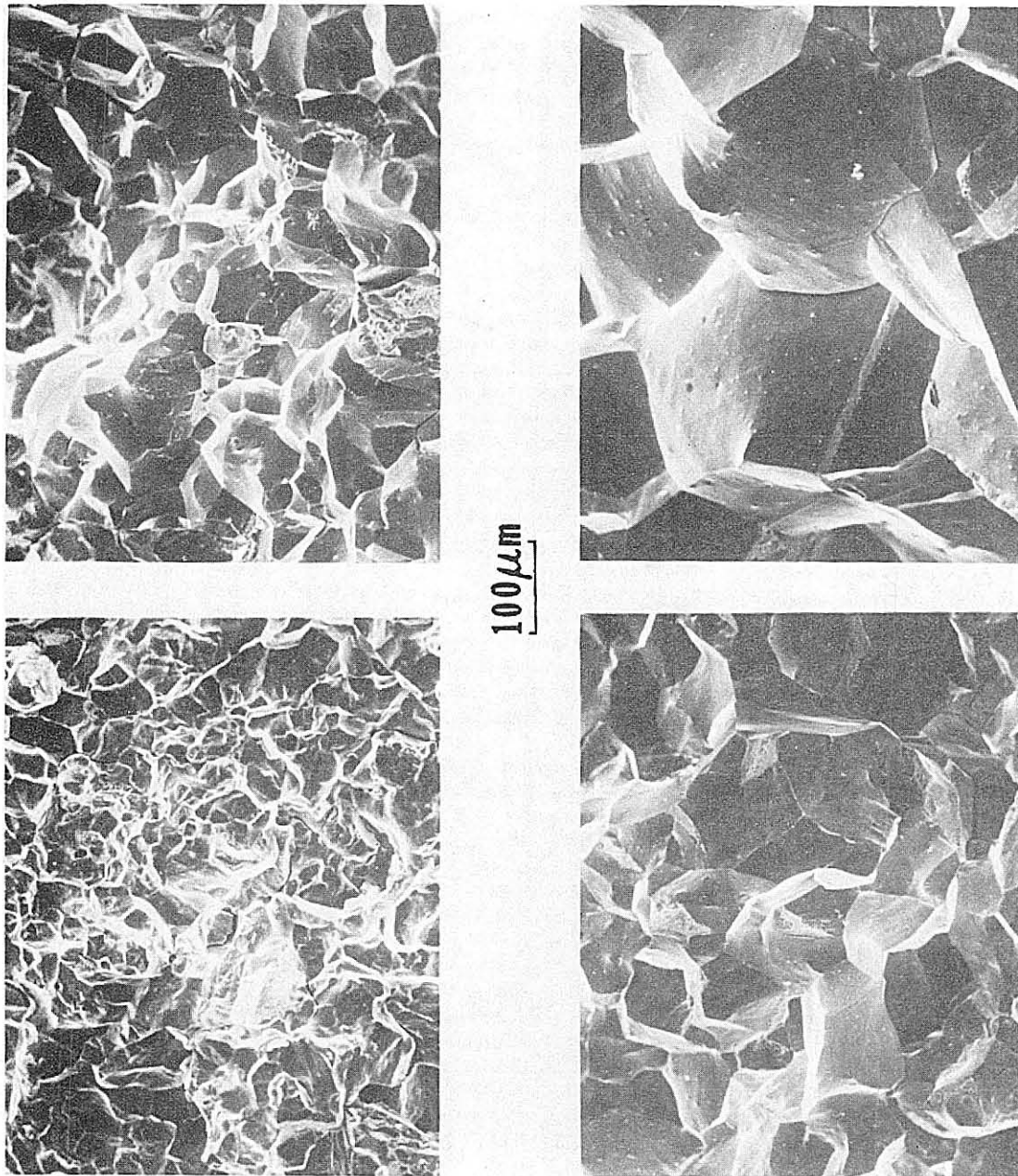


Figure 8

XBB 800-12306

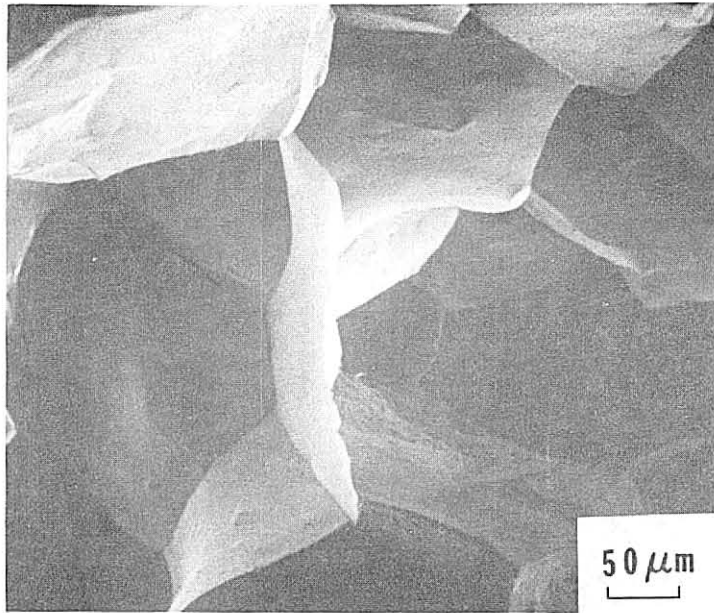
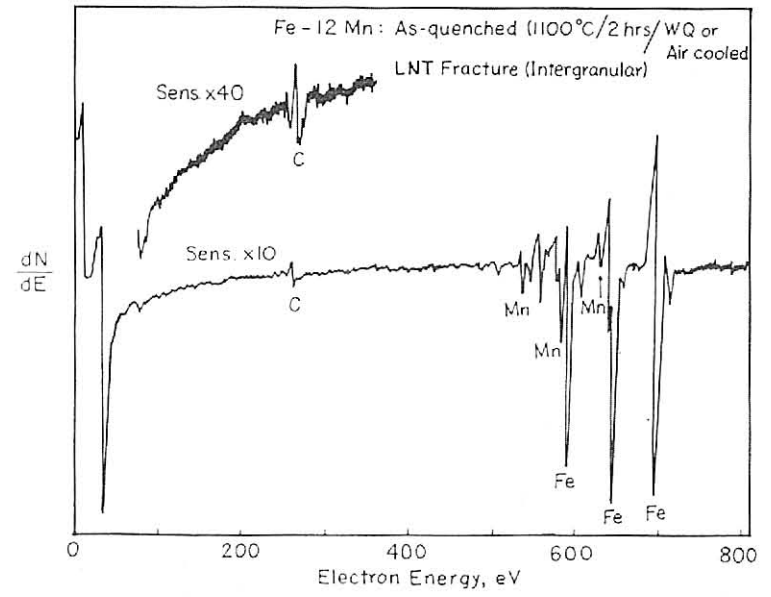


Figure 9



XBB 812-1600

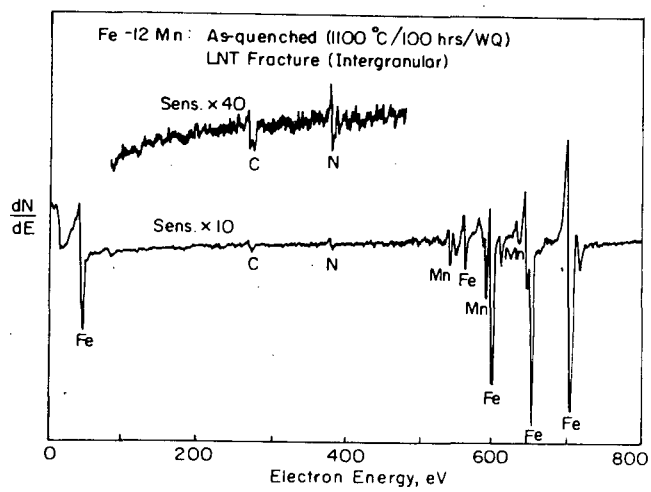
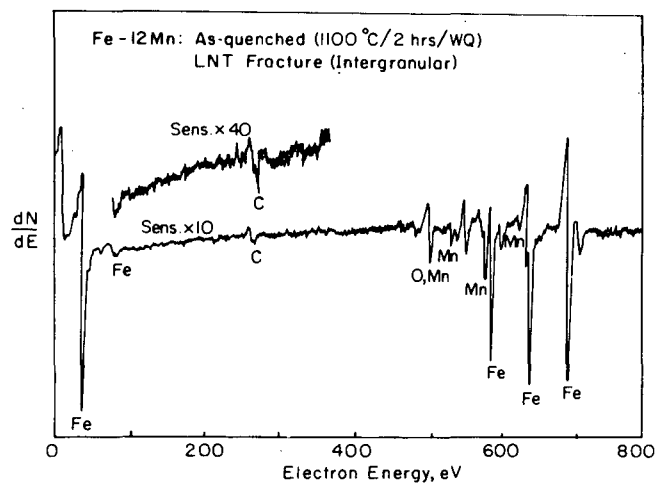


Figure 10

XBL 8011-12713

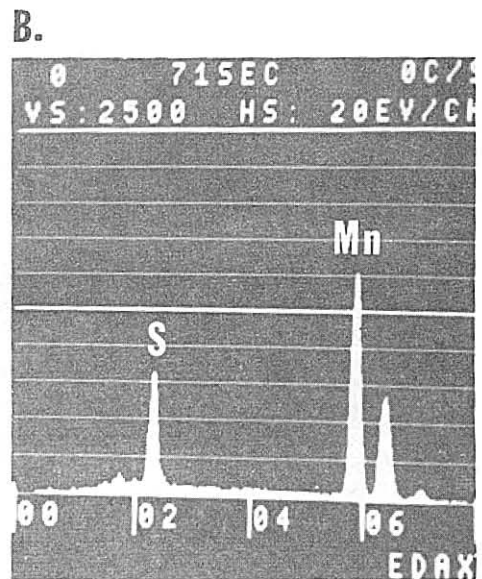
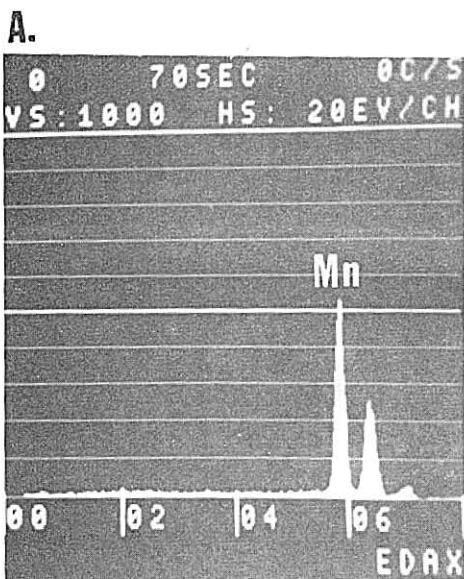
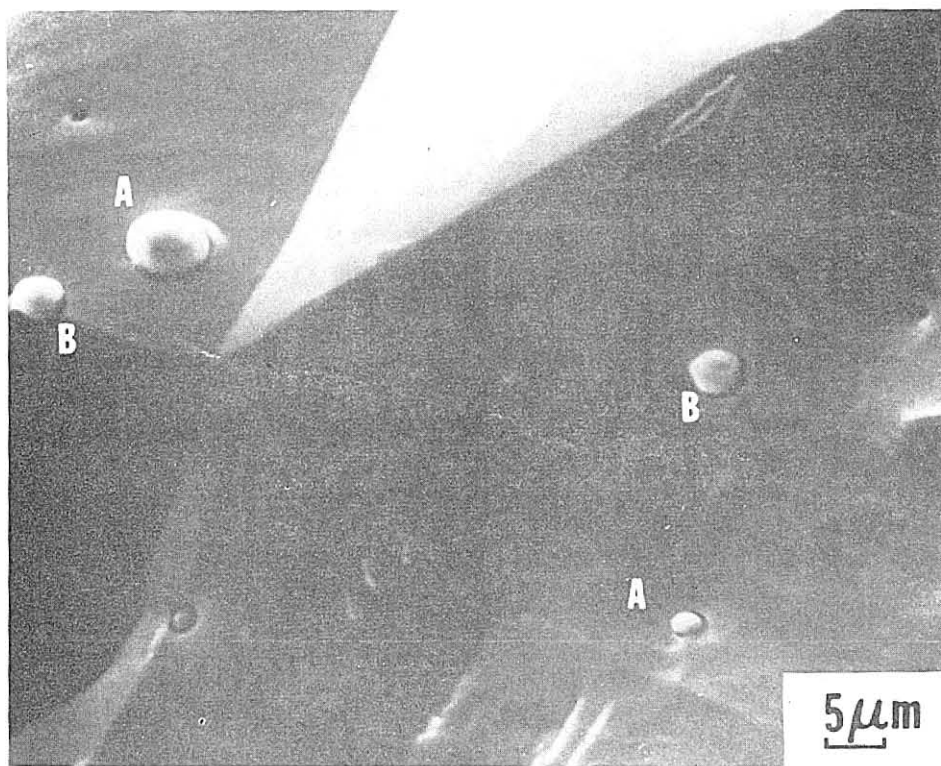


Figure 11

XBB 800-1307A

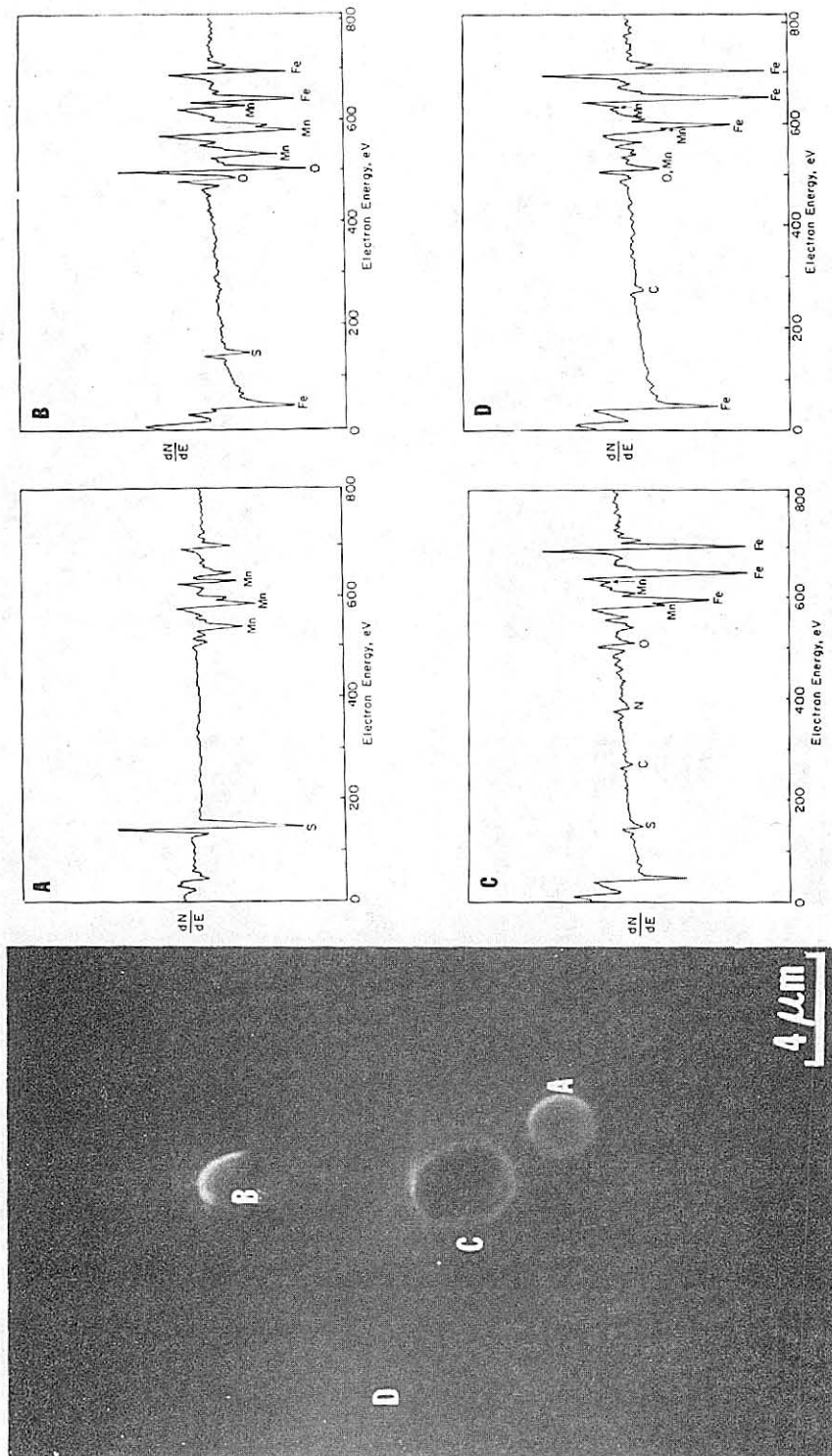


Figure 12

XBB 800-13508A

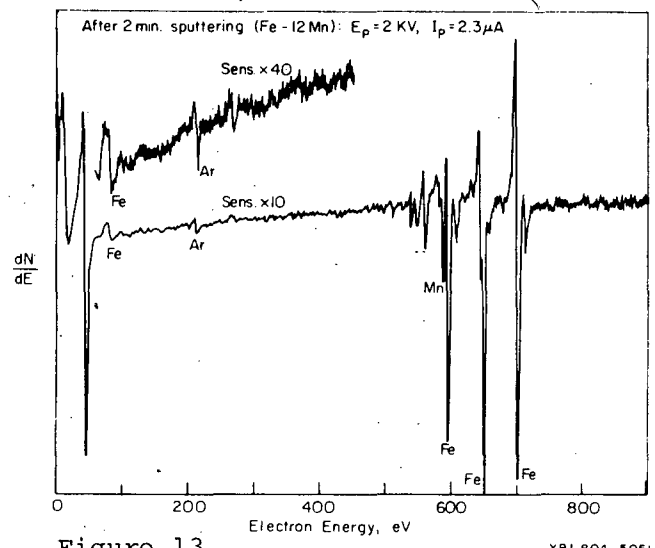
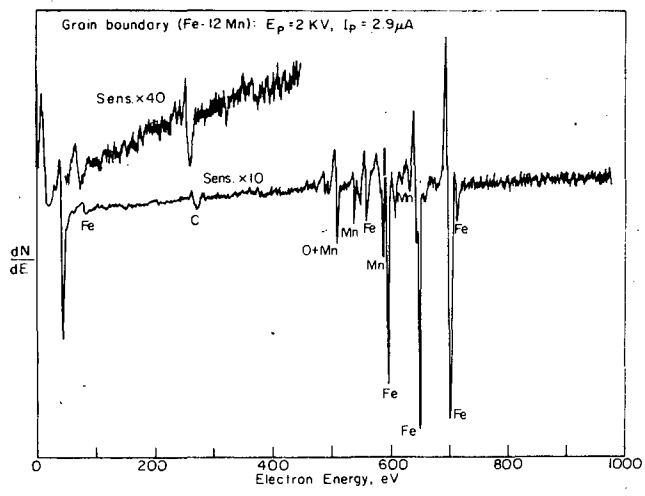


Figure 13

x8L804-5051A

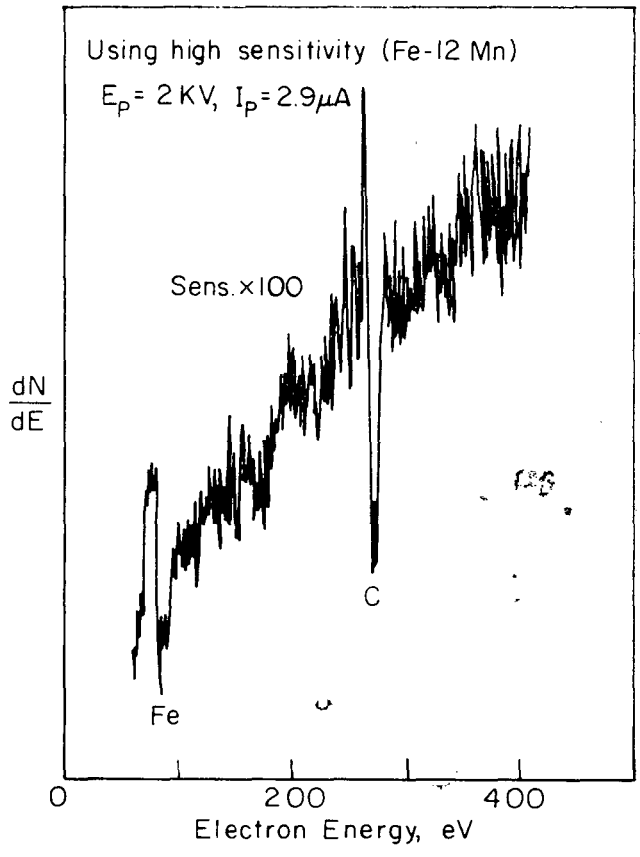
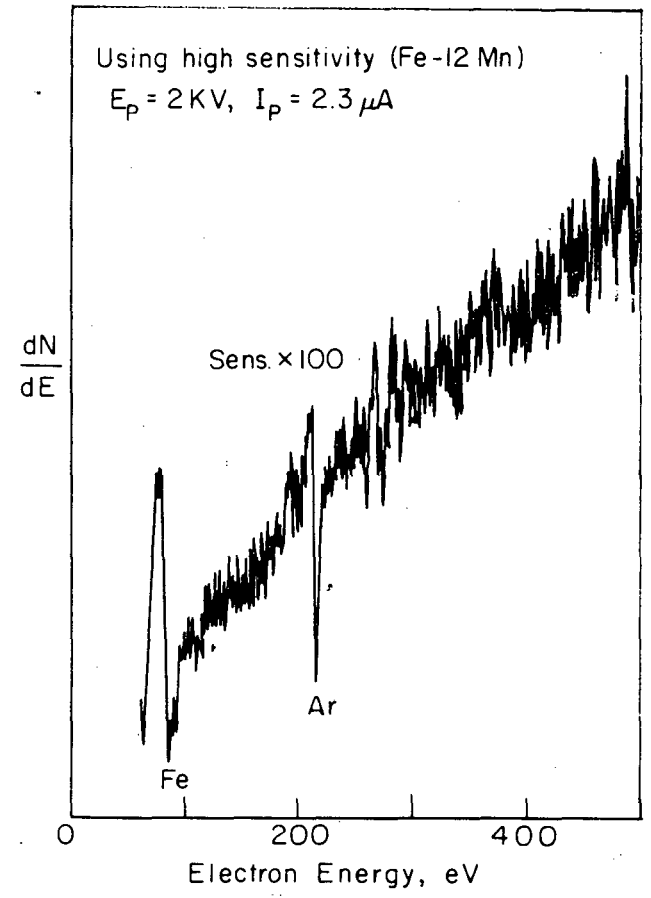


Figure 14



XBL 804-5057A

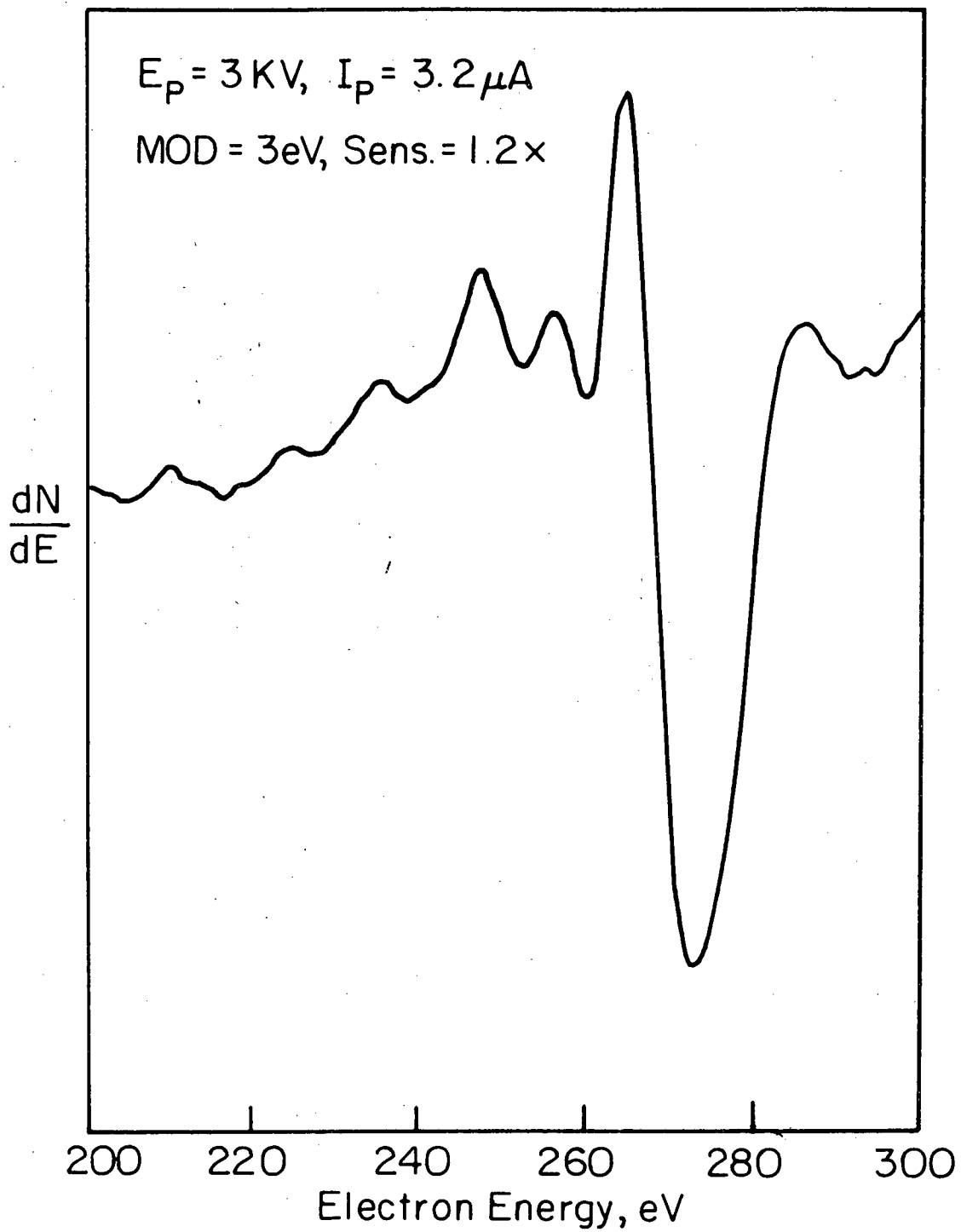


Figure 15

XBL804-5058

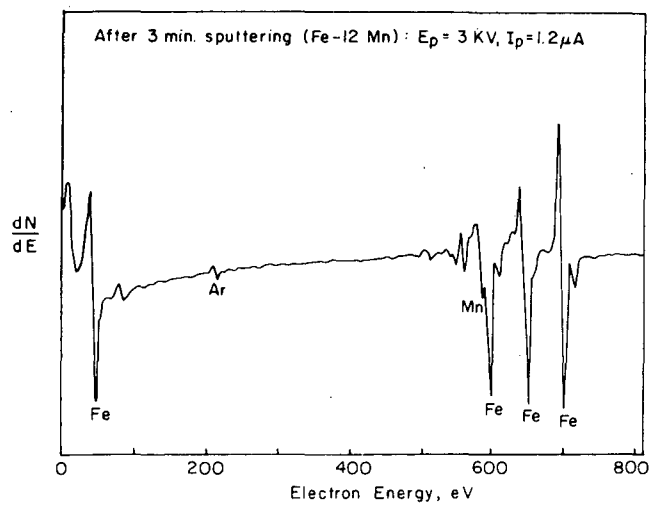
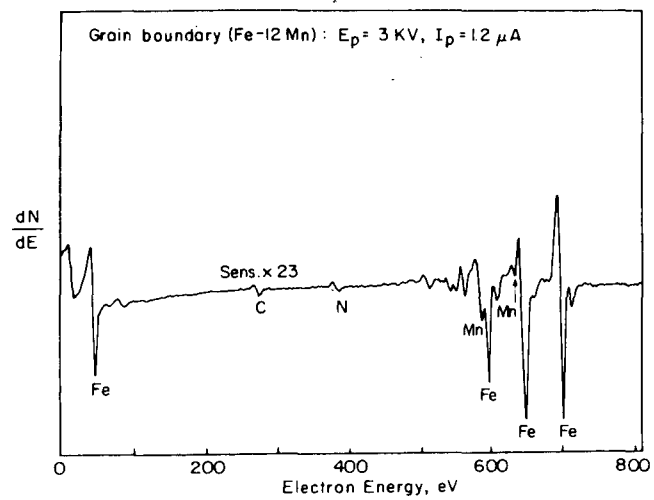


Figure 16

XBL 8011-12714

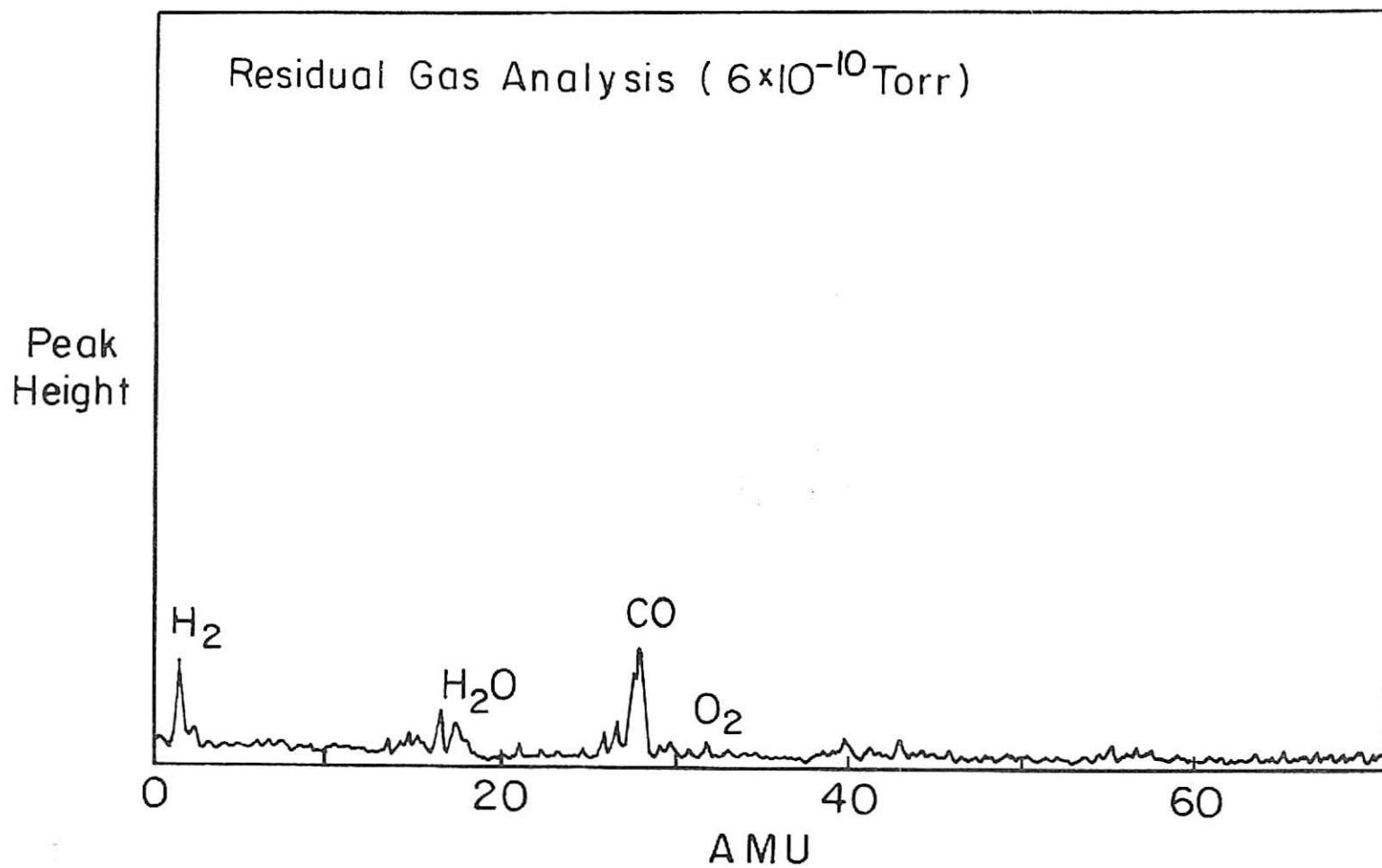
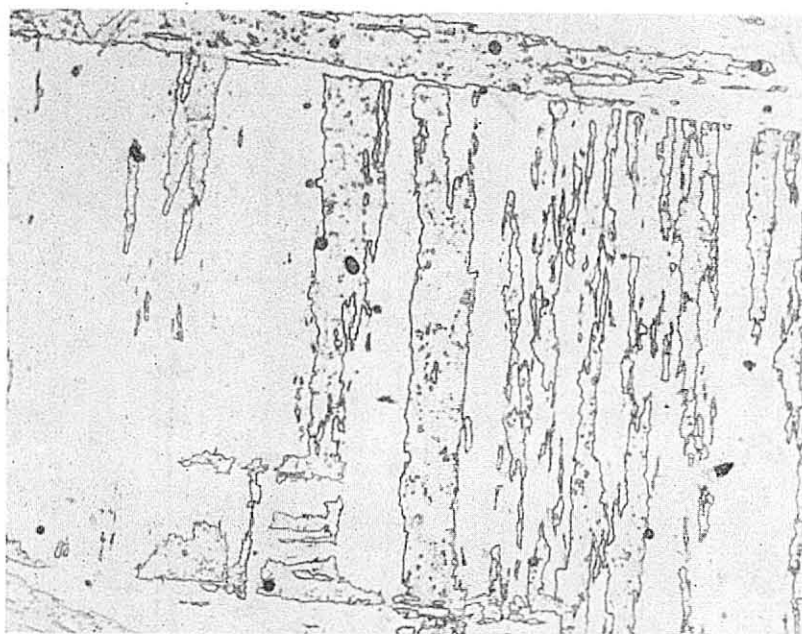


Figure 17

XBL 8010-6 24 2A



30 μ m

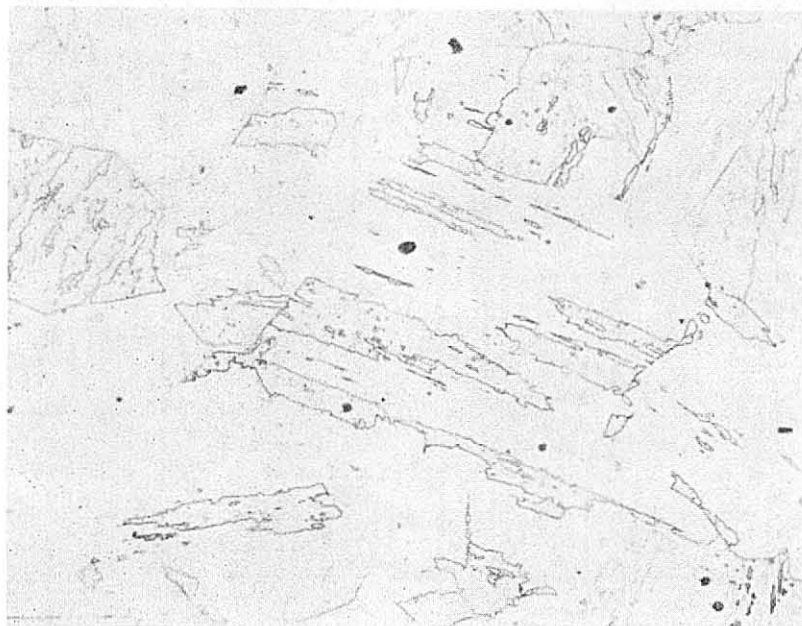


Figure 18

XBB 800-12308



Figure 19

XBB 810-11513

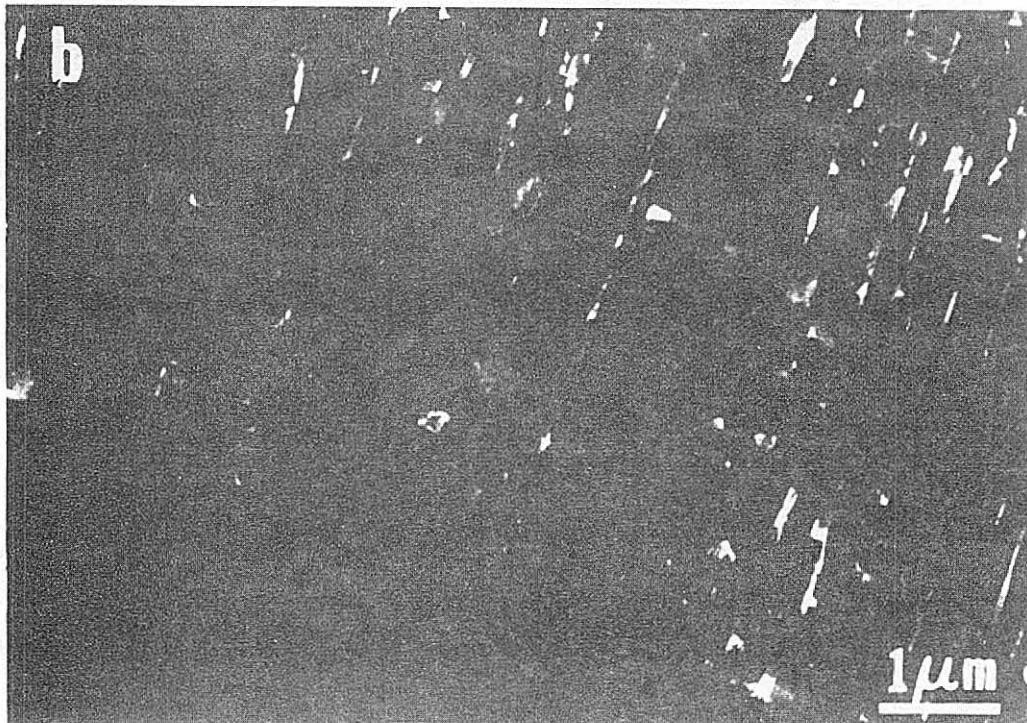
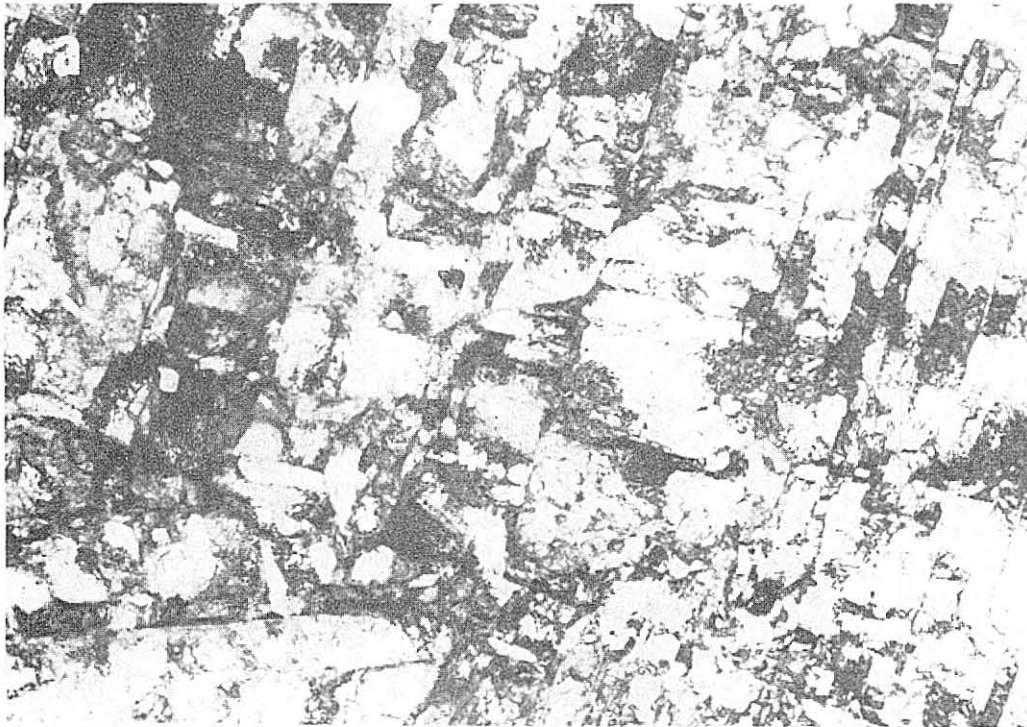


Figure 20

XBB 810-11419

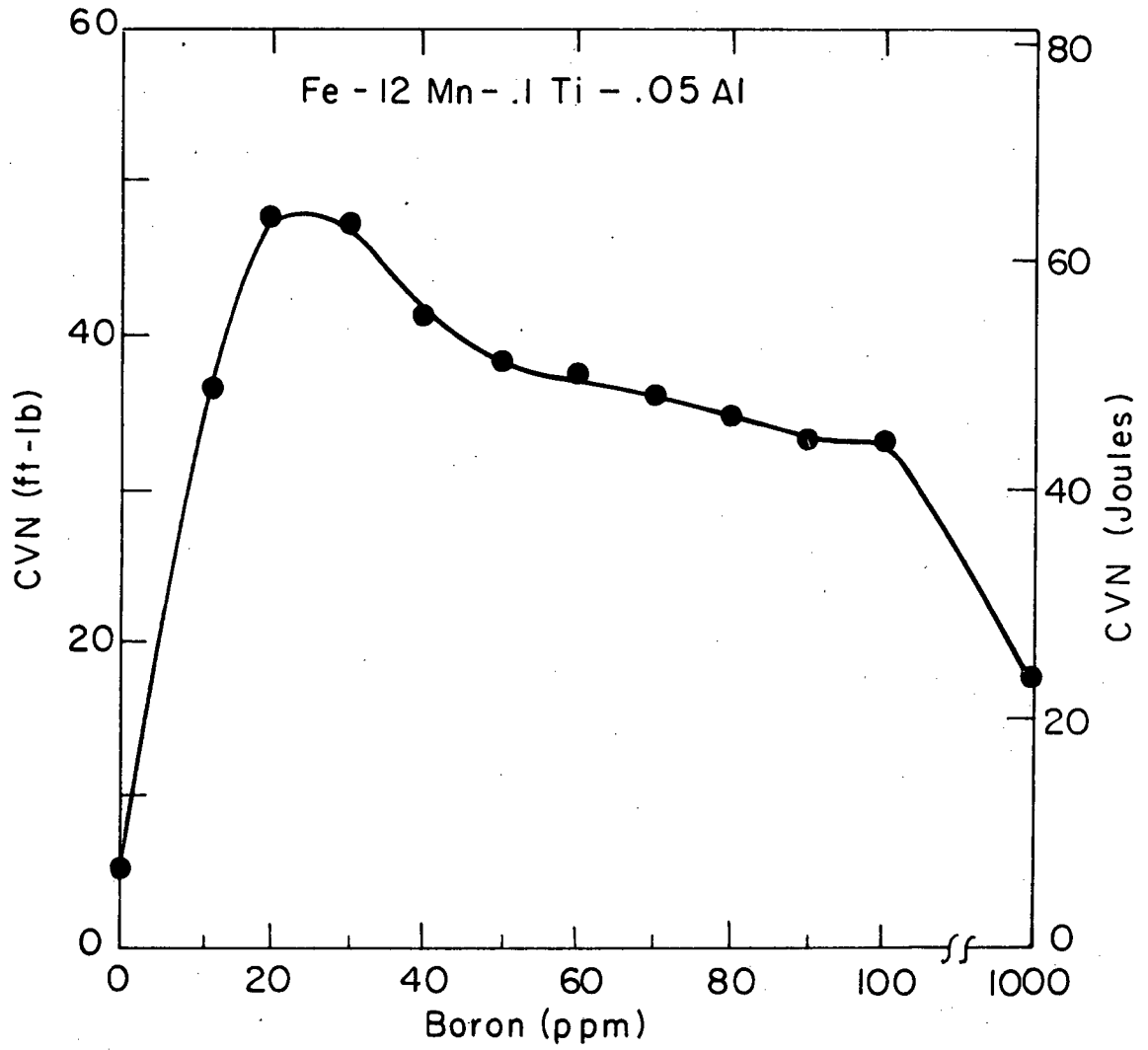


Figure 21

XBL812-5231

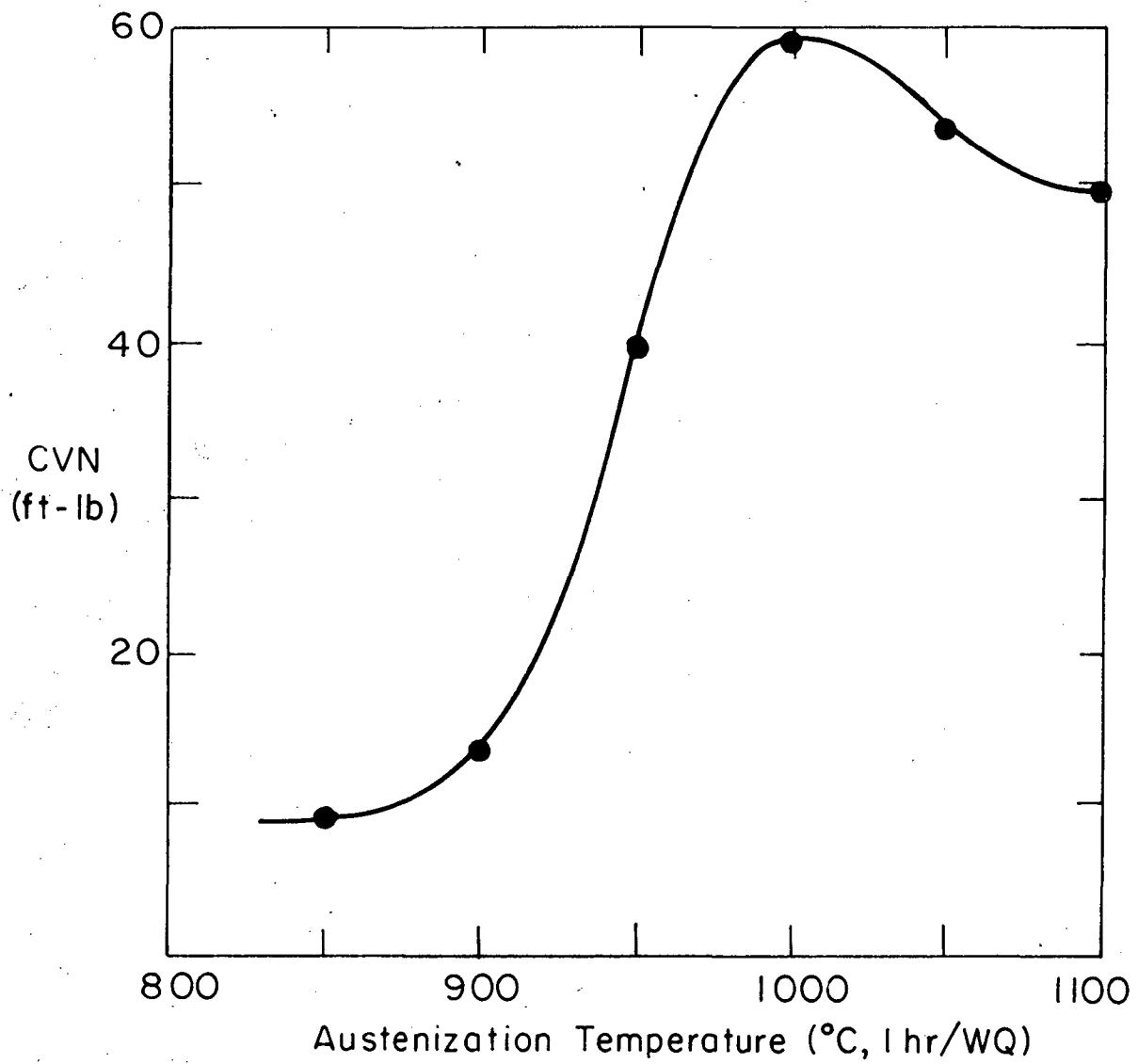


Figure 22

XBL 812-5226

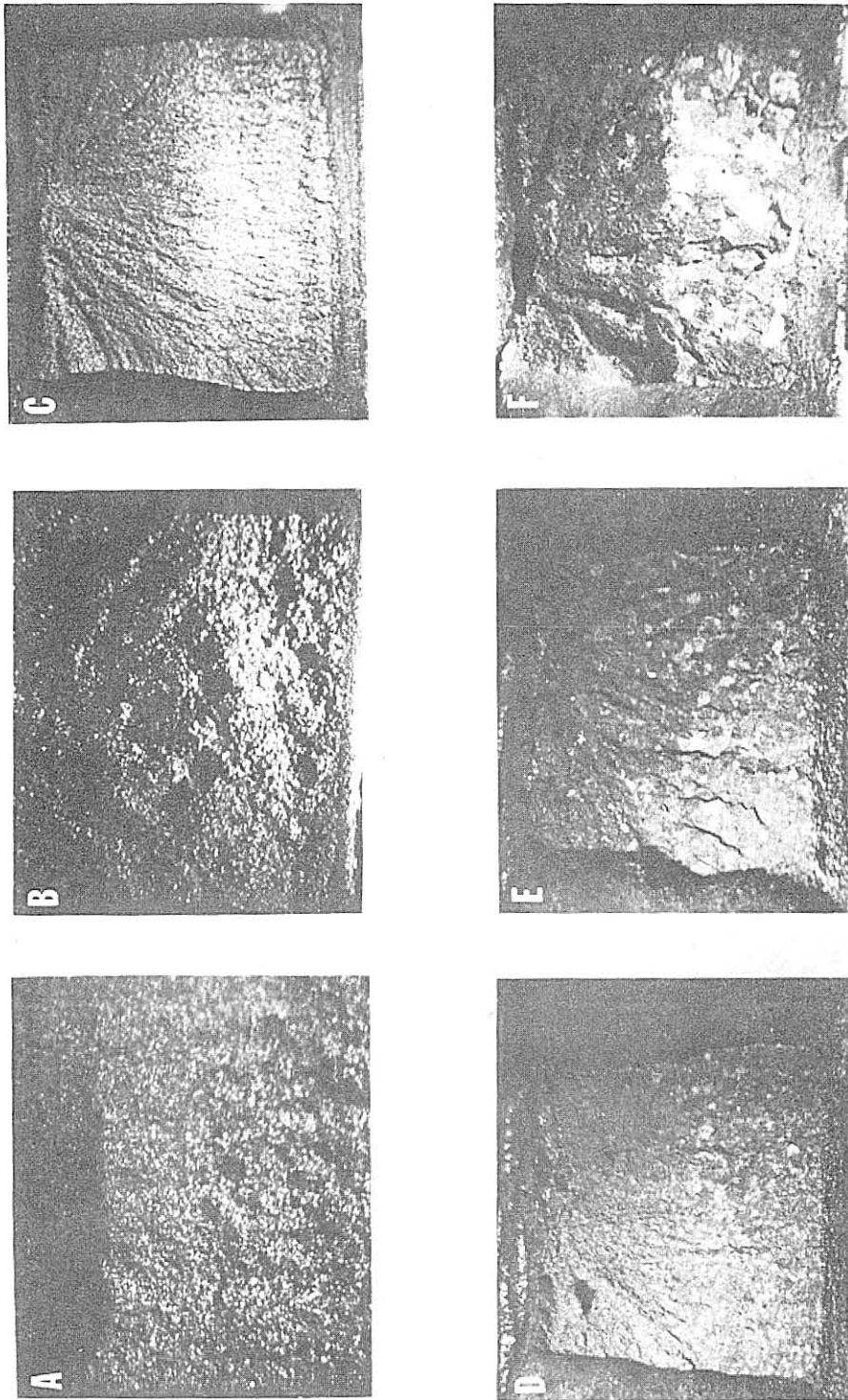


Figure 23

XBB 811-1099

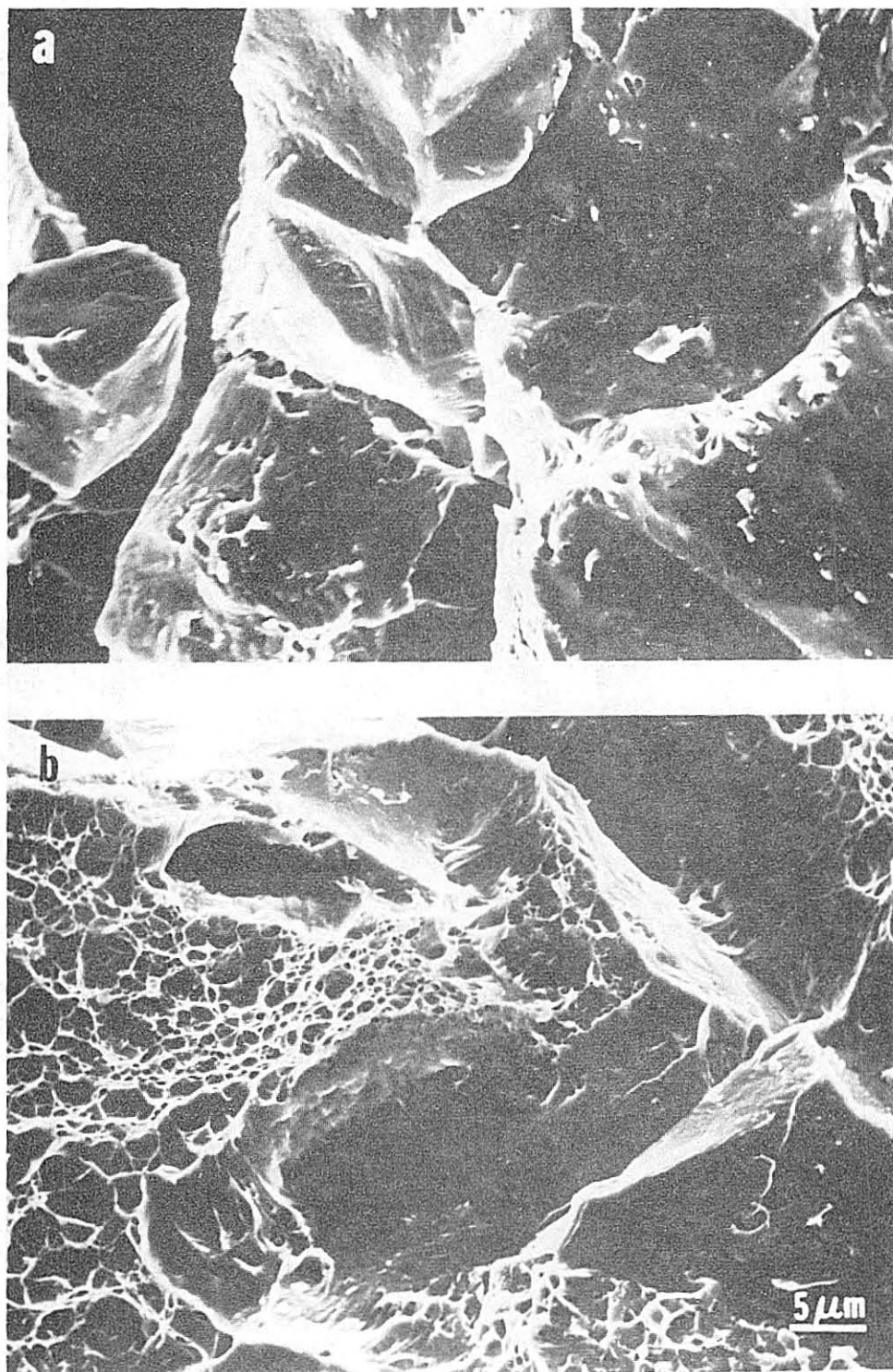


Figure 28

XBB 810-10133

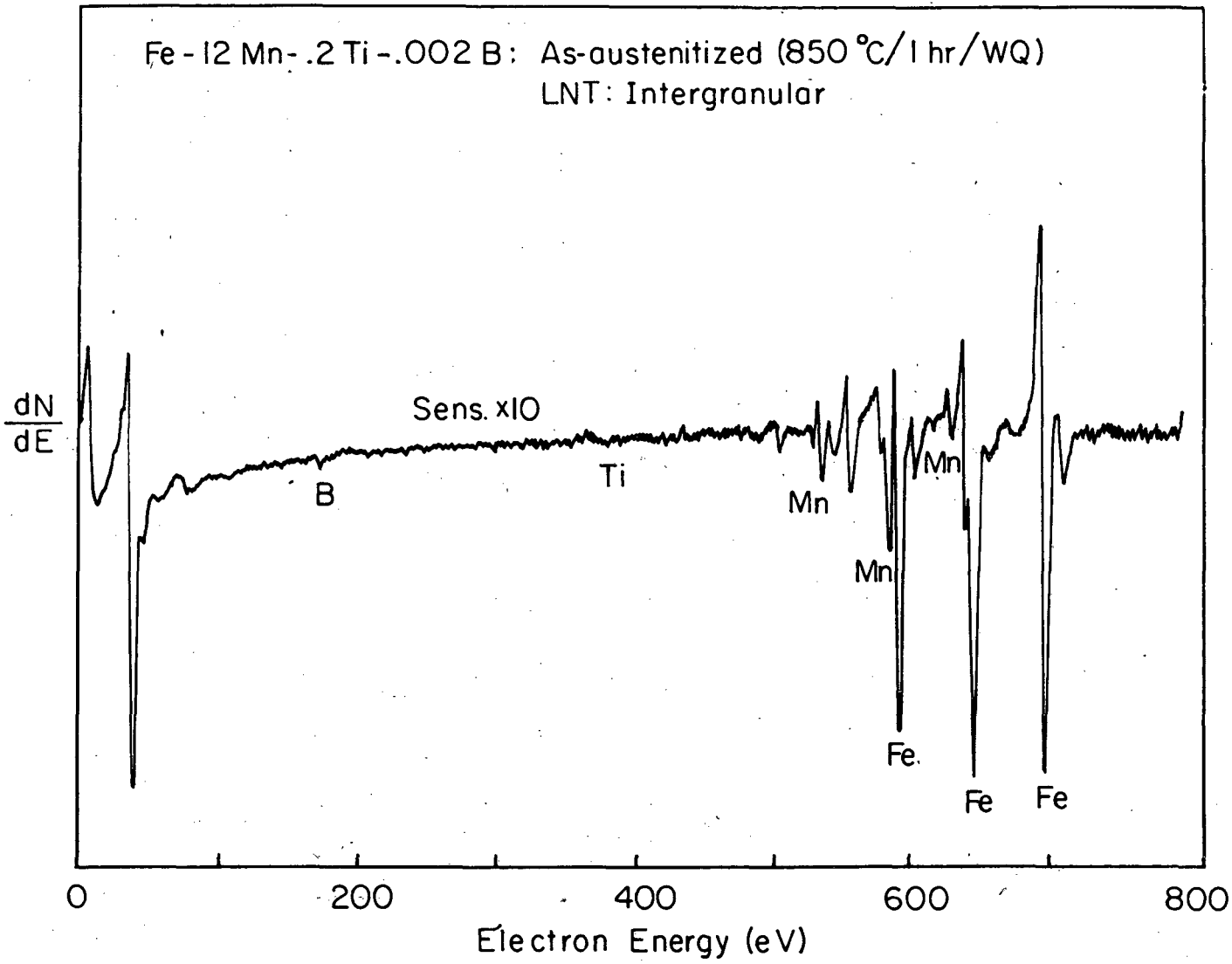


Figure 25

XBL 812 - 5236

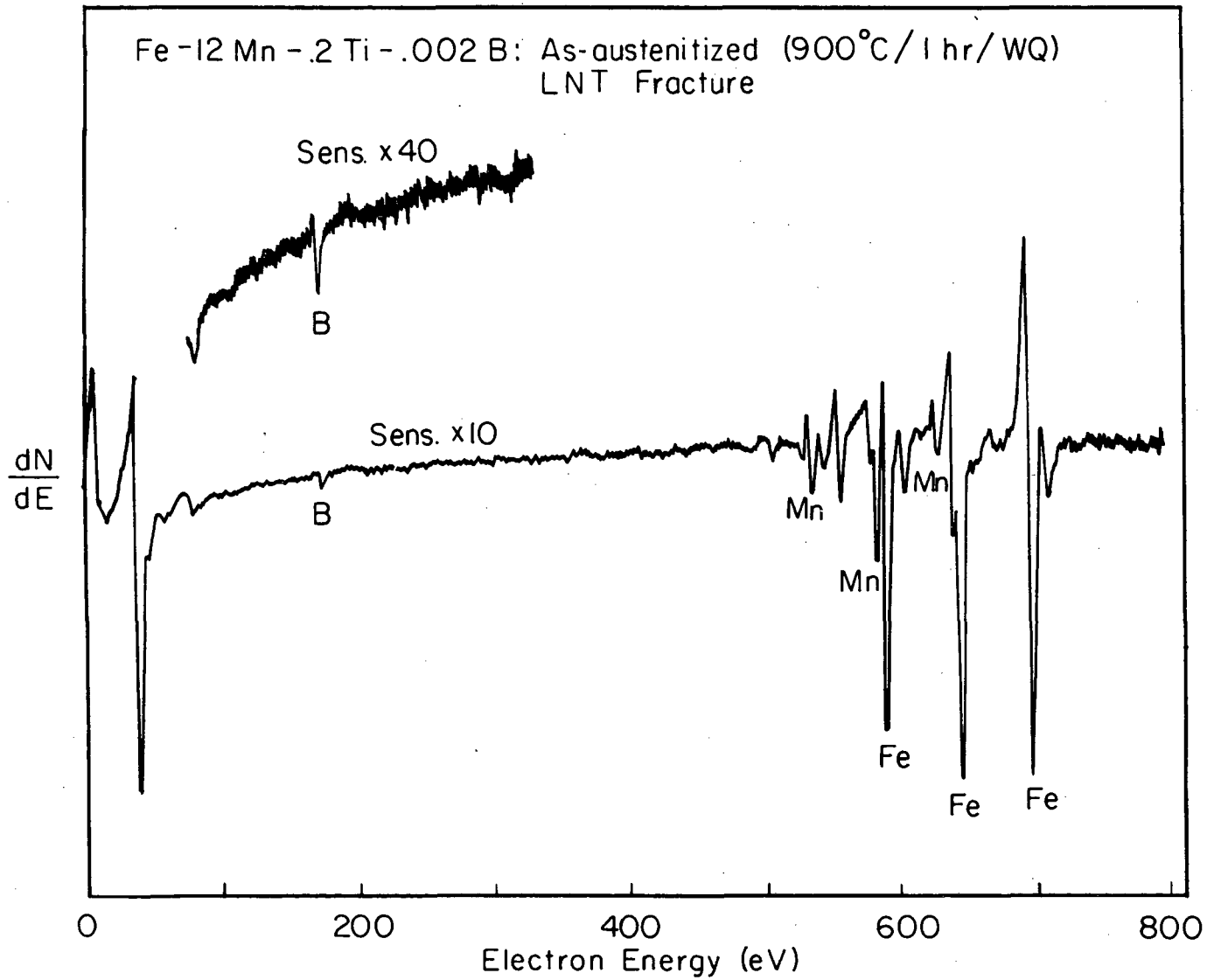


Figure 26

XBL 812-5235



Figure 27

XBB 810-11947

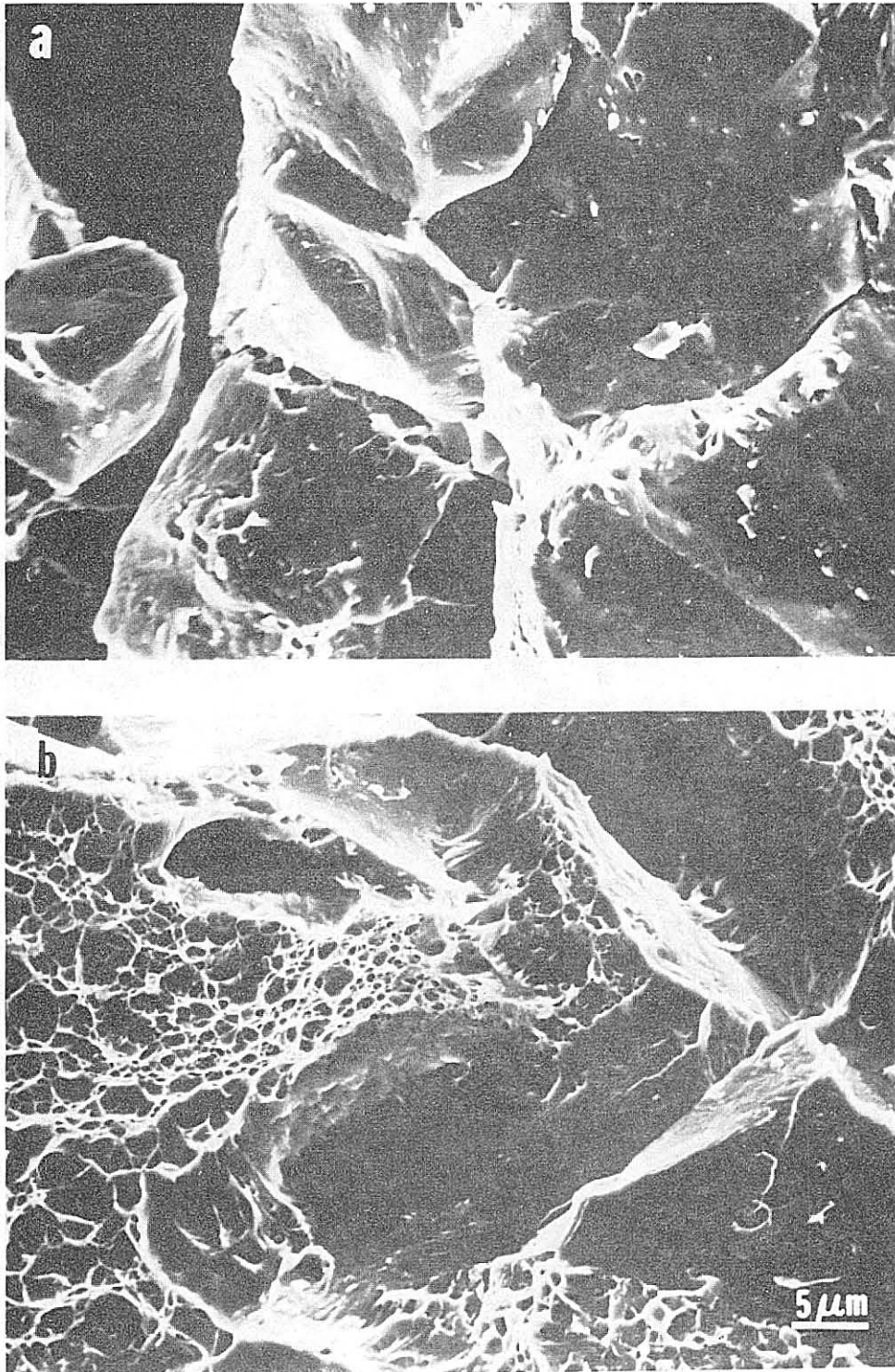


Figure 28

XBB 810-10133

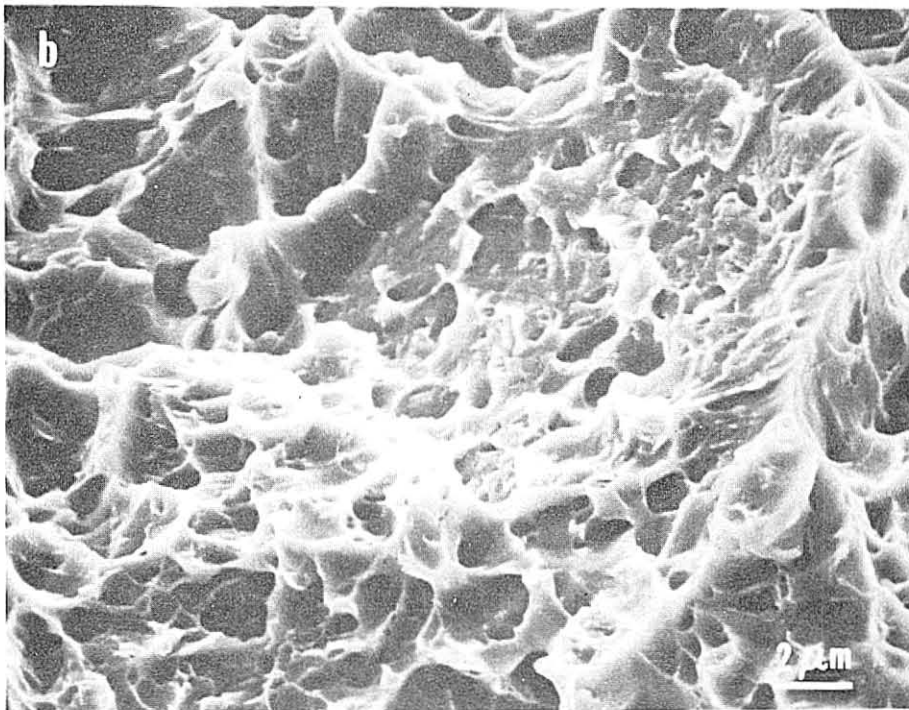
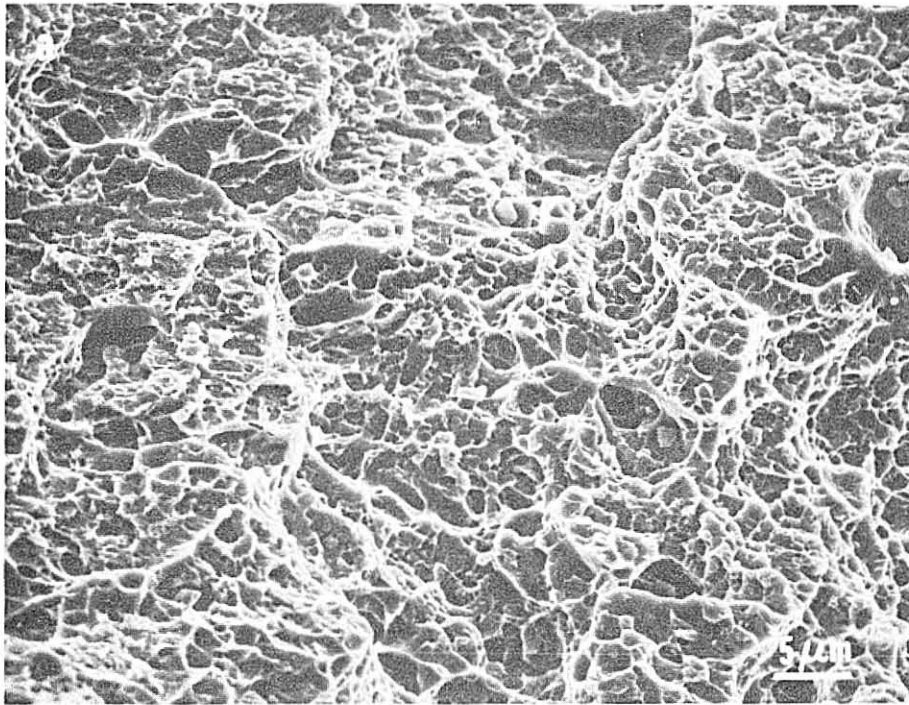


Figure 29

XBB 810-10131

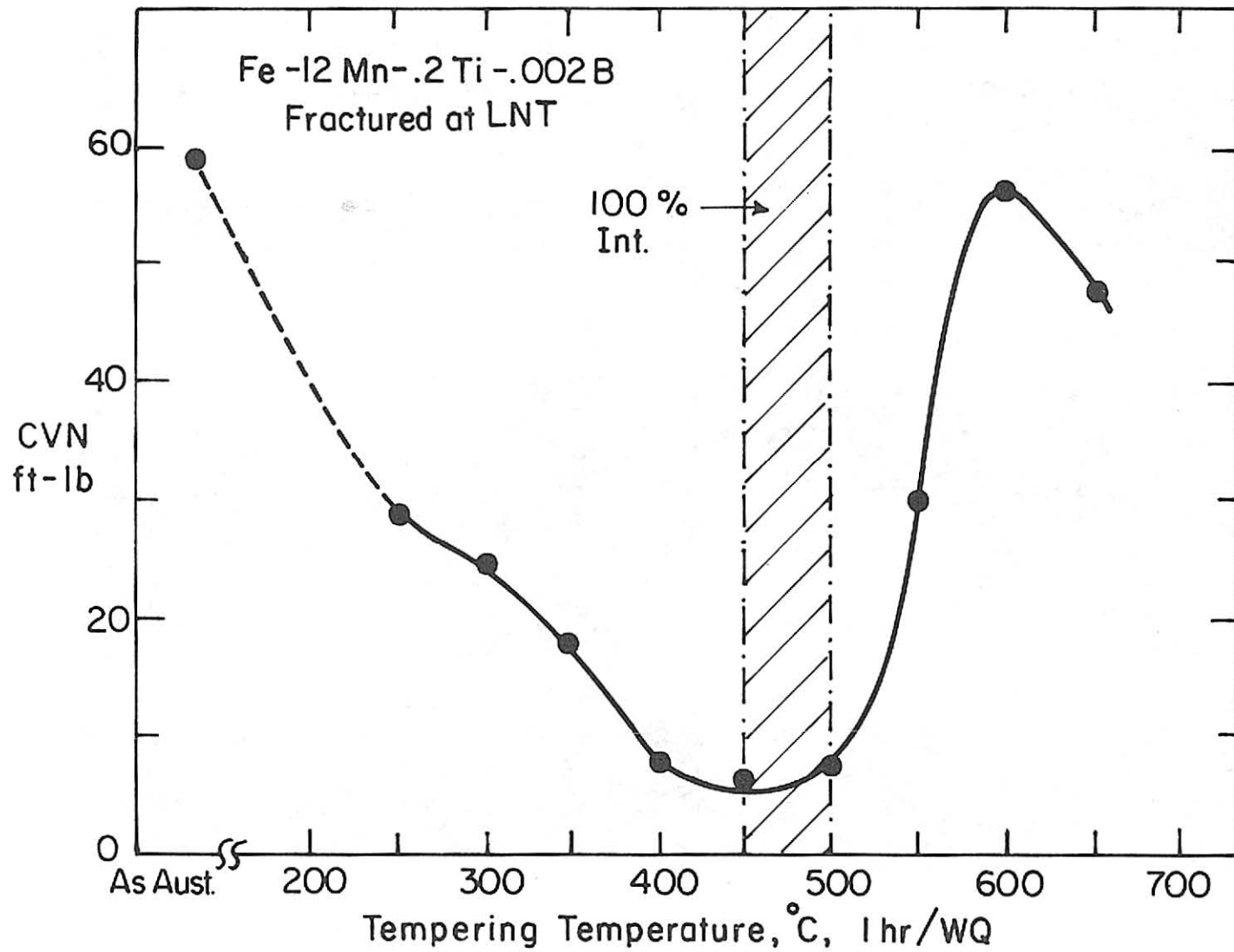


Figure 30

XBL8110-6788

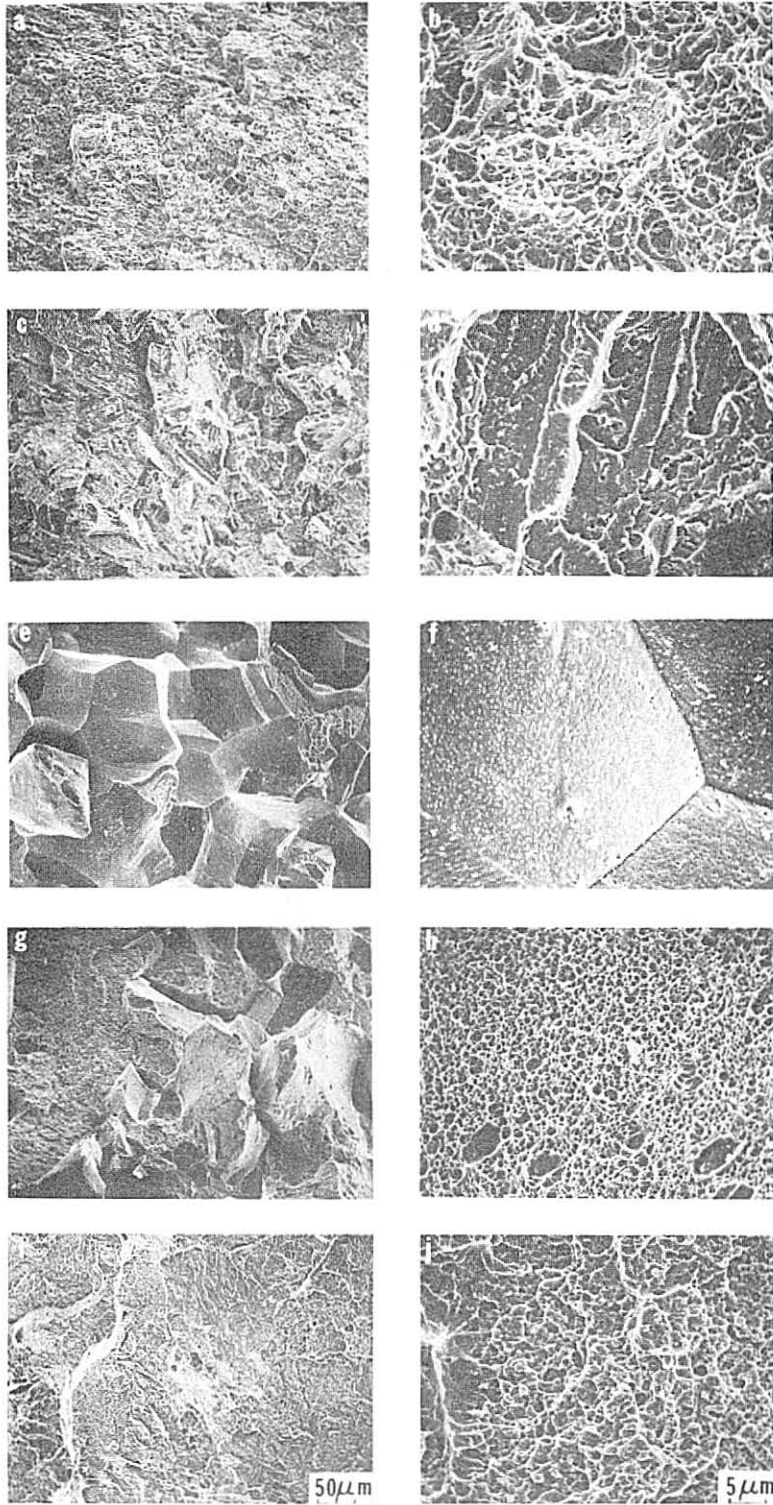


Figure 31

XBB 811-1100

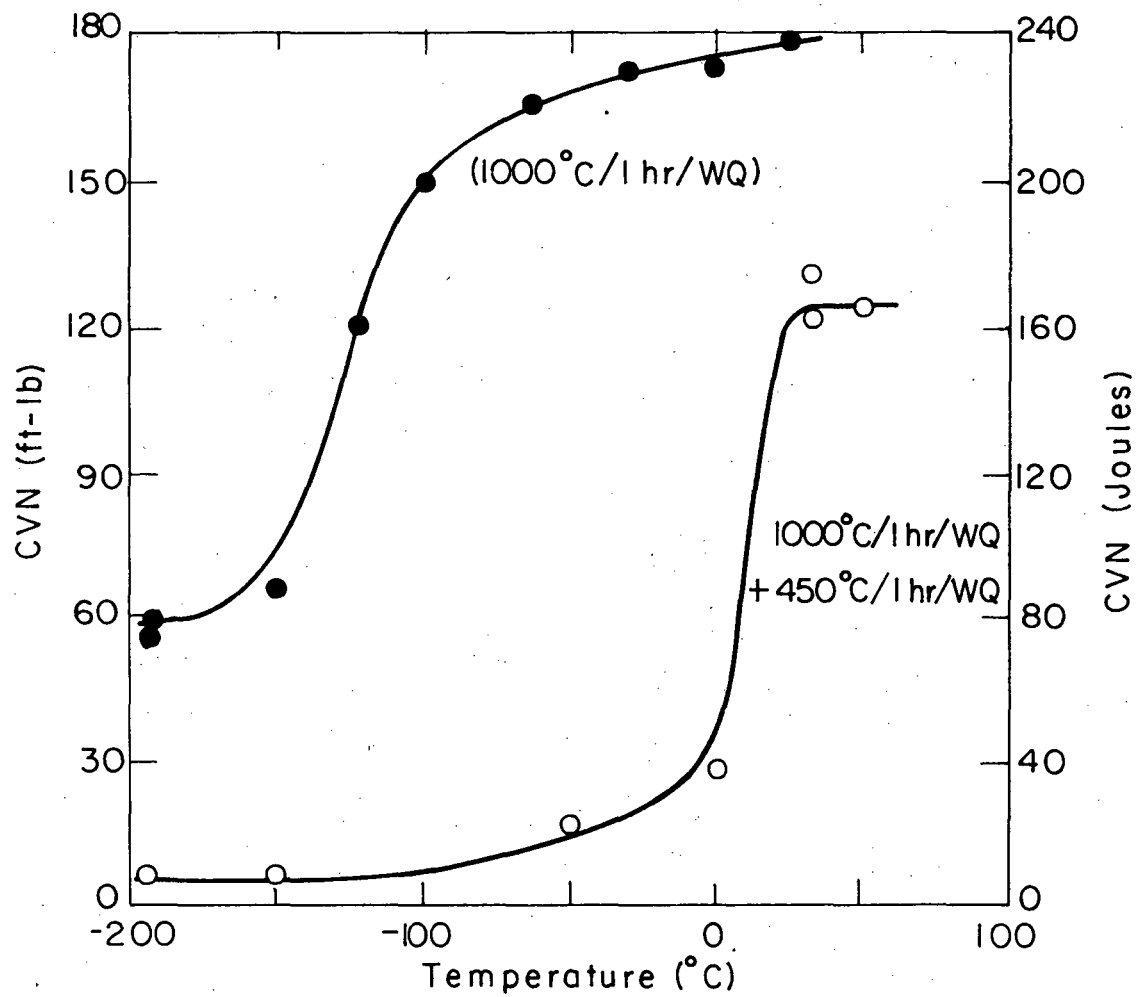


Figure 32

XBL 812-5224

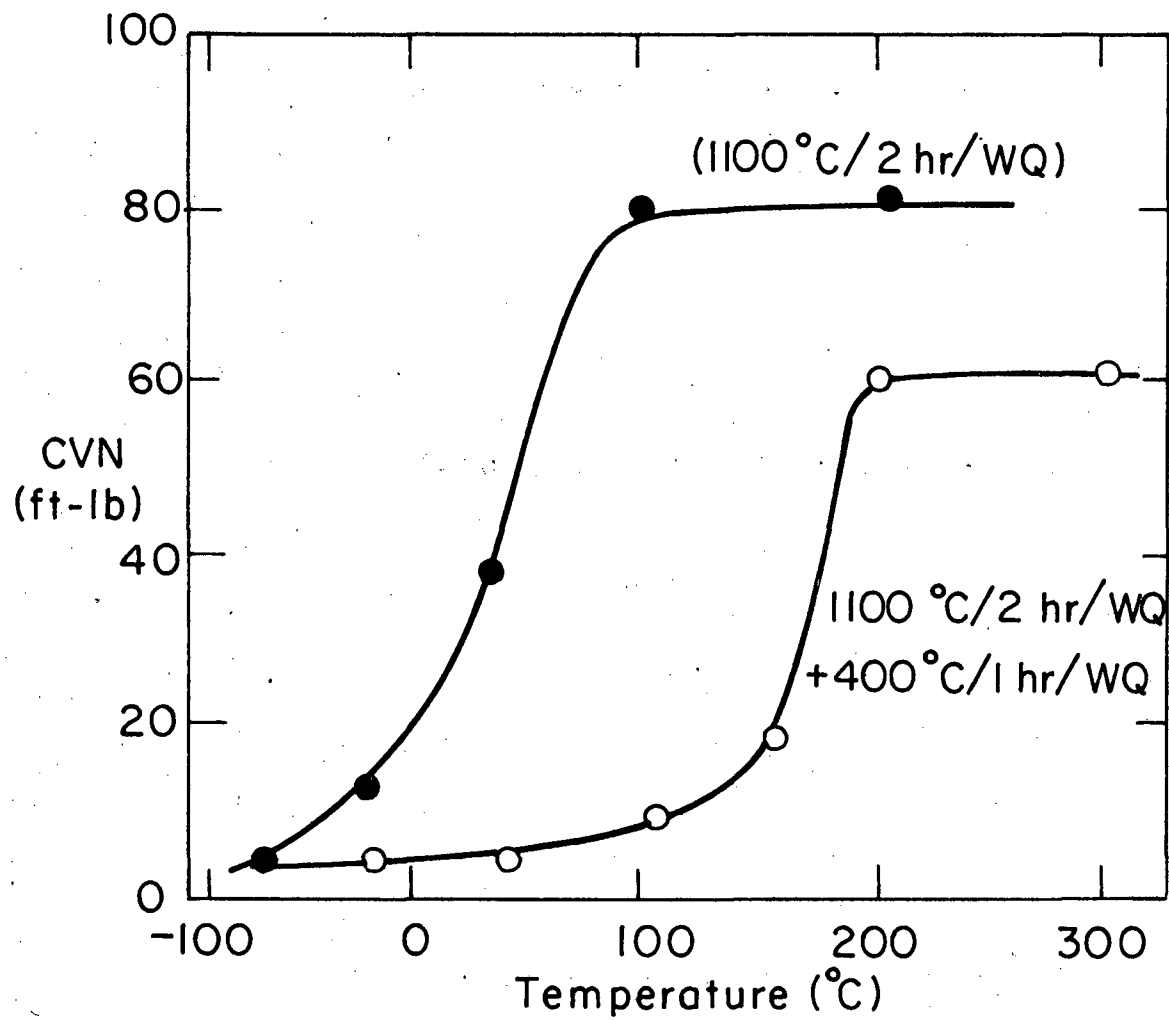


Figure 33

XBL 812-5227

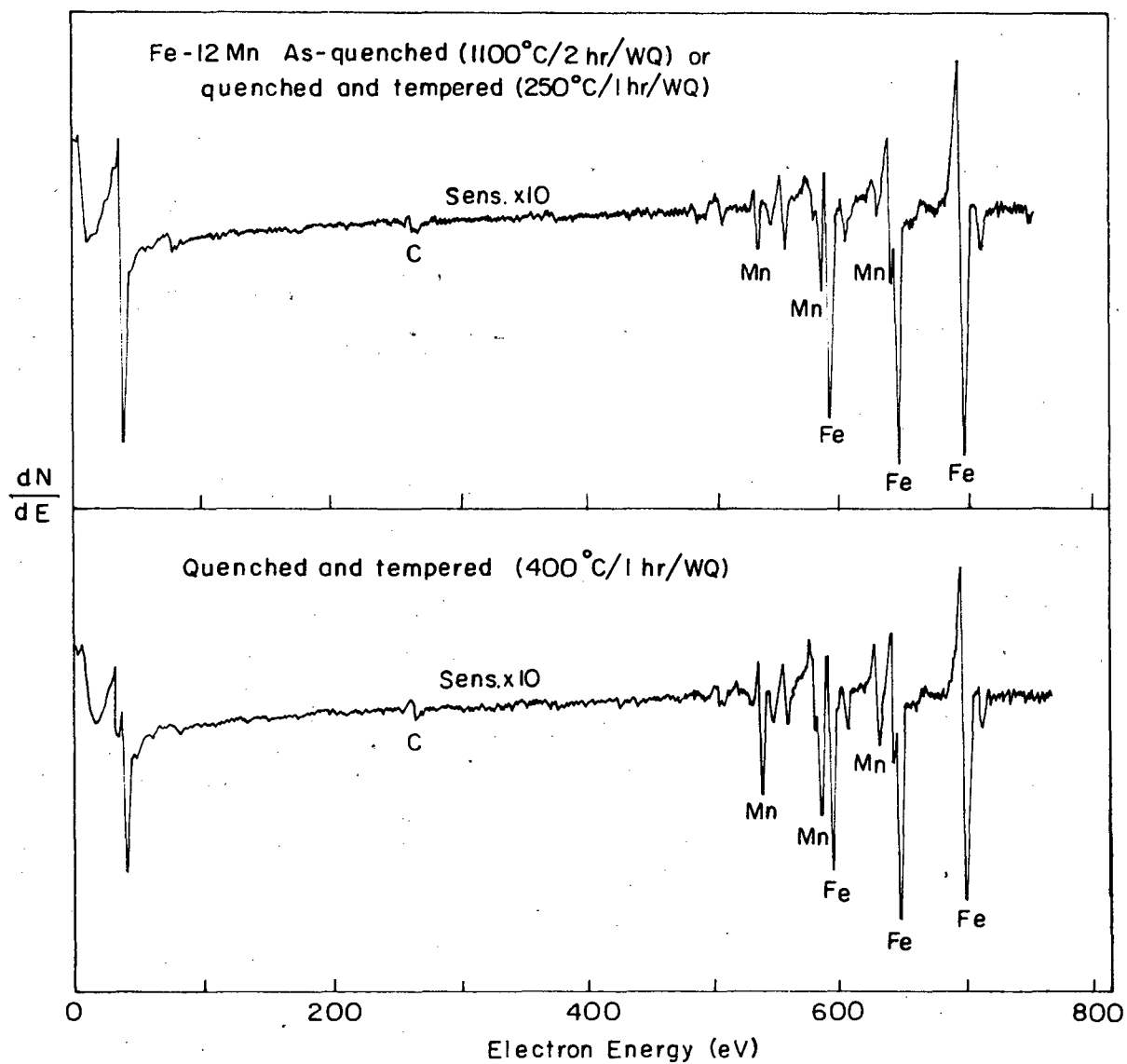


Figure 34

XBL 812-5223

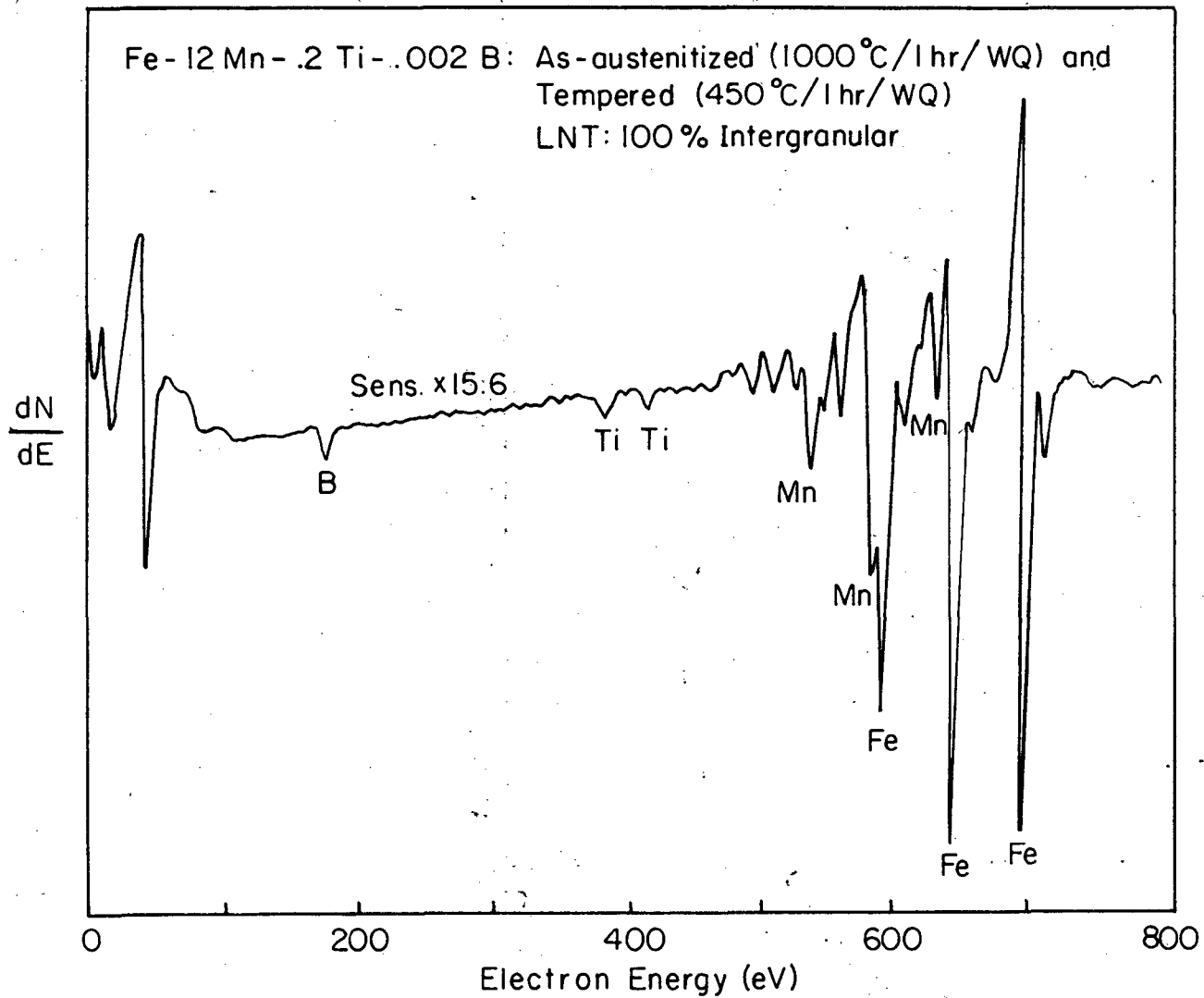


Figure 35

XBL812-5237

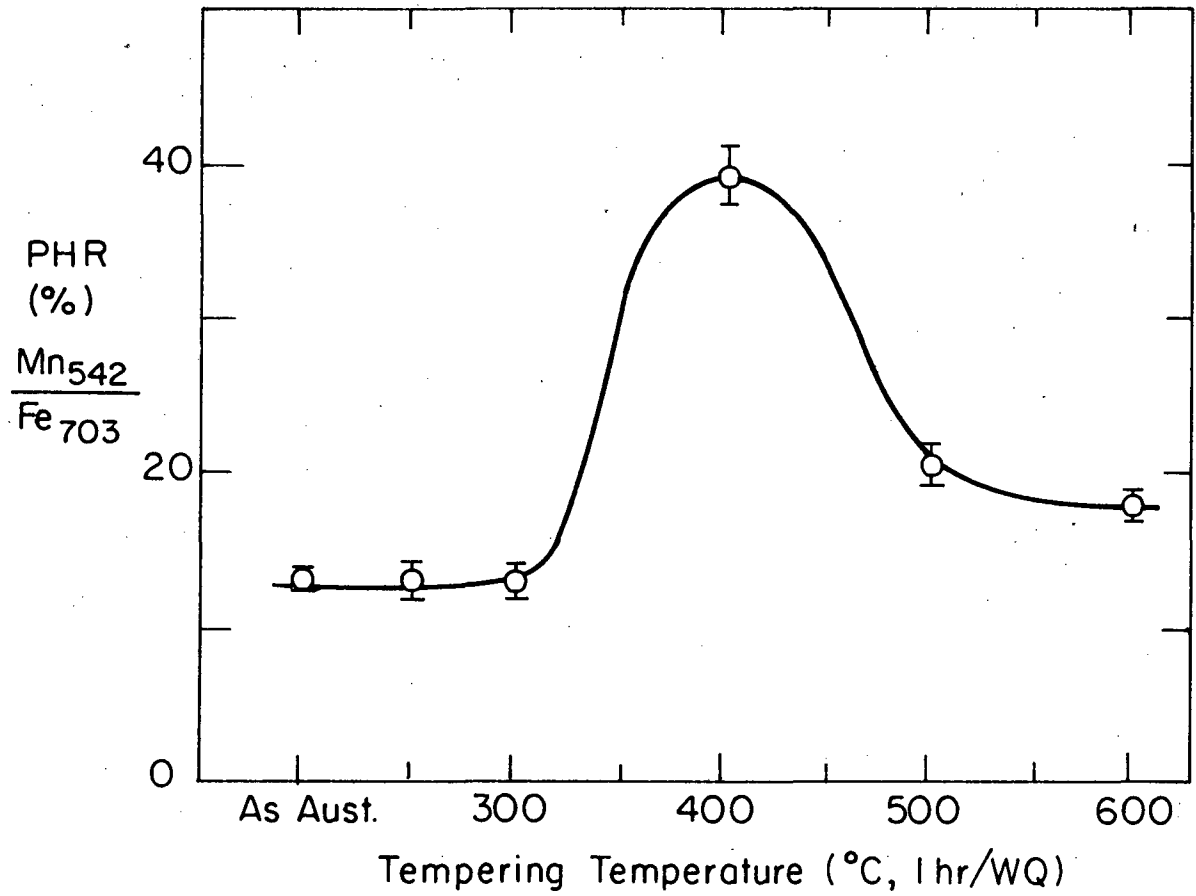


Figure 36

XBL 812-5228

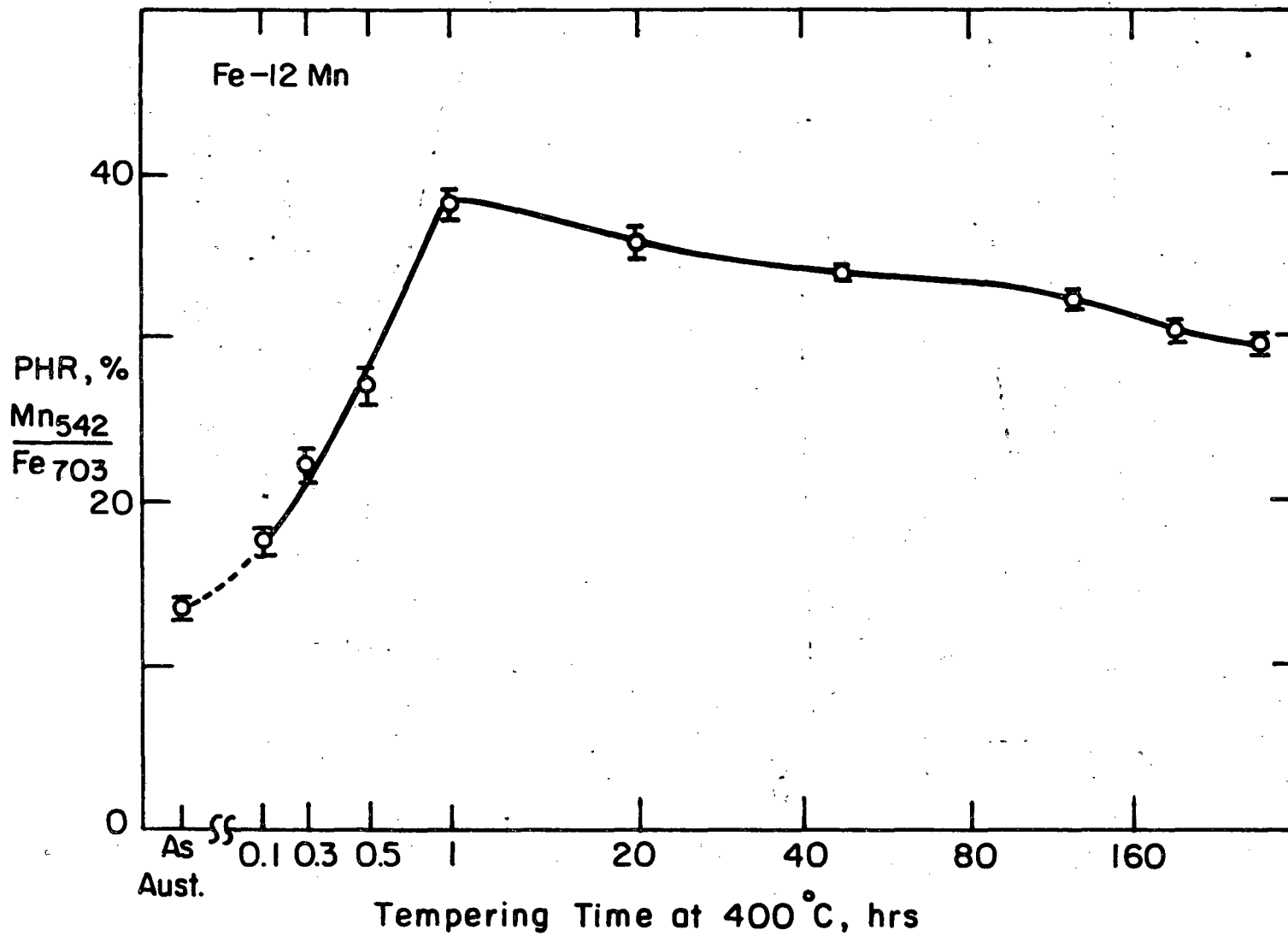


Figure 37

XBL8110-6794

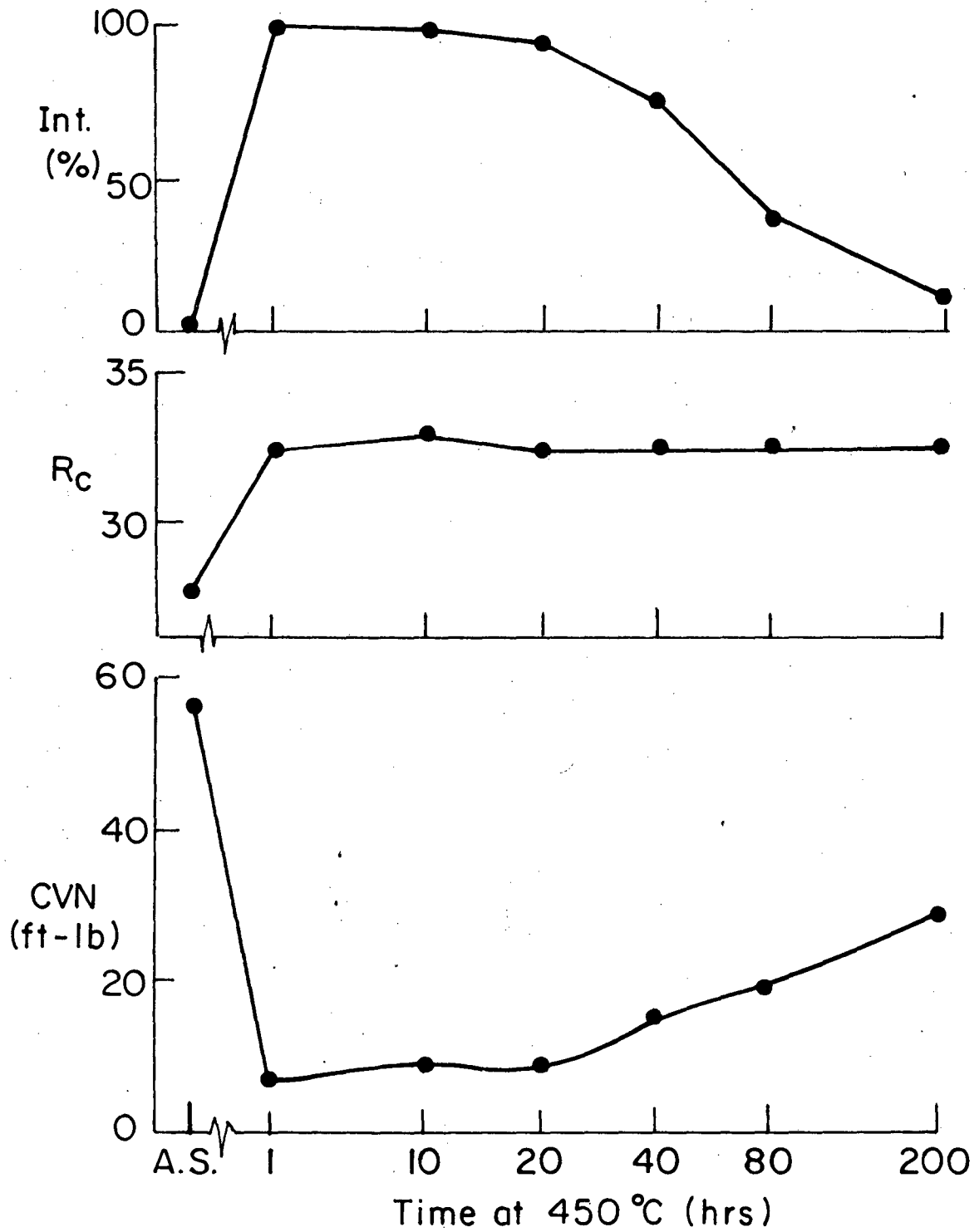


Figure 38

XBL 812-5225

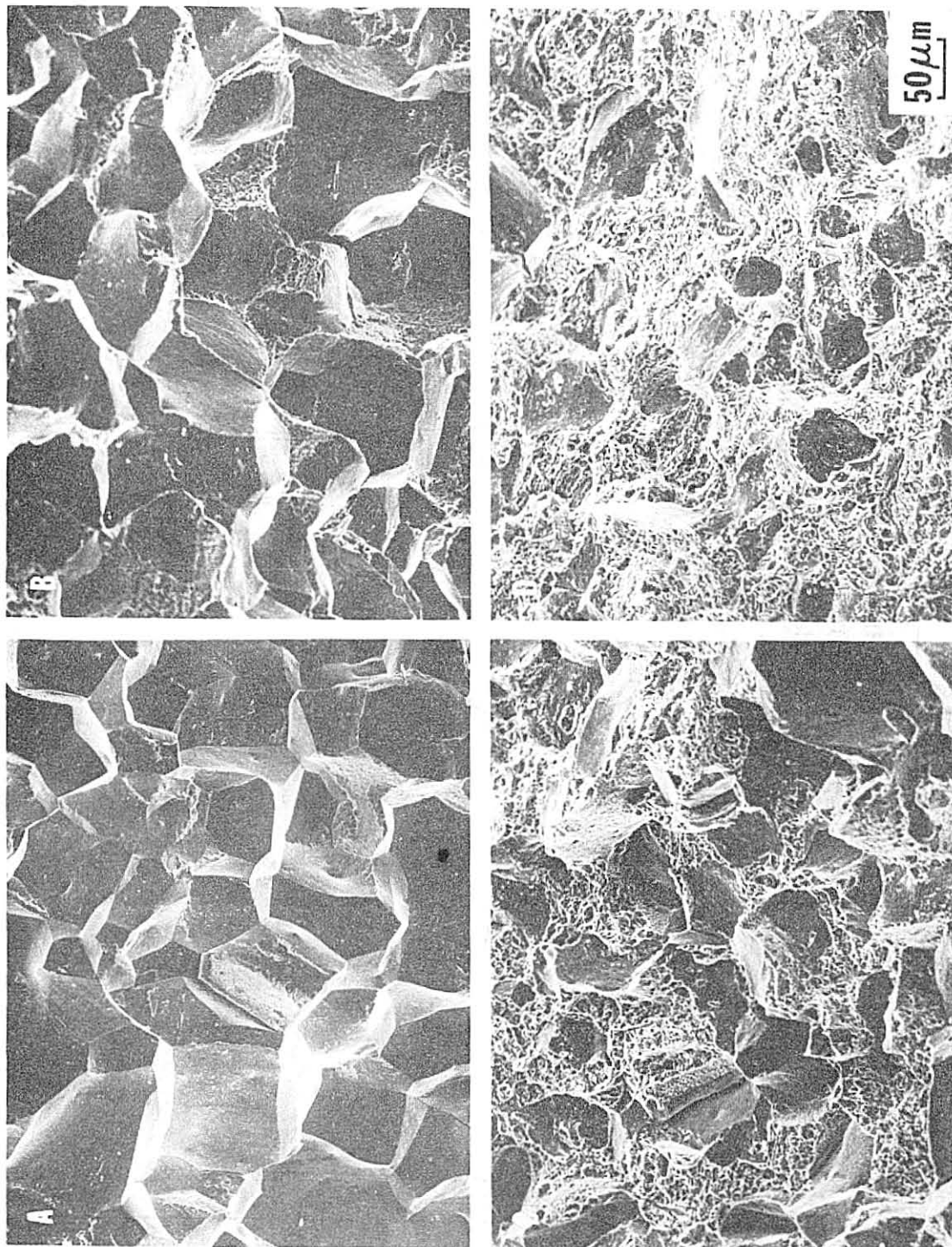


Figure 39

XBB 810-11049

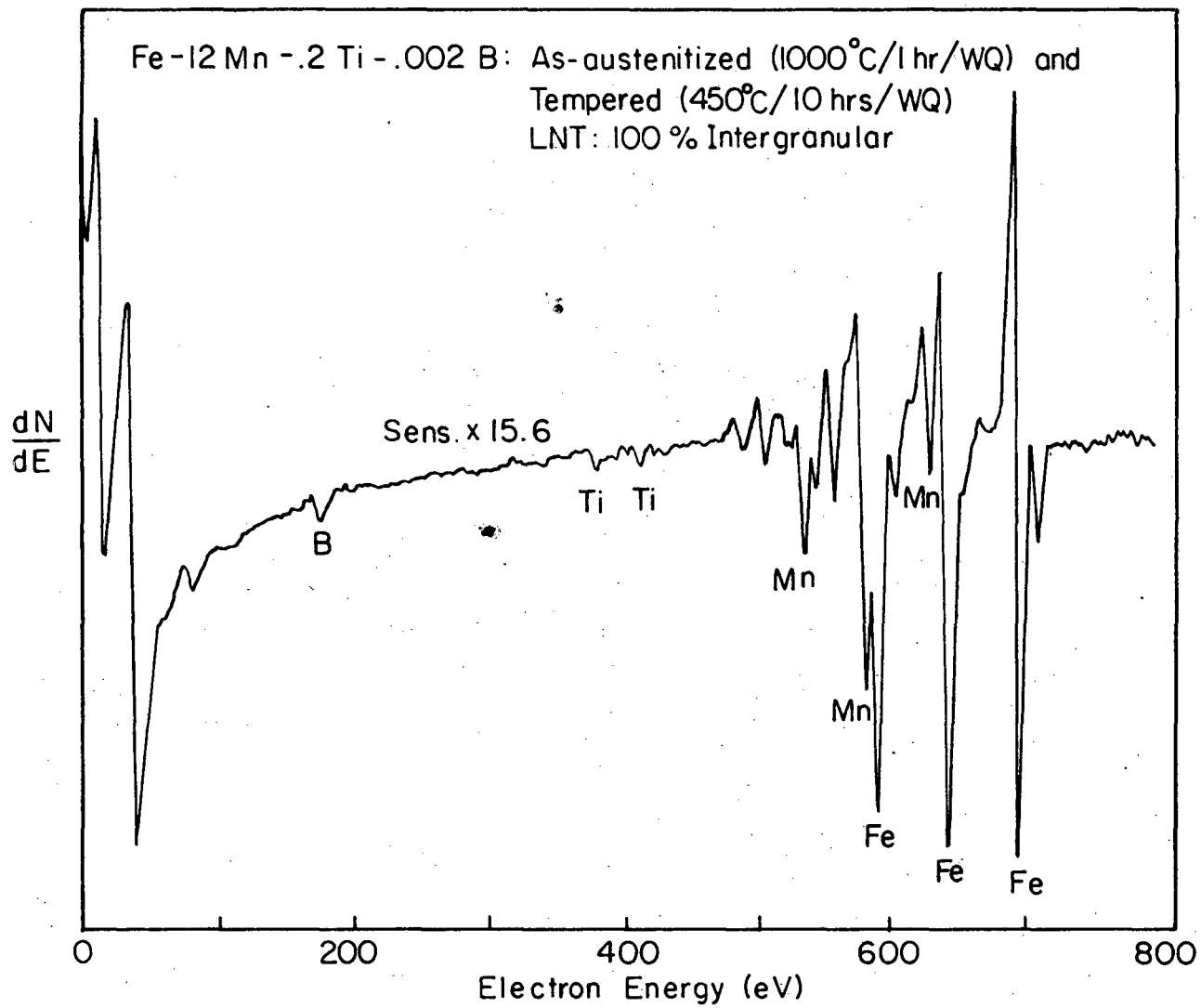


Figure 40

XBL 812-5238

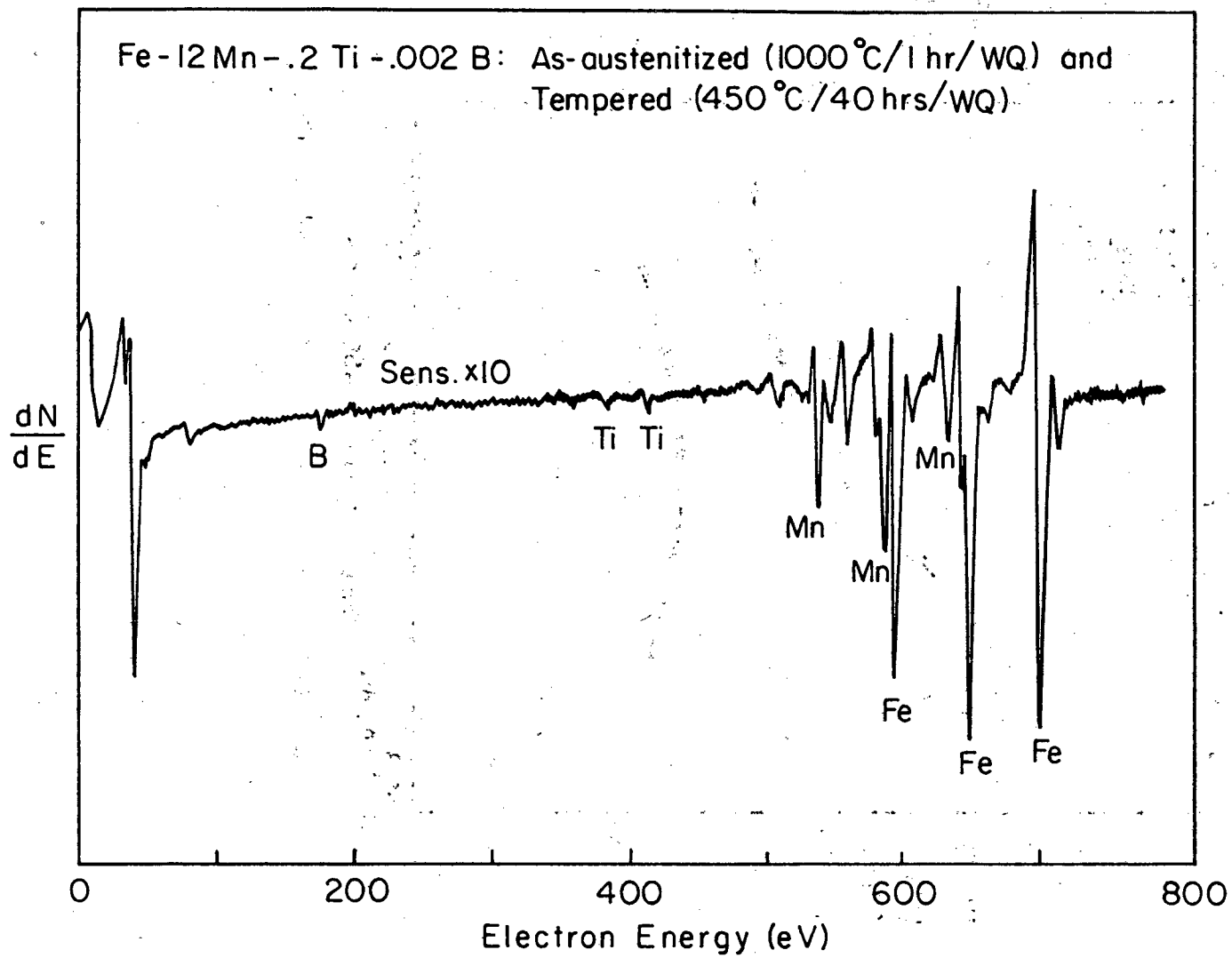


Figure 41

XBL812-5240

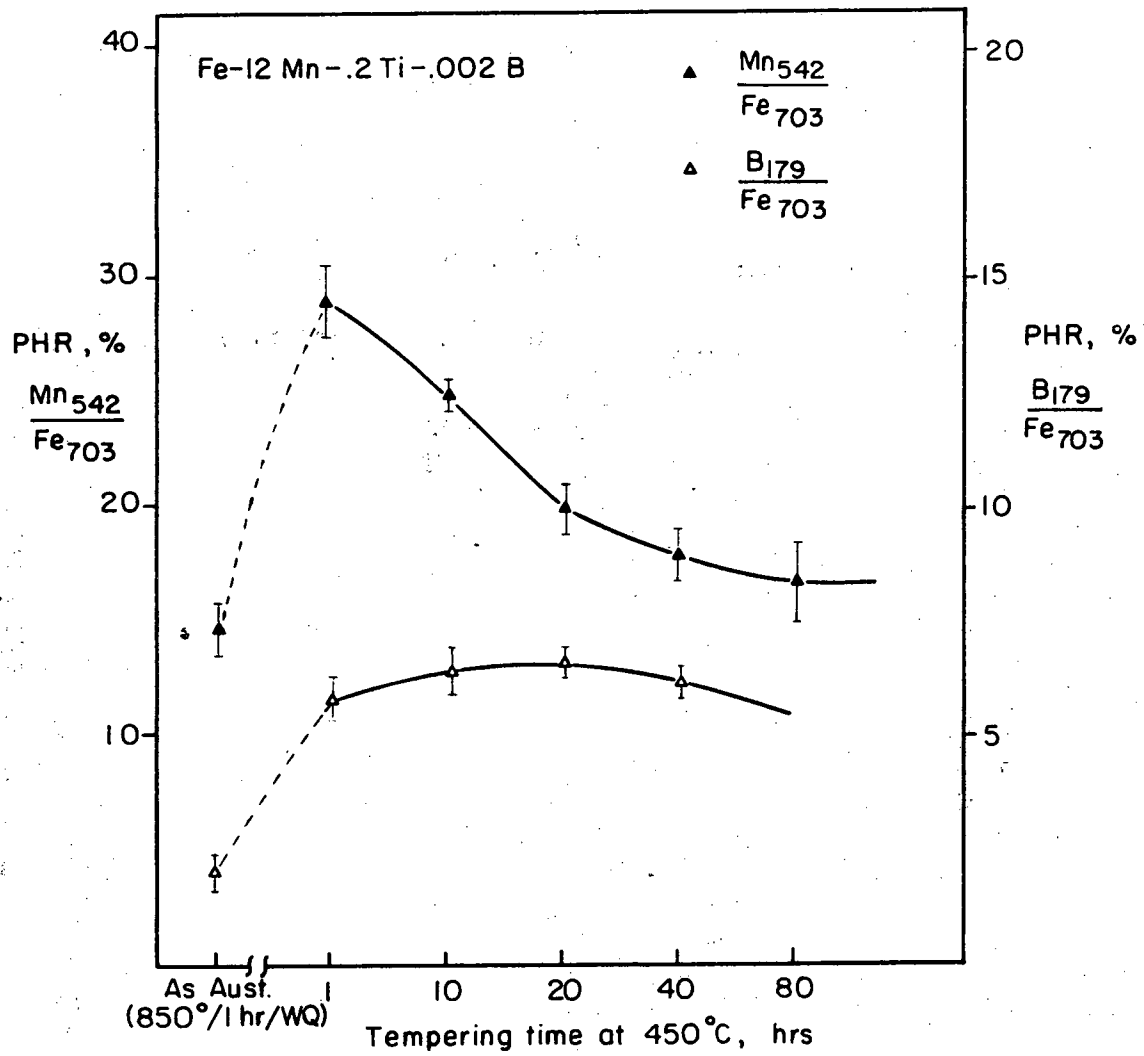


Figure 42

XBL 814-9449

Sputtering Profile

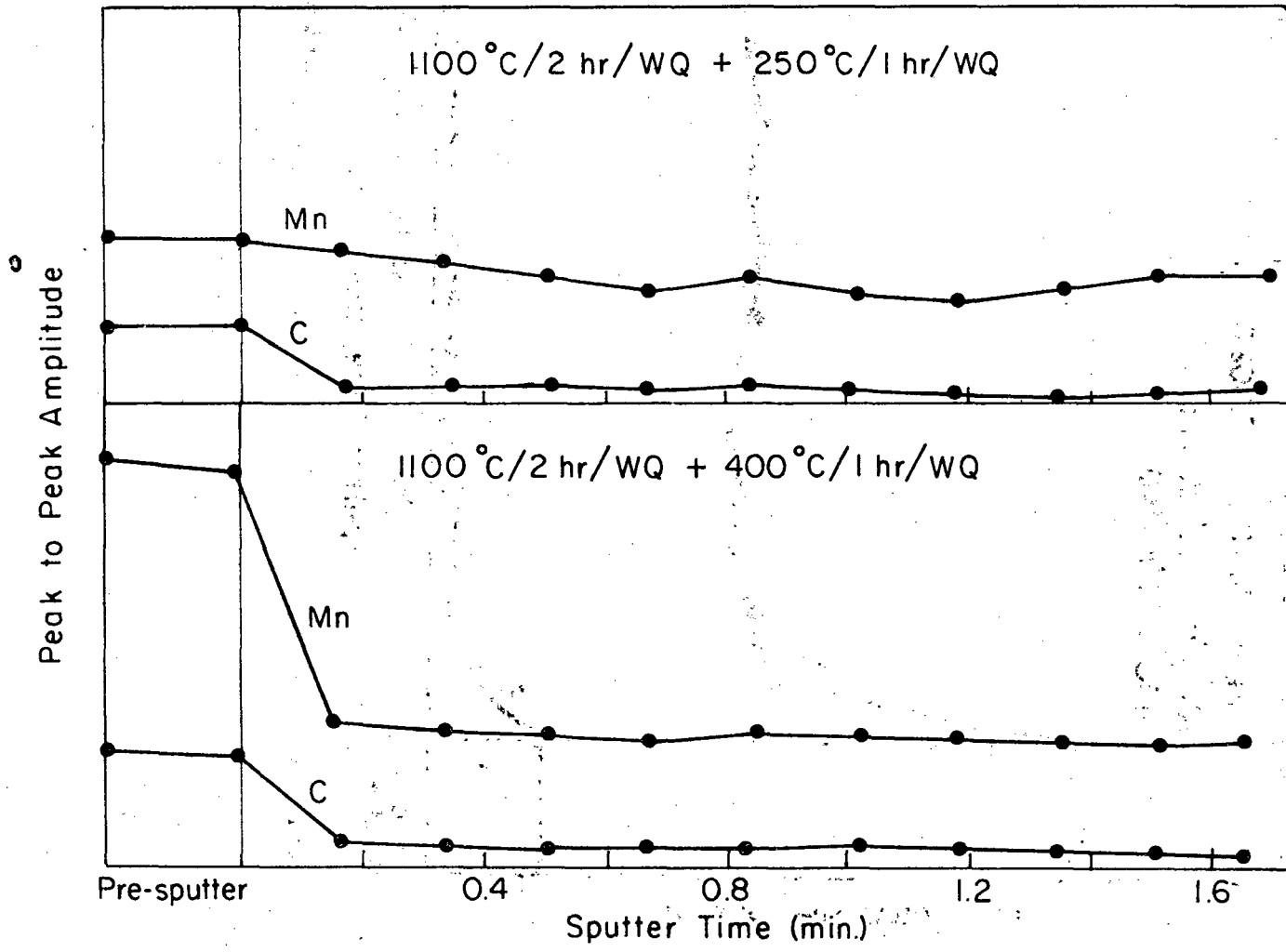


Figure 43

XBL 812-5230

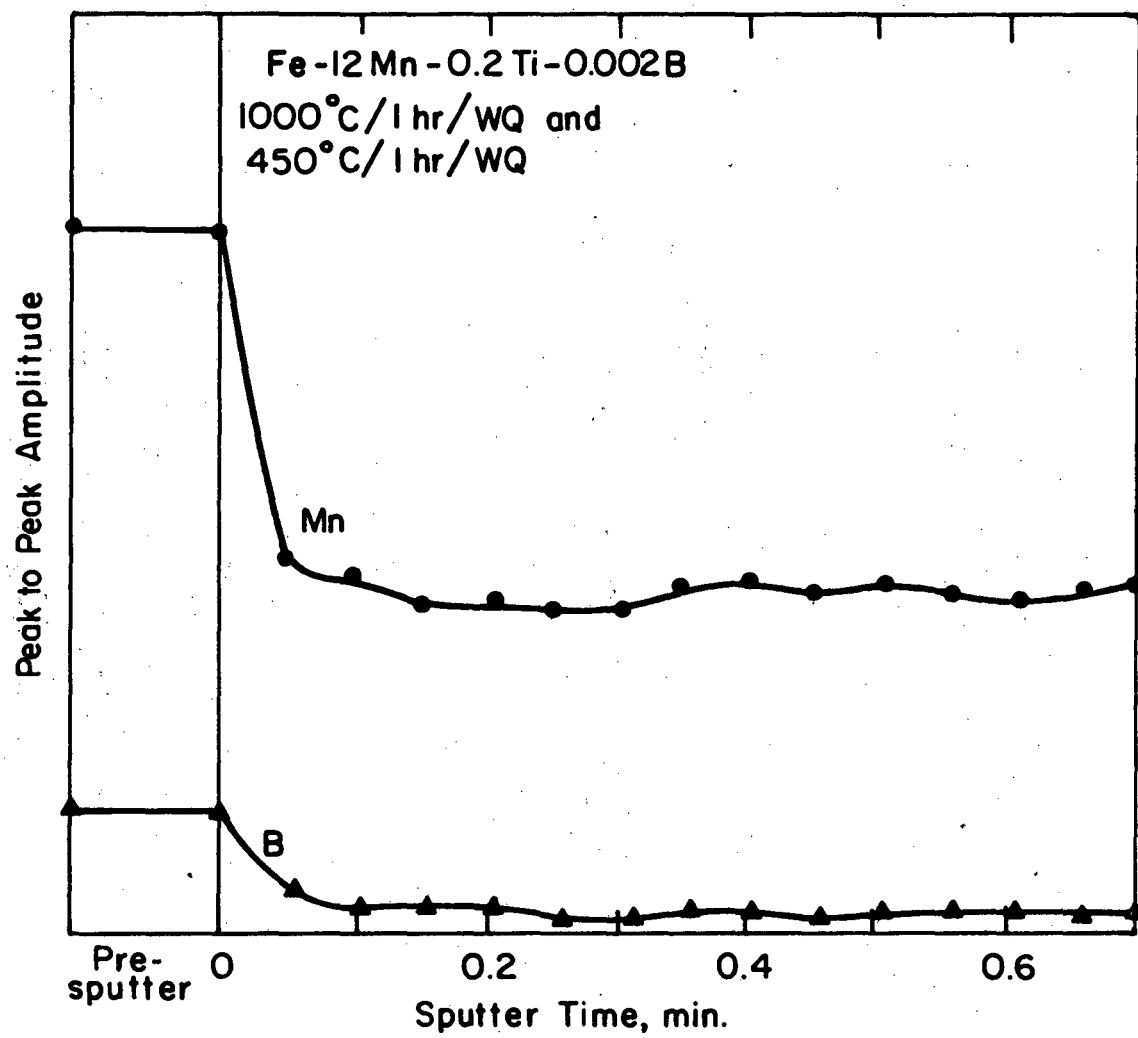


Figure 44

XBL 8110-6799

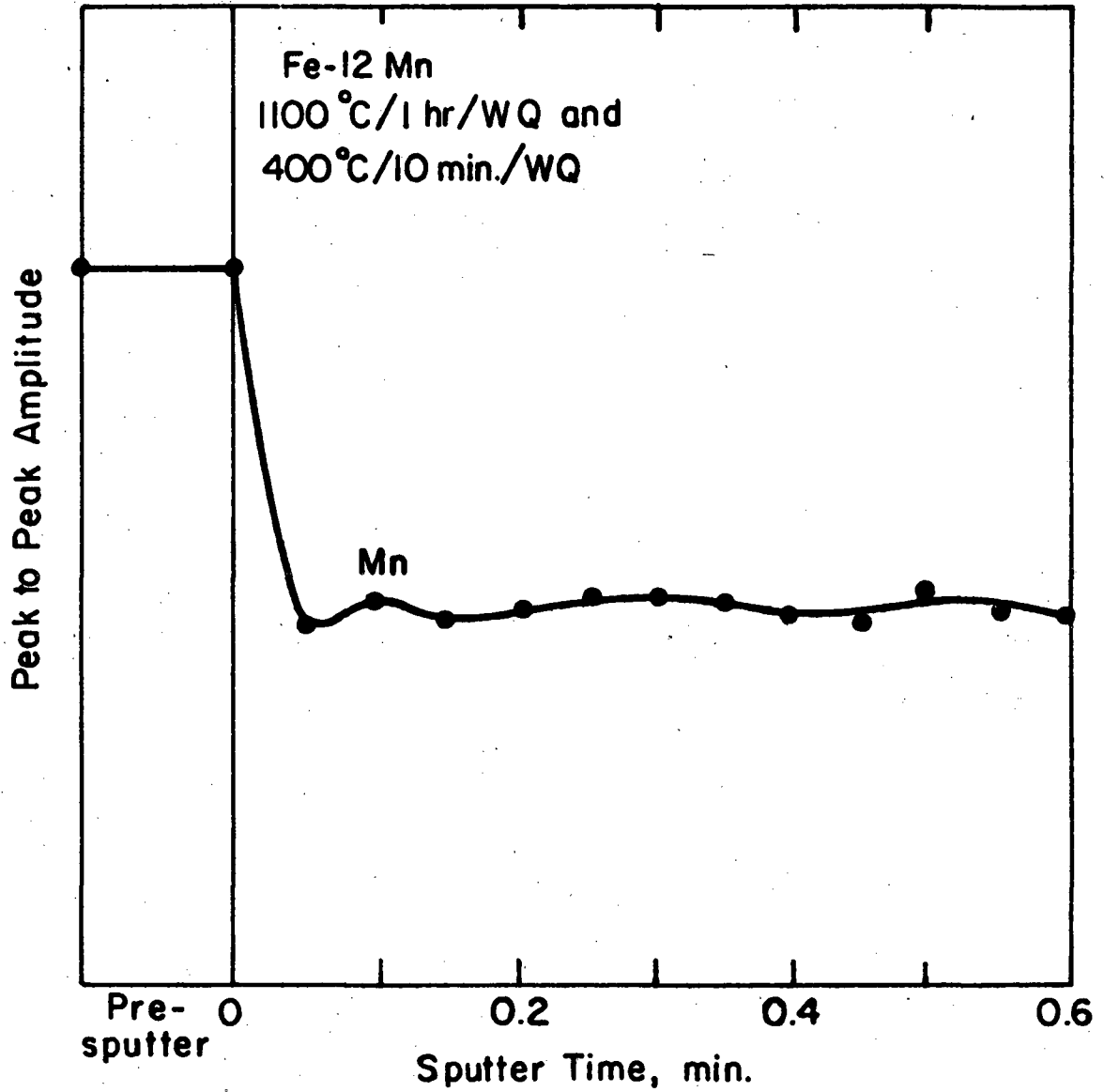


Figure 45

XBL8110-6795

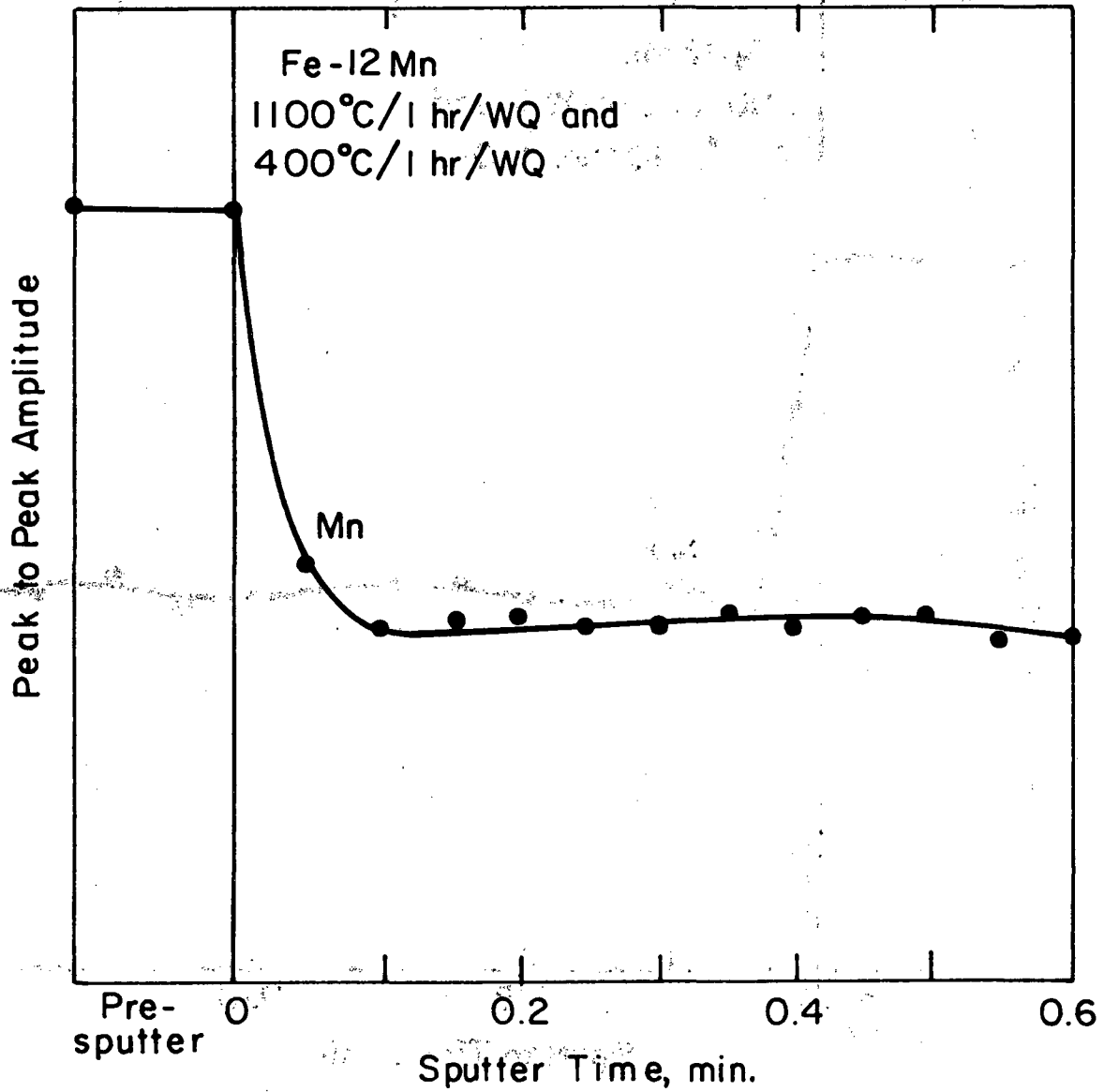


Figure 46

XBL8110-6796

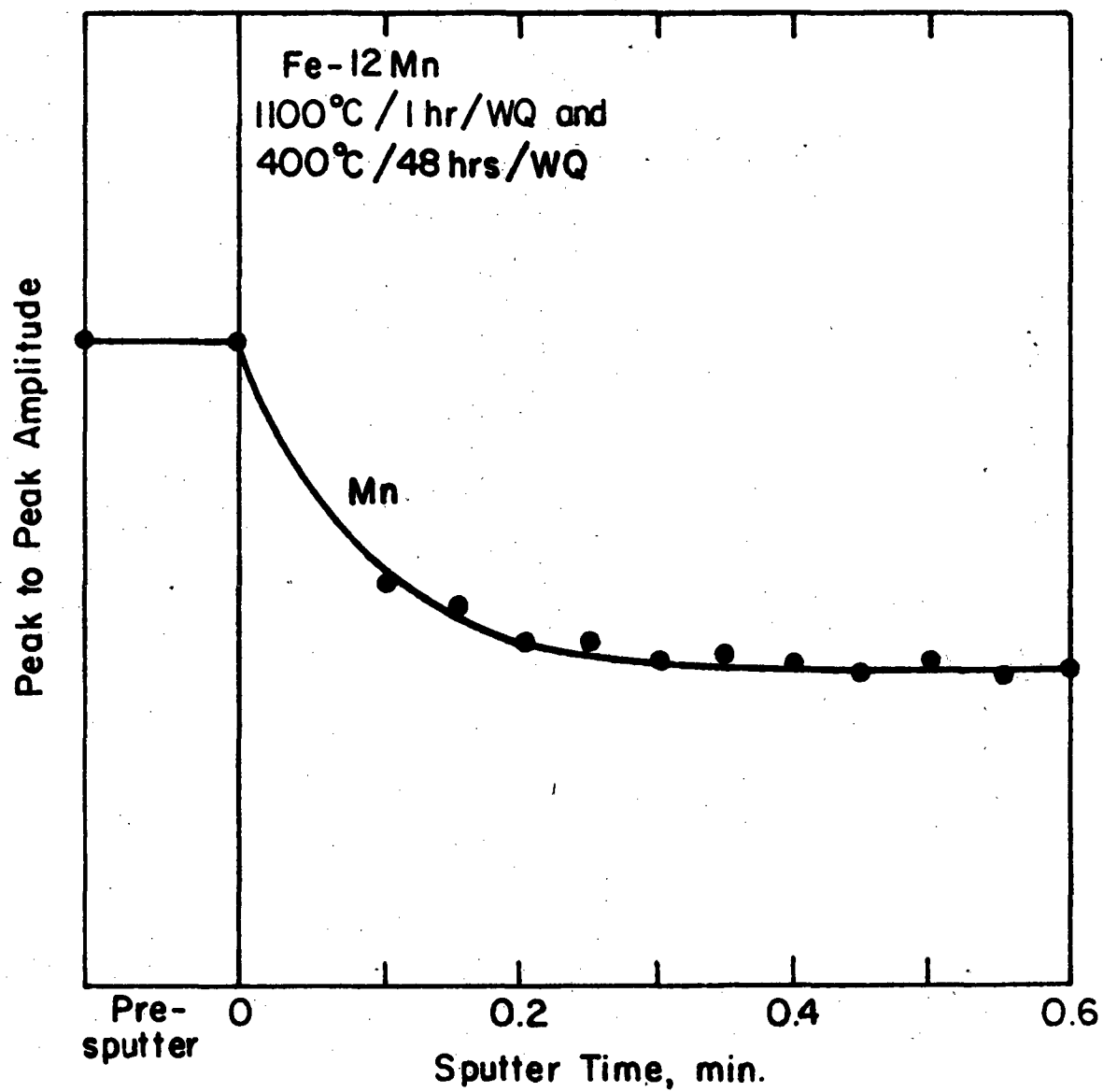


Figure 47

XBL8110-6797

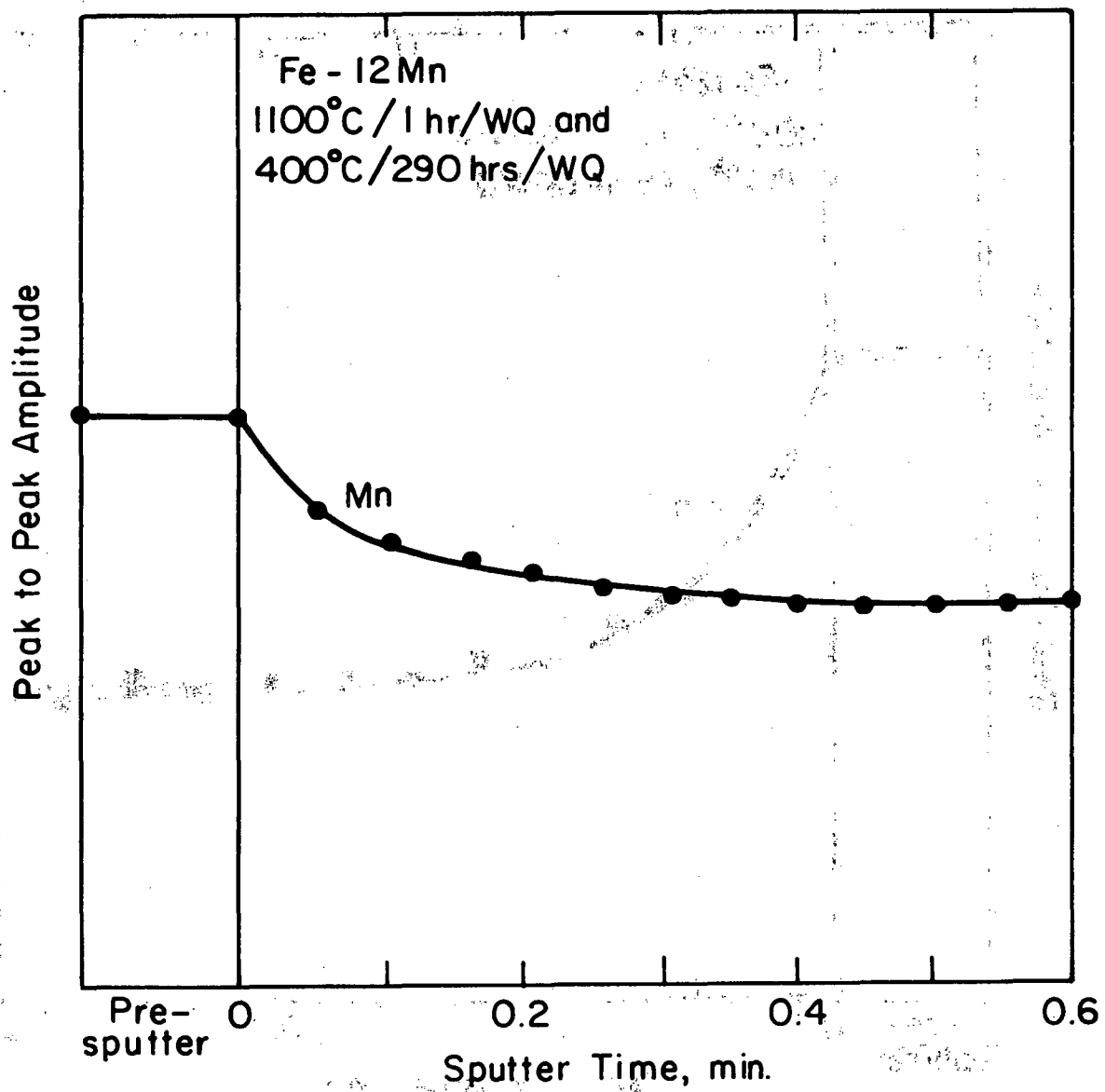


Figure 48

XBL 8110-6798

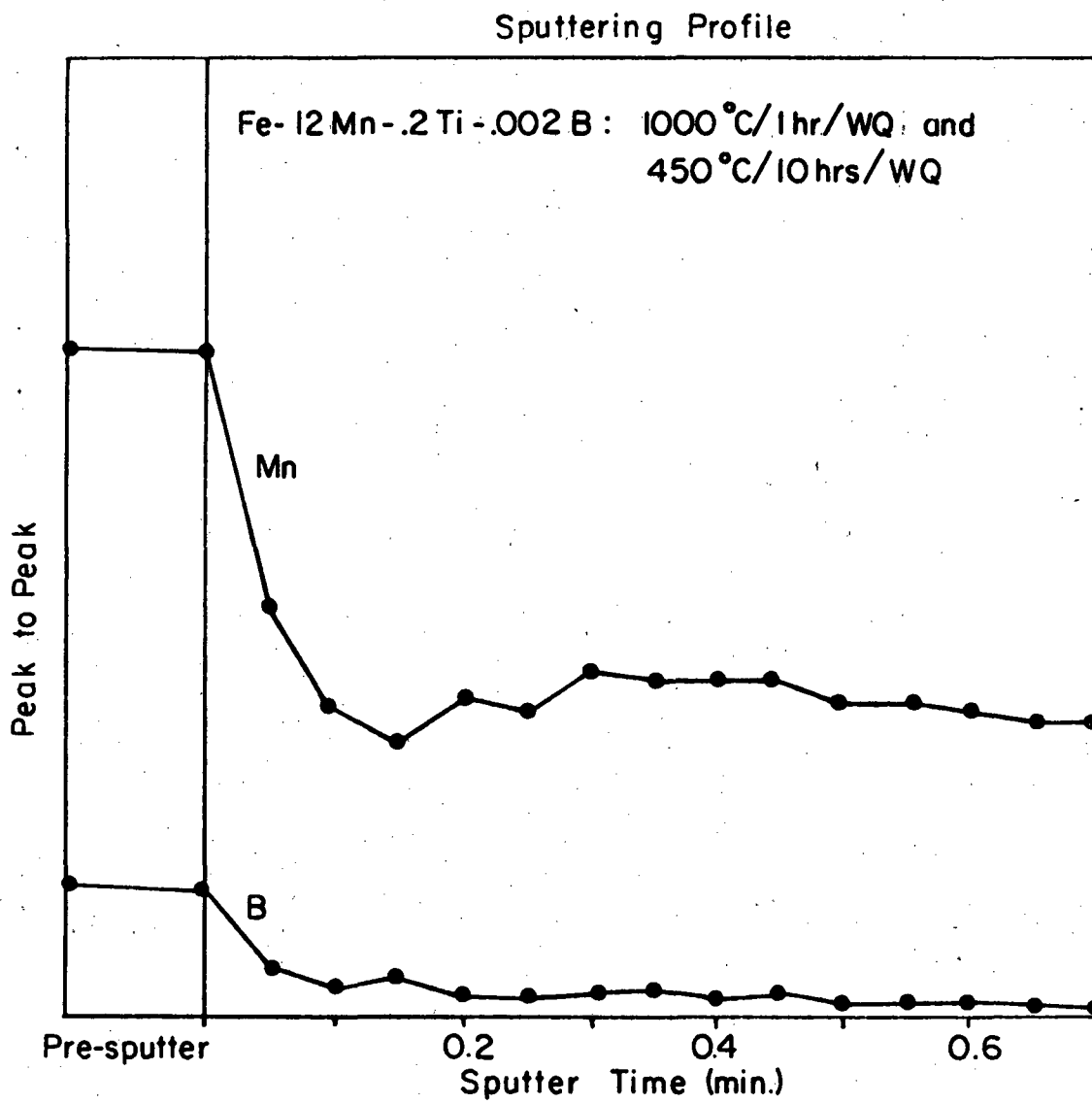


Figure 49

XBL 812-5232

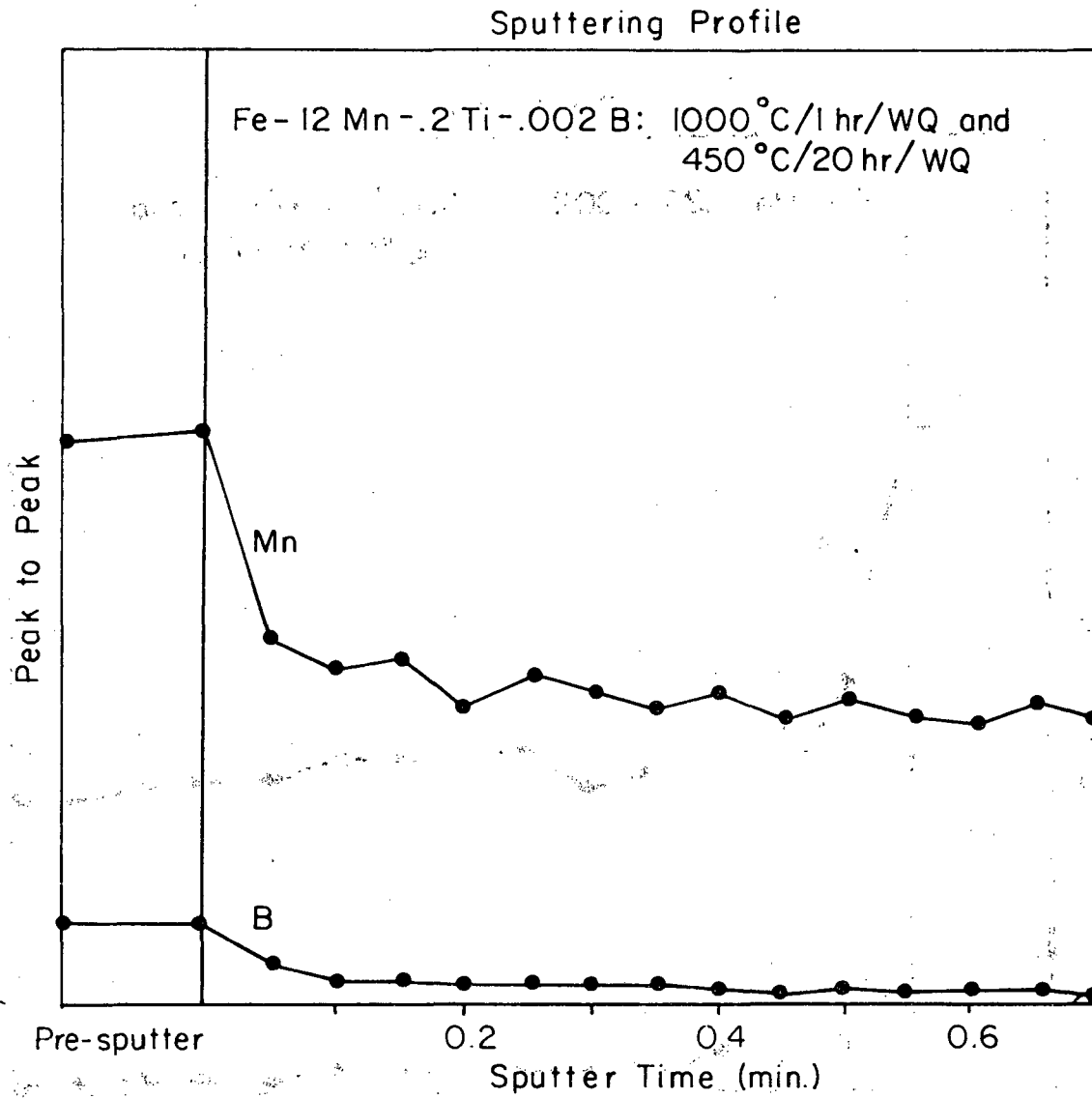


Figure 50

XBL 812-5233

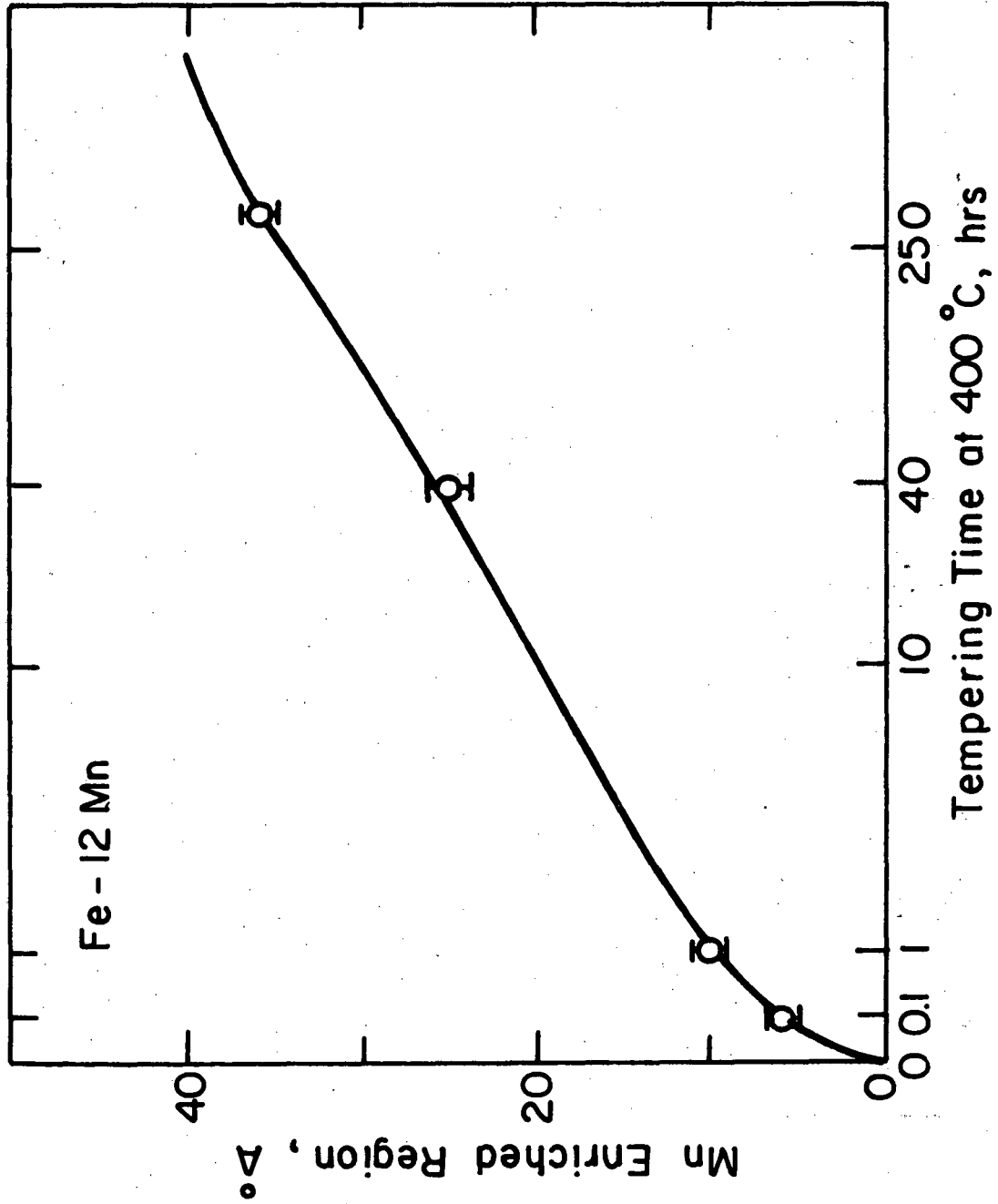


Figure 51

XBL 8110-6789

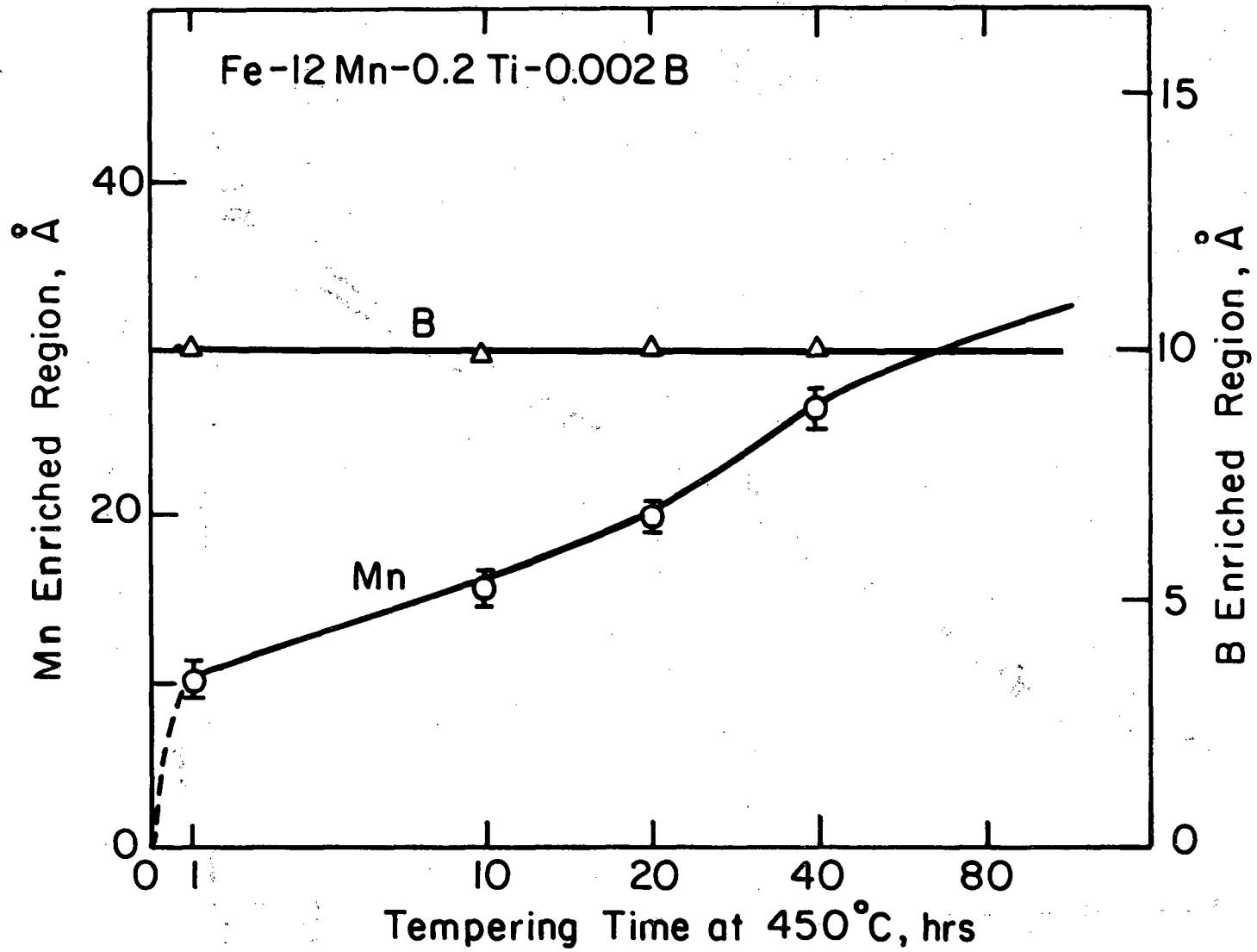
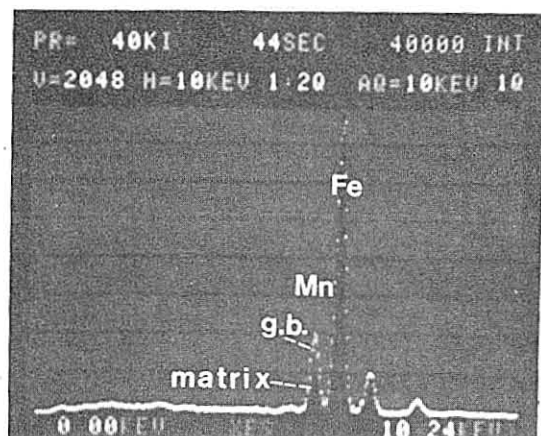
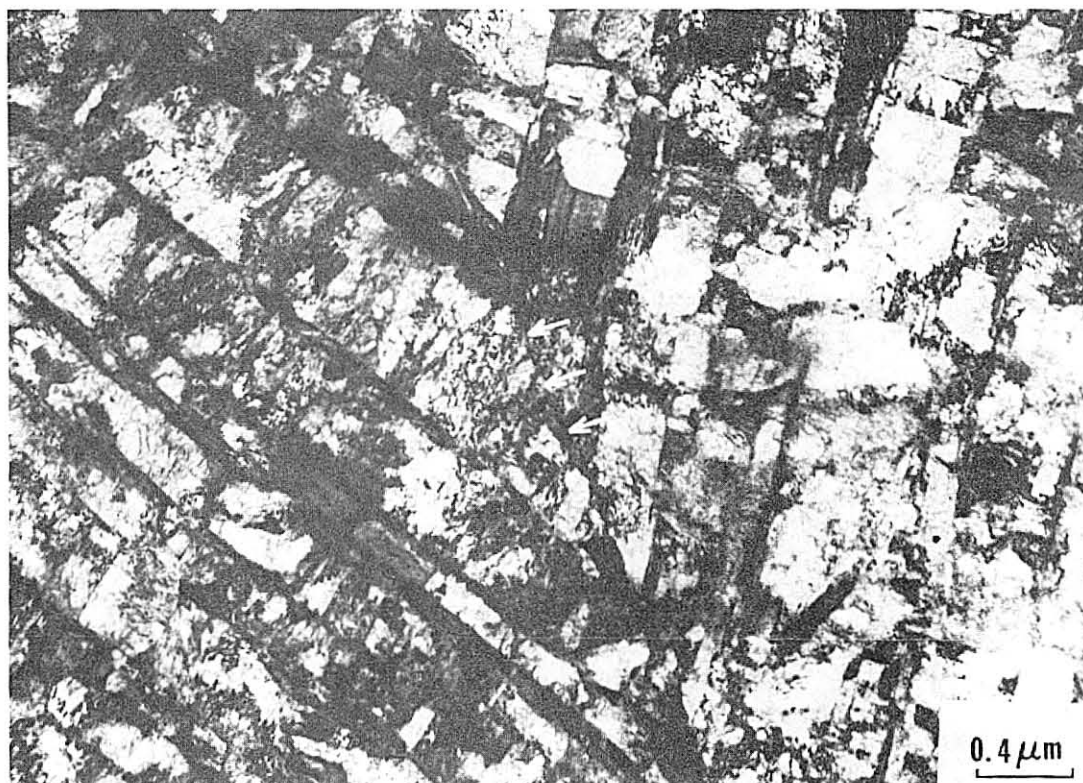


Figure 52

XBL 8110-6790



**Tempering at
 400° C, 1 hr**

Figure 53

CBB 810-11953

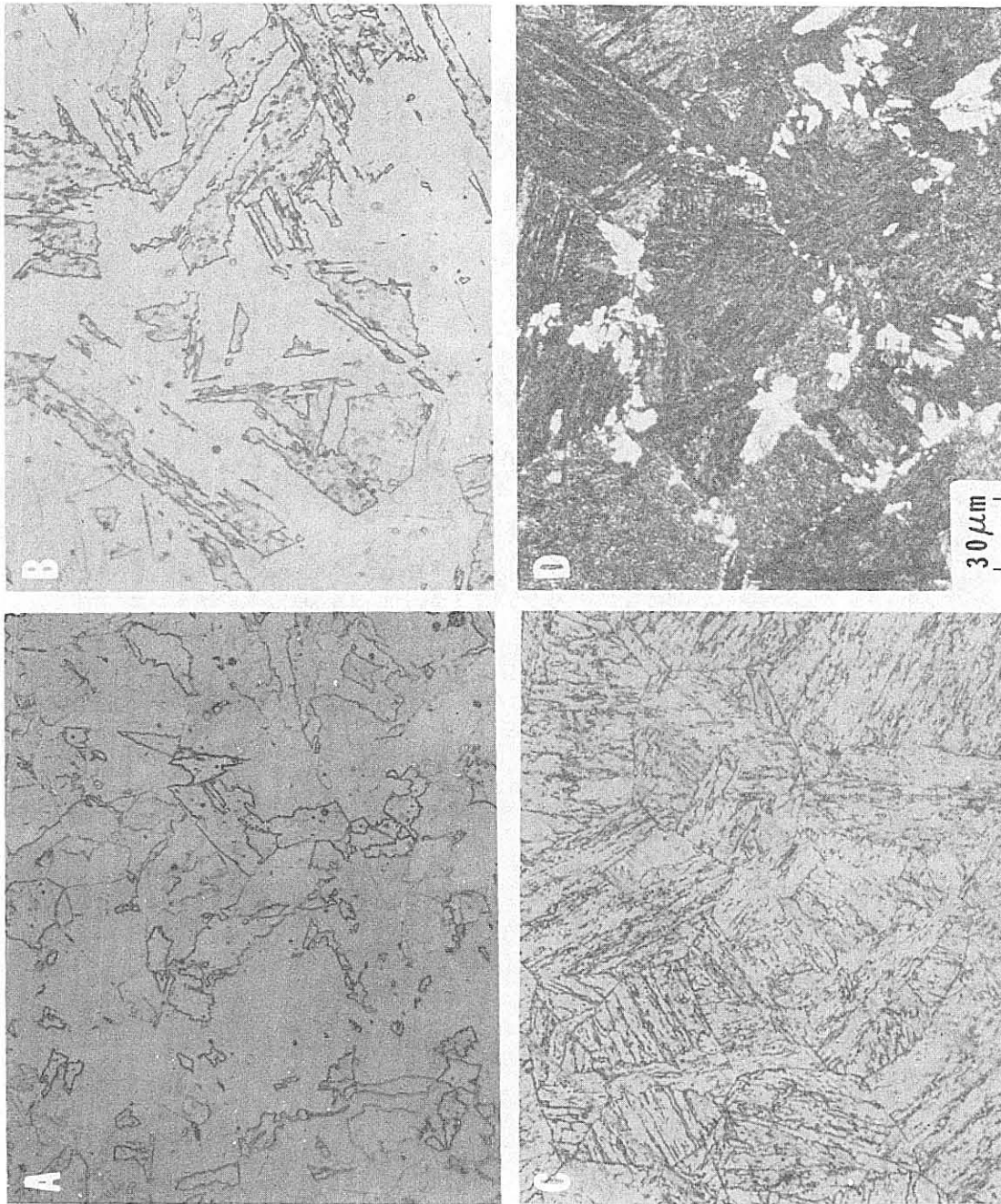


Figure 54

XBB 810-11051

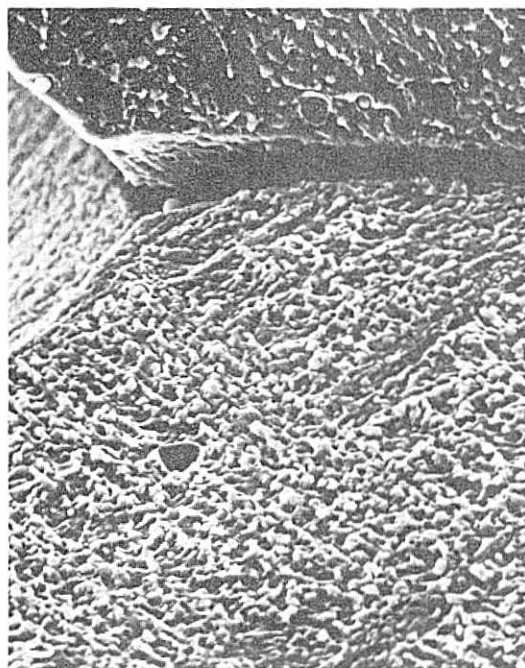
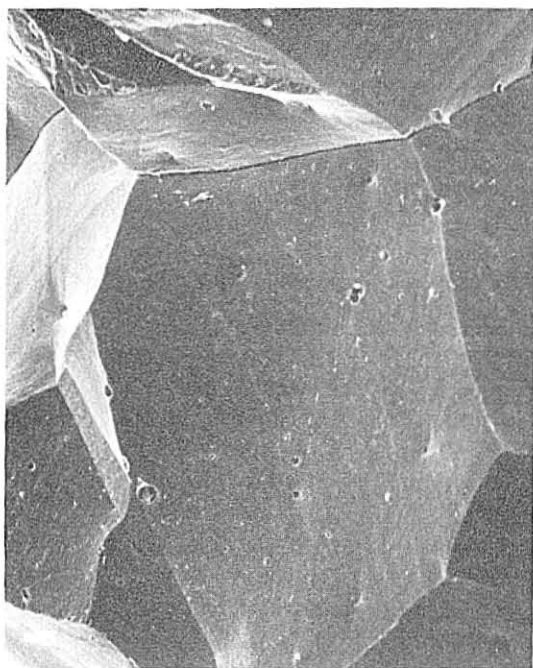
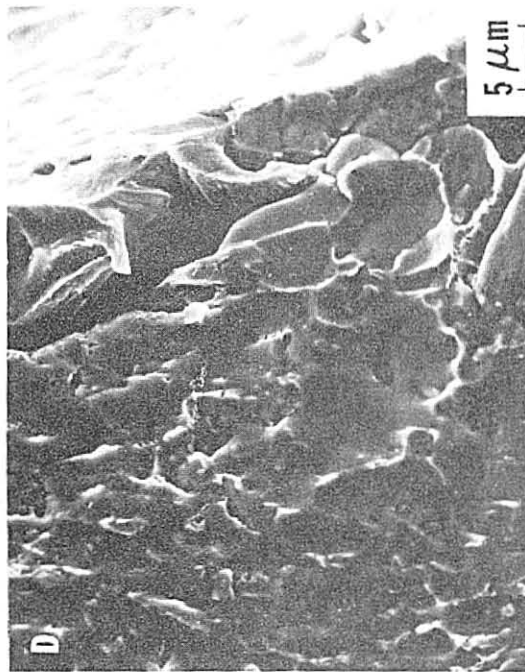
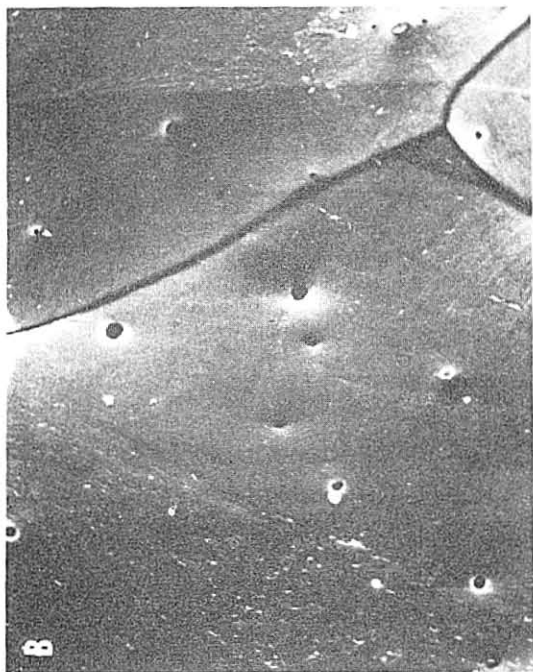


Figure 55

XBB 810-10731

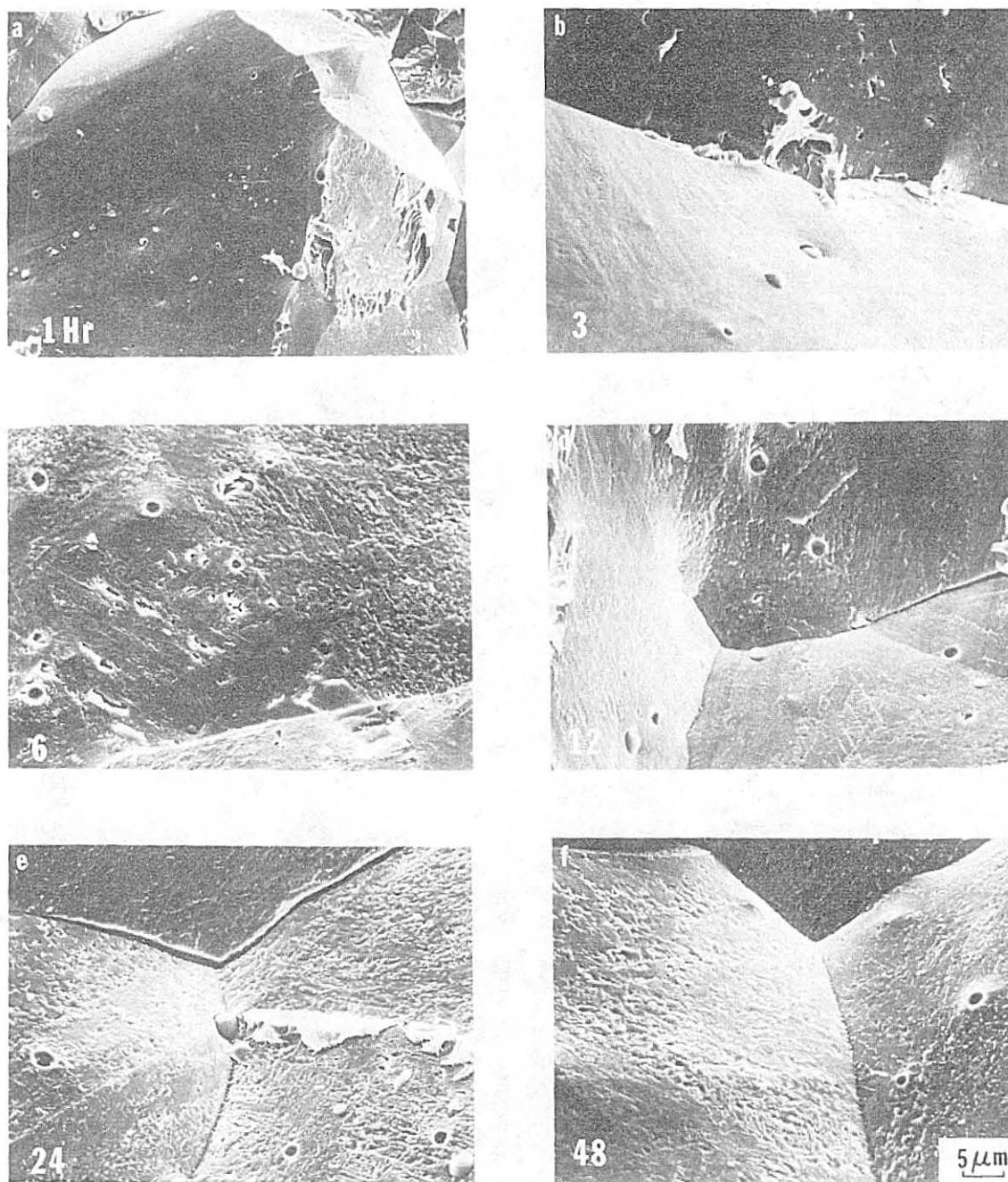


Figure 56

XBB 811-1093

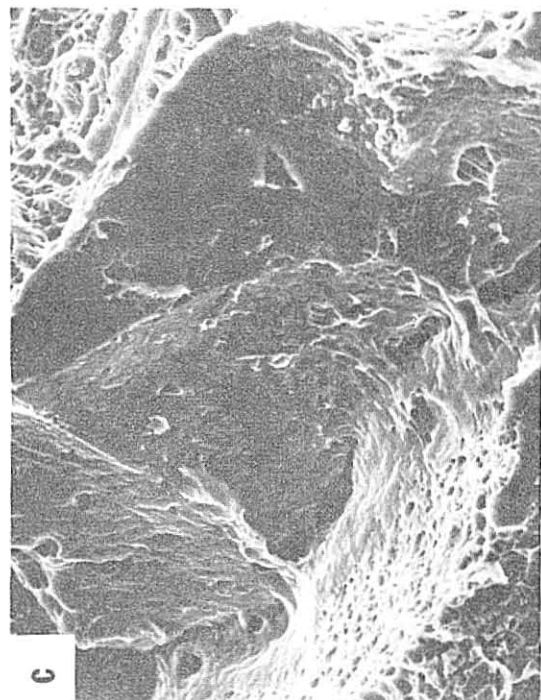
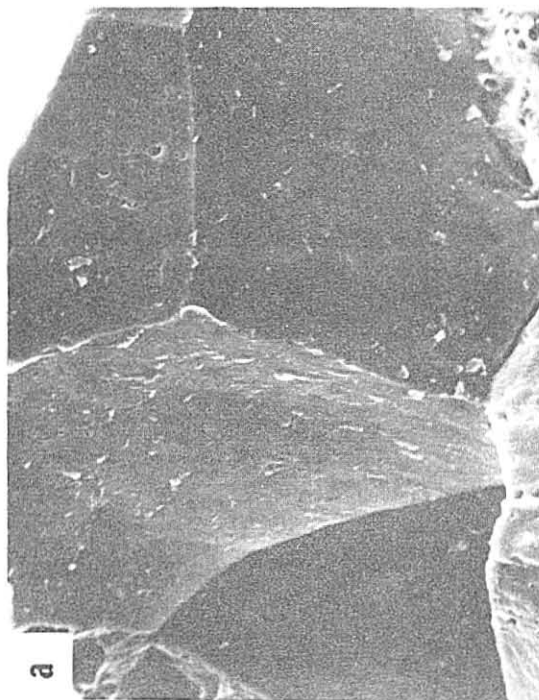
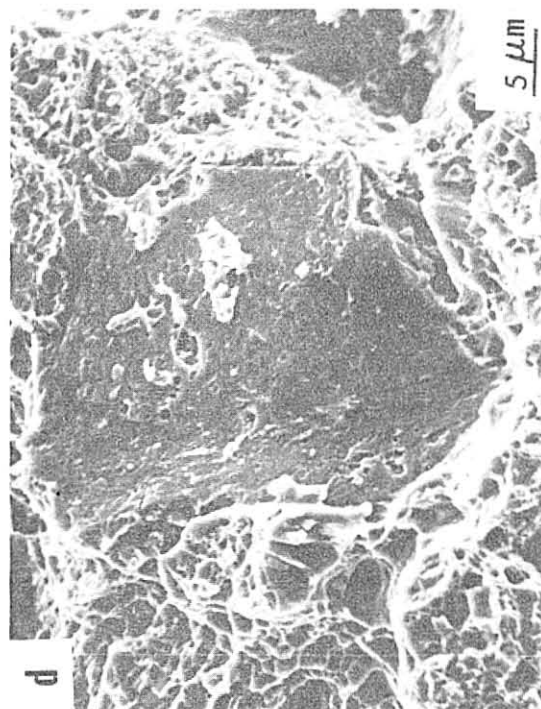
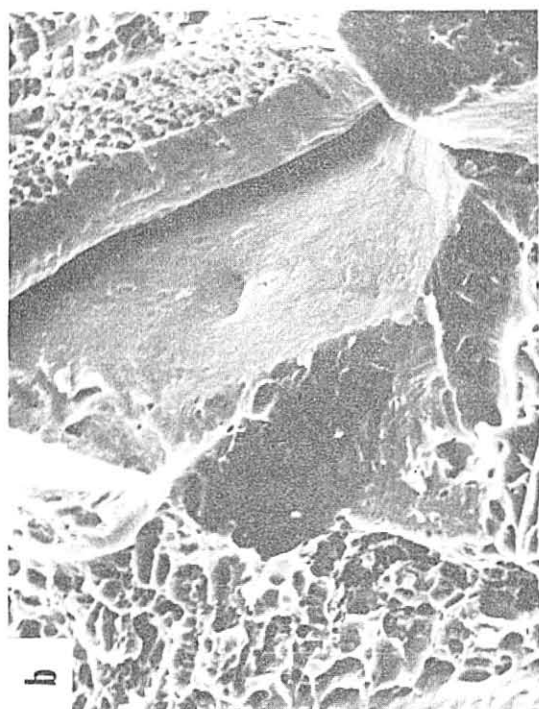


Figure 58

XBB 810-10732

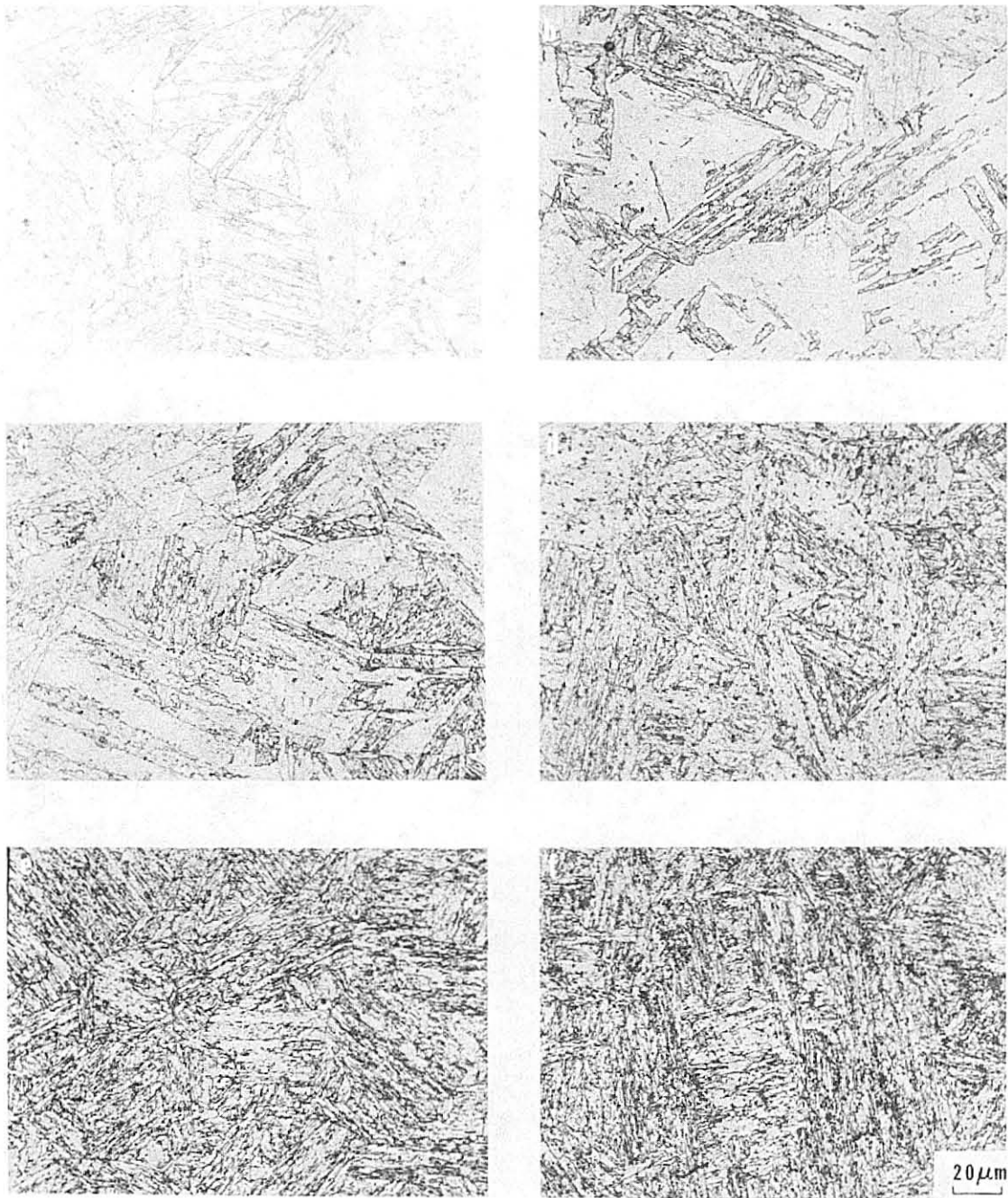


Figure 57

XBB 811-1091

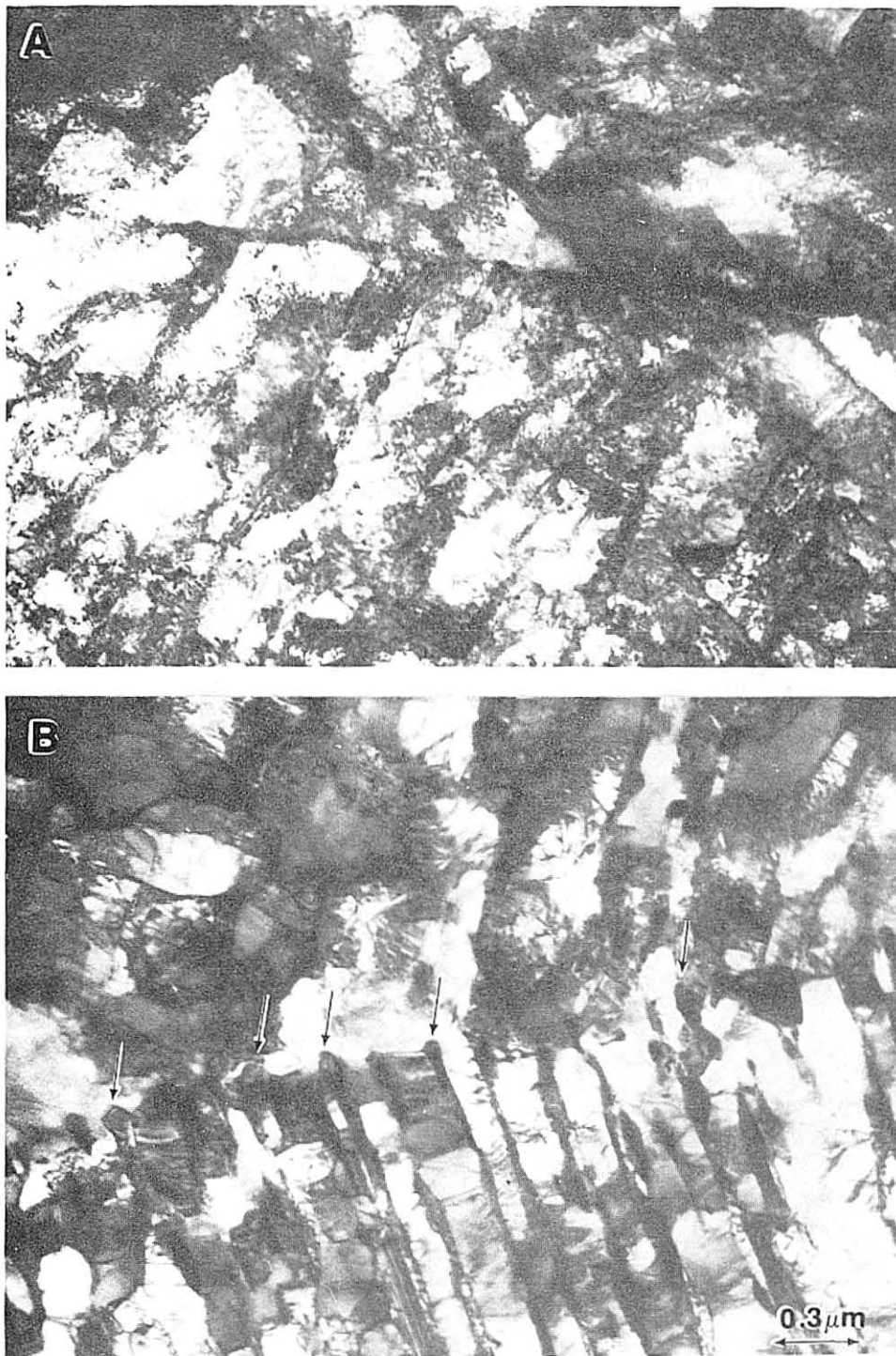


Figure 59

XBB 821-872

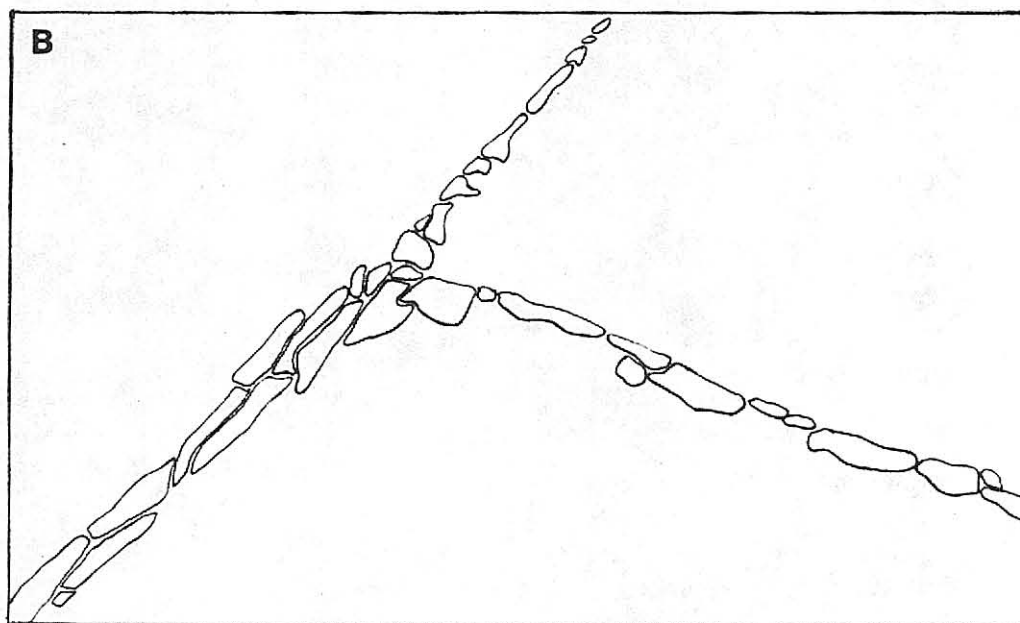
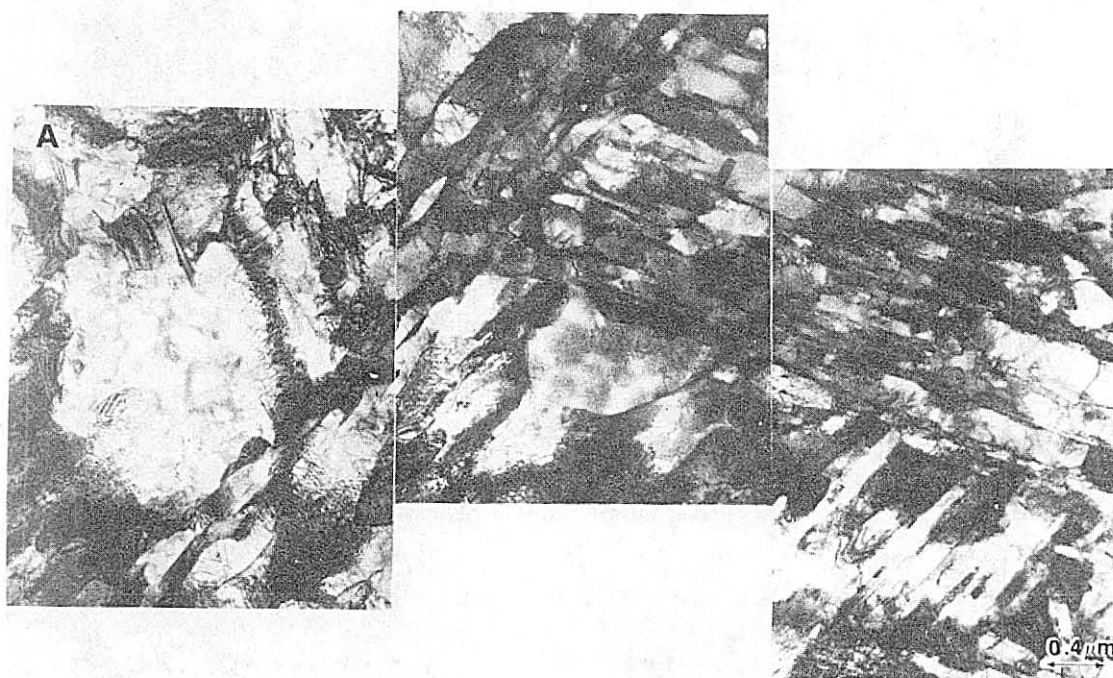


Figure 60

XBB 821-873

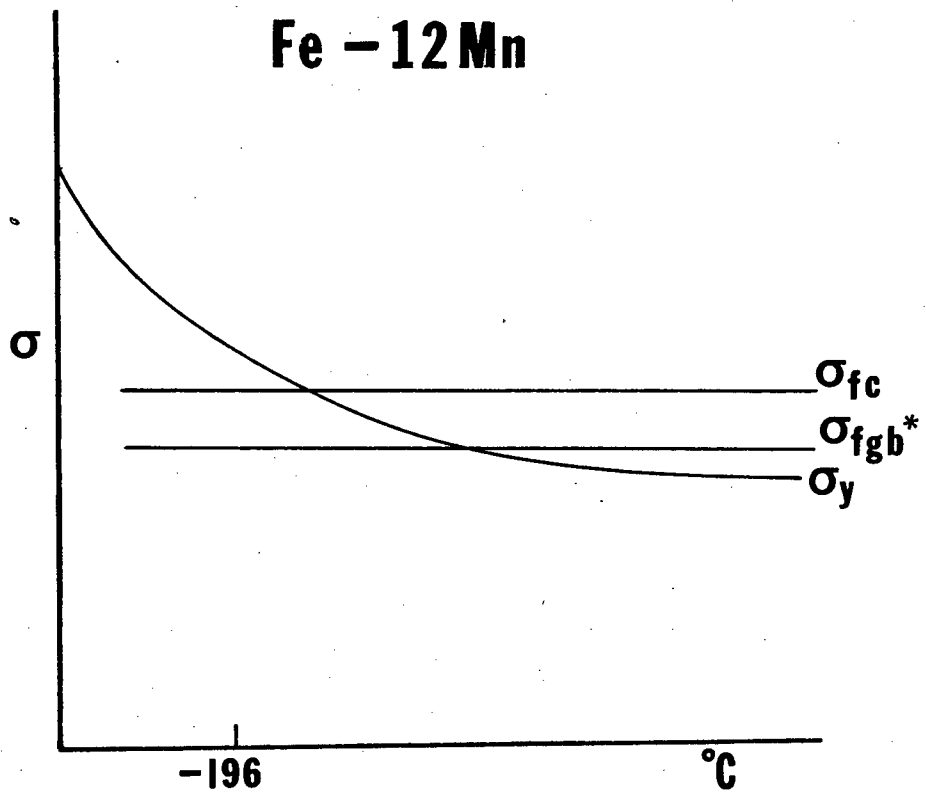


Figure 61

XBL 8112-12974

This report was done with support from the Department of Energy. Any conclusions or opinions expressed in this report represent solely those of the author(s) and not necessarily those of The Regents of the University of California, the Lawrence Berkeley Laboratory or the Department of Energy.

Reference to a company or product name does not imply approval or recommendation of the product by the University of California or the U.S. Department of Energy to the exclusion of others that may be suitable.

TECHNICAL INFORMATION DEPARTMENT
LAWRENCE BERKELEY LABORATORY
UNIVERSITY OF CALIFORNIA
BERKELEY, CALIFORNIA 94720